Studies of Nonlinear Femtosecond Pulse Propagation in Bulk Materials

by

Hilary K. Eaton

B.S. Furman University 1993

A thesis submitted to the

Faculty of the Graduate School of the

University of Colorado in partial fulfillment

of the requirements for the degree of

Doctor of Philosophy

Department of Chemistry and Biochemistry

1999

This thesis entitled:
Studies of Nonlinear Femtosecond Pulse Propagation in Bulk Materials
written by Hilary K. Eaton
has been approved for the Department of Chemistry and Biochemistry

Stephen R. Leone

Tracy S. Clement

Date

The final copy of this thesis has been examined by the signatories, and we find that both the content and the form meet acceptable presentation standards of scholarly work in the above mentioned discipline.

Eaton, Hilary K. (Ph. D.)

Studies of Nonlinear Femtosecond Pulse Propagation in Bulk Materials

Thesis directed by Professor Stephen R. Leone

Femtosecond pulse lasers are finding widespread application in a variety of fields including medical research, optical switching and communications, plasma formation, high harmonic generation, and wavepacket formation and control. As the number of applications for femtosecond pulses increases, so does the need to fully understand the linear and nonlinear processes involved in propagating these pulses through materials under various conditions. Recent advances in pulse measurement techniques, such as frequency-resolved optical gating (FROG), allow measurement of the full electric field of the pulse and have made detailed investigations of short-pulse propagation effects feasible.

In this thesis, I present detailed experimental studies of my work involving nonlinear propagation of femtosecond pulses in bulk media. Studies of plane-wave propagation in fused silica extend the SHG form of FROG from a simple pulse diagnostic to a useful method of interrogating the nonlinear response of a material.

Studies of nonlinear propagation are also performed in a regime where temporal pulse splitting occurs. Experimental results are compared with a three-dimensional nonlinear Schrödinger equation. This comparison fuels the development of a more complete model for pulse splitting.

Experiments are also performed at peak input powers above those at which pulse splitting is observed. At these higher intensities, a broadband continuum is generated. This work presents a detailed study of continuum behavior and power loss as well as the first near-field spatial-spectral measurements of the generated continuum light. Nonlinear plane-wave propagation of short pulses in liquids is also investigated, and

a non-instantaneous nonlinearity with a surprisingly short response time of 10 fs is observed in methanol. Experiments in water confirm that this effect in methanol is indeed real. Possible explanations for the observed effect are discussed and several are experimentally rejected.

This thesis applies FROG as a powerful tool for science and not just a useful pulse diagnostic technique. Studies of three-dimensional propagation provide an in-depth understanding of the processes involved in femtosecond pulse splitting. In addition, the experimental investigations of continuum generation and pulse propagation in liquids provide new insights into the possible processes involved and should provide a useful comparison for developing theories.

“Truth gains more even by the errors of one who, with due study and preparation, thinks for himself than by the true opinions of those who only hold them because they do not suffer themselves to think.” –John Stuart Mill

Acknowledgements

First and foremost, I would like to acknowledge and thank my advisor, Tracy Clement. Although graduate school rules prevent her from being listed as such, Tracy has served as my primary advisor for the duration of the work presented in this thesis. Tracy took me on as her first graduate student despite the fact that my background in physics was nearly non-existent. With much patience and effort, she was able to bring me up to speed quickly. I am very grateful for the opportunities and guidance she has provided. I would also like to thank her for sticking by me even when her own life took her in a new direction.

I would also like to thank Carl Koval of the Chemistry department for facing the angry mob and encouraging me to continue with my graduate studies during a particularly difficult time. Carl is one of the department's greatest assets, and should be acknowledged as such. JILA and especially Steve Leone deserve my gratitude for providing me with support after Tracy accepted a new position. I am thankful that you kept me from slipping through the proverbial cracks, allowing me to complete this degree.

There are several people who contributed both to the work in this thesis and to my development as a scientist. Scott Diddams is the post-doc with whom I worked on several projects. Scott is a very capable scientist whose leadership and ability to explain complicated concepts in an understandable fashion are remarkable. I would like to extend a special thank-you to Alex Zozulya who developed much of the theory

to explain our experimental data. I would also like to thank Amy Van Engen for many enlightening and enjoyable discussions. Amy often served as a sounding-board for my ideas and helped me to refine and develop them. Amy was also always available as a friend in both good and bad times. Amy, you are a wonderful and unique person, and I will always treasure your friendship.

This brings me to the people "behind the scenes" who have provided comfort, support and friendship through some very stressful and difficult times. Two very special people who deserve mention are my sister, Mandi, and Lisa LePome. Mandi moved to Colorado after my first year of graduate school. Since then she has been a constant source of encouragement, laughter, good food, nice clothes, and friendship only a sister could offer. Over the years she has become one of my closest friends and I will be very sad to leave her. I met Lisa my first year in graduate school and then shared a house with her for four years. Despite this, she still left for graduate school in chemistry this fall. Lisa is one of the most caring, fun and bizarre people I have ever had the pleasure of knowing. Her zany personality made me laugh through even the darkest hours. Lisa, if you ever need them, I'm sure we can find some foggy hills somewhere.

I would also like to mention my friends in JILA and chemistry who have made my graduate tenure more enjoyable. It would be difficult to name everyone who has contributed to my happiness here, so I will only briefly mention a few people with whom I have spent the most time. I have been fortunate to share an office with four very wonderful, intelligent and (admittedly) strange people. Sebastian, Joanna, Elizabeth and Amy, you have been a source of great support and entertainment. I will never forget the camaraderie or the many office sports that developed. Thank you for everything. I owe the good fortune of years of Friday night outings, canoe trips and other fun adventures to Brad and Julie Paul. Keep those pictures off the web! (That goes for you too Lori!) I would like to thank Matt Taubman for his encouragement in both exercising regularly and consuming lots of good food as a reward. Matt, I will miss dancing with

you. I have to say it just one more time: “Hustle me baby!” And, I would also like to thank Jason Ensher for his friendship, for getting me involved in soccer, and for introducing me to Brett Esry. Who knew?

Finally, I would like to acknowledge Brett Esry for his unfailing support and patience. It has been a long two years. Thank you, Brett, for waiting for me.

Contents

Figures

Figure

Tables

Table

Chapter 1

Introduction

The first mode-locked pulse laser was demonstrated in 1964 and produced nanosecond (10^{-9} s) pulses [1]. By 1987, pulses as short as six femtoseconds (6×10^{-15} s) had been achieved [2]. Today, commercial laser systems routinely produce sub-100 fs pulses, and these pulses are finding application in a variety of fields. Because of the high peak intensities of short pulses, femtosecond pulse propagation is a field rich in nonlinear phenomena. The short duration of the pulses have made possible the observation of many light-matter interactions that were inaccessible before the advent of short pulse lasers.

The availability of commercial femtosecond laser systems has led to many interesting and challenging problems involving short pulse propagation. First, there are many challenges associated with generating the pulses themselves. There is a demand for shorter pulses, more intense pulses, and pulses at wavelengths ranging from x-ray to infrared. In addition, designer pulses with a specific temporal shape or specific phase function are desired. Femtosecond pulses are currently finding application in many diverse areas of science and medicine. Propagation issues play a role not only in these current-day scientific endeavors, but will also be important for many as yet unforeseen applications.

One obvious application of short pulses is communications. When sending information packets through a fiber or air, shorter pulses mean higher information den-

sity and therefore faster transmission of the data. The high intensities associated with shorter pulses, however, can lead to nonlinear propagation effects and increased temporal spreading or pulse deformation during transmission. Temporal spreading limits the density of pulses that can be sent down a transmission line. It also lowers the peak intensity of the pulses such that, over a long distance, the signal needs to be amplified periodically. Minimizing pulse spreading minimizes the number of amplification stations needed as well as increases the throughput of the system.

The high intensities associated with short pulses can also benefit the communications industry. High peak intensities allow optical switches based on the nonlinear optical response of a material to be constructed. For example, a simple optical switch can consist of a short control beam, a nonlinear material, and a polarizing beam splitter that is crossed with the polarization of the signal beam. When both the temporally short control beam and the signal beam are present in the nonlinear material, a polarization rotation of the signal occurs, allowing it to proceed through the beam splitter. In this way, the signal beam can be switched on and off.

Another example of an application of femtosecond pulses is the generation of high harmonics of the central pulse frequency by focusing an intense pulse into a gas of atoms. Experiments by Zhou *et al.* have found that the duration of the pulse determines the efficiency of harmonic production and that the wavelength of the harmonics can be tuned by adjusting the chirp of the input pulse [3]. High harmonic generation is of interest as a method of generating short extreme-ultraviolet and soft x-ray pulses at a high repetition rate in the laboratory.

Femtosecond pulses are also finding application in ultrafast pump-probe experiments. The short duration of these pulses allows researchers to probe chemical reactions on a femtosecond time scale. Another area of current interest involves using designer femtosecond pulses to tailor atomic or molecular wavefunctions. The idea is to produce and probe coherent atomic wavepackets in a controlled and understandable

fashion.

Short pulses are also being used in many other areas. Some of these include the study of plasma generation and laser-plasma interactions, probing and treating diseased or damaged biological tissues, and the pursuit of new materials with larger nonlinear responses.

All of these applications of short pulses involve propagation through glass or crystal optics, air, other gases, fibers, or liquids such as laser dyes, solvents, or water. If one wishes to understand or control the interaction of a short pulse with any system, it is necessary to have a well characterized pulse, including knowledge of how that pulse changes as it propagates from the source to the sample to the detector. In addition, the nonlinear interactions of short pulses with materials result in complicated phenomena that are intriguing from the standpoint of basic scientific curiosity.

This thesis addresses the linear and nonlinear propagation of ~ 100 fs pulses in bulk media. Most experimental studies of pulse propagation prior to this work provided information on only one aspect of the electric field before and after propagation, usually the spectral or temporal intensity. Knowledge of only the spectral or temporal intensity, however, is not sufficient to fully elucidate propagation effects. Two pulses for example could have the same spectrum or the same intensity autocorrelation and be differently chirped. Only by knowing the phase of the two pulses can they be distinguished. The development of full-field measurement techniques have made possible investigations of pulse propagation involving accurate knowledge of both the amplitude and the phase of a femtosecond pulse. Our approach, therefore, is to measure the full electric field of a pulse before and after traversing the material of interest and thereby glean valuable information about the complex light-matter interactions involved in the propagation. We accomplish this full-field measurement with the second-harmonic generation form of frequency-resolved optical gating (FROG).

Some background information relevant to short pulses and their propagation is

discussed in Chapter 2. This chapter also provides a brief history of pulse measurement techniques leading up to the development of FROG and subsequent advances in technology.

The femtosecond laser system is described and an overview of the experimental procedure is given in Chapter 3. This chapter also presents a discussion of the FROG technique in general and the polarization gating and second-harmonic generation forms of FROG in detail. Specific emphasis is placed on those issues that are important for using FROG as a high dynamic range measurement technique for measuring broadband pulses. Experimental data illustrating the capabilities of FROG as a propagation technique are also presented.

Propagation in fused silica is investigated in Chapters 4 and 5. Propagation is investigated in both a one-dimensional, plane-wave regime and in a regime where self-focusing leads to complicated spatio-temporal dynamics including pulse-splitting and continuum generation. Experimental results are compared with a model based on the nonlinear Schrödinger equation. At the highest powers investigated, spectral bandwidths after propagation become so large that FROG measurements are no longer practical. In this case, we present observations of continuum behavior as a function of input power and time. This chapter also presents the first near-field spatial-spectral measurements of the continuum. Measurements in both chapters provide insight into the nature of short pulse propagation in fused silica and add significantly to the battery of experimental data available for comparison with advancing theories.

Propagation in liquid media is also investigated, and these results are reported in Chapter 6. Studies in methanol reveal the presence of a non-instantaneous nonlinearity with a very short response time. Studies in water lend credibility to the observed nonlinear response in methanol and provide a measure of the nonlinear index of refraction.

Finally, Chapter 7 provides a summary of the science presented in this thesis and discusses future directions.

Chapter 2

Background

Some background is necessary for understanding the concepts presented in this thesis. This chapter attempts to provide the reader with the information necessary to understand later chapters. Relevant references are included for the interested reader. The first section presents a brief discussion of the nature of short pulses. Section 2.2 addresses issues related to the linear and nonlinear propagation of these short pulses. In the final section, a brief history of pulse measurement techniques demonstrates the timeliness of these measurements and provides a motivation for the technique we have chosen.

2.1 Short Pulses

A light pulse can be described as a group of optical cycles under a pulse envelope. A short pulse in time necessarily has a broad spectral bandwidth as a result of the Fourier relationship between time and frequency. A shorter pulse requires a larger frequency bandwidth than a longer pulse. For a given pulse length in time, the minimum spectral bandwidth can be calculated using the time-bandwidth product. For a Gaussian pulse and using FWHM of intensity values of the time and spectral bandwidth, the minimum time bandwidth product is 0.441. Using rms values, the minimum time-bandwidth product for a Gaussian is pulse is 0.5. Reference [4] gives a table of the minimum time-bandwidth products for a variety of common pulse shapes. Pulses with a

time-bandwidth product close to the minimum value are said to be "transform-limited". A transform-limited, 100 fs pulse spectrally centered at 800 nm has a spectral FWHM of roughly 9.5 nm.

A short pulse can be described as a carrier frequency, ω_0, and a complex Gaussian envelope of the form:

$$\mathcal{E}(t) = \exp(-at^2)\exp[i(\omega_0 t + bt^2)]. \tag{2.1}$$

In this equation, $\exp[i(\omega_0 t + bt^2)]$ is the time-varying phase shift of the sinusoidal signal within the Gaussian pulse. The total instantaneous phase is then

$$\Phi_{tot}(t) = \omega_0 t + bt^2.$$

The rate at which the total phase propagates forward in time is the instantaneous frequency and is defined as the derivative of the phase with respect to time:

$$\omega(t) \equiv \frac{d\Phi_{tot}(t)}{dt}.$$

For the Gaussian pulse in Eq. 2.1,

$$\omega(t) = \frac{d}{dt}(\omega_0 t + bt^2) = \omega_0 + 2bt. \tag{2.2}$$

If $b \neq 0$, then the instantaneous frequency varies linearly in time. In other words, the component frequencies of the pulse are ordered in increasing or decreasing fashion in time. Such a pulse is said to be chirped. The term "chirp" comes from the sound a bird makes when it chirps. In that case, acoustic frequencies increase or decrease with time. In Eq. 2.2, b is called the chirp parameter and provides a measure of the chirp of the pulse. The presence of chirp increases the time-bandwidth product of a pulse by a factor of $\sqrt{1 + (b/a)^2}$. Therefore, by propagating a chirped pulse through a medium such that the different frequencies travel at different speeds and the chirp is reduced or eliminated, the pulse can be compressed in time. Equation 2.2 also illustrates that

a linear frequency chirp (linear with respect to time) occurs as a quadratic term in the phase. This point will be relevant when examining data presented in later chapters of this thesis.

2.2 Short Pulse Propagation

As a pulse propagates, the velocity at which the carrier frequency travels through a dispersive medium is called the phase velocity. The phase velocity is determined by the propagation constant, k, evaluated at the carrier frequency. The propagation constant is given by $k = 2\pi n/\lambda_0$ where n is the index of refraction of the material. The velocity at which the envelope travels is called the group velocity. The group velocity is given by the first derivative with respect to frequency of the propagation constant. When the group velocity itself is frequency dependent, the component frequencies of the pulse travel at different velocities. This frequency dependent group velocity is known as group velocity dispersion (GVD). GVD leads to changes in pulse shape, such as compression or stretching in time, as a pulse propagates. GVD is given by the second derivative of the propagation constant with respect to frequency. Since k goes as n/λ_0, a plot of n versus the free-space wavelength, λ_0, reveals regions of positive and negative GVD. Positive or normal dispersion occurs at wavelengths where the curve is concave up – where the second derivative is positive. Downward curvature indicates regions of negative, or anomalous dispersion. At visible wavelengths, most common optical materials exhibit normal dispersion. With normal GVD, red-shifted frequencies travel faster than blue-shifted frequencies, leading to an upchirped pulse.

Propagation of an electromagnetic wave can be described by starting from Maxwell's

equations for a neutral, non-magnetic, dielectric medium:

$$\begin{aligned} \nabla \times \boldsymbol{E} &= \frac{-\mu_0 \partial \boldsymbol{H}}{\partial t} \\ \nabla \times \boldsymbol{H} &= \frac{\partial \boldsymbol{D}}{\partial t} \\ \nabla \cdot \boldsymbol{B} &= 0 \\ \nabla \cdot \boldsymbol{D} &= 0. \end{aligned}$$

For non-magnetic media,

$$\boldsymbol{B} = \mu_0 \boldsymbol{H}.$$

And the electric displacement, $\boldsymbol{D}$, is given by

$$\boldsymbol{D} = \epsilon_0 \boldsymbol{E} + \boldsymbol{P}.$$

$\boldsymbol{P}$ represents the polarization, in units of electric dipole moment per unit volume, of the medium and is the only term in Maxwell's equations that relates directly to the medium. In the above equations, μ_0 is the permeability of free space, and ϵ_0 is the permittivity of free space. Taking the curl of $\nabla \times \boldsymbol{E}$ with

$$\begin{aligned} \frac{1}{\sqrt{\mu_0 \epsilon_0}} &= c \qquad \text{and} \\ \nabla \cdot \boldsymbol{E} &= 0 \qquad (\text{transverse waves}) \end{aligned}$$

gives the one-dimensional inhomogeneous wave equation:

$$\nabla^2 \boldsymbol{E} - \frac{1}{c^2} \frac{\partial^2 \boldsymbol{E}}{\partial t^2} = \frac{1}{\epsilon_0 c^2} \frac{\partial^2 \boldsymbol{P}}{\partial t^2}. \tag{2.3}$$

If the polarization, $\boldsymbol{P}$, is linear in the applied field, then the propagation is linear. This linear response of the medium is simply the index of refraction. If the applied field is strong enough, $\boldsymbol{P}$ can become nonlinear in the applied field. This is what is meant when one discusses nonlinear propagation. A good introduction to nonlinear optics can be found in Chapter 17 of Ref. [5]. A simplified description of some of the

basic concepts that will be important for understanding the work presented in this thesis follows.

$\boldsymbol{P}$ can be expressed as a series expansion in the applied field:

$$\boldsymbol{P} = \chi_1 \epsilon_0 \boldsymbol{E} + \chi_2 \boldsymbol{E}^2 + \chi_3 \boldsymbol{E}^3 + \cdots.$$

In this expression, χ_n provides a measure of the strength of the linear or nonlinear process and is called the susceptibility. As is expected with a series expansion, higher order susceptibilities have decreasing strength. In other words, higher order nonlinearities require a stronger field to have any effect on the propagation. It is for this reason that nonlinear optical processes were largely inaccessible to researchers prior to the availability of lasers. Commercial femtosecond lasers now routinely produce pulses with peak intensities on the order of 10 $\mathrm{GW/cm^2}$ or higher.

The second order nonlinearity, $\chi_2 \boldsymbol{E}^2$, is responsible for second-harmonic generation and optical parametric amplification among other things. Both of these effects arise from a transfer of energy between electromagnetic fields of different frequencies within the material such that

$$\omega_3 = \omega_1 + \omega_2.$$

Second-harmonic generation is a special case of this general expression, where $\omega_1 = \omega_2$. In this case, light at the fundamental frequency is converted to light at the second harmonic frequency: $\omega_3 = 2\omega_1$. In parametric amplification, the opposite effect occurs. Fundamental light at ω_3 causes the generation of light at $\omega 1$ and ω_2, where ω_1 and ω_2 are not necessarily equal. Second order nonlinearities only occur in non-centrosymmetric materials such as Beta-Barium Borate (BBO), Potassium Dihydrogen Phosphate (KDP) and Lithium Niobate. A list of the second order nonlinear coefficients of some commonly used crystals can be found in Ref. [6].

The third order nonlinearity is active in all materials, regardless of symmetry, and gives rise to some interesting effects, including four-wave mixing, Raman scatter-

ing, and the optical Kerr effect. Four-wave mixing includes all processes where one frequency is created from the combination of three other frequencies. For example, the situations $\omega_4 = \omega_1 + \omega_2 + \omega_3$, $\omega_4 = \omega_1 + \omega_2 - \omega_3$, $\omega_4 = -\omega_1 - \omega_2 + \omega_3$ etc. are all classified as four-wave mixing. Third-harmonic generation is a special case of four-wave mixing in which $\omega_1 = \omega_2 = \omega_3$, and $\omega_4 = 3\omega_1$. The Raman nonlinearity is also a version of four-wave mixing in which a molecule makes a transition between two states. Figure 2.1 illustrates this process. A pump photon excites the molecule into a higher energy virtual state from which the molecule immediately drops back down to either state 1 or state 2. Raman scattering occurs when the molecule ends up in a different state than it was initially such that $\omega_f = \omega_p - \omega_{1-2}$ (Stokes) or $\omega_f = \omega_p + \omega_{1-2}$ (anti-Stokes). In the preceding equations, ω_f represents the emitted frequency, ω_p represents the pump frequency, and ω_{1-2} represents the energy difference, expressed in terms of frequency, between states 1 and 2. Raman scattering can occur as either a spontaneous or stimulated process. Since at thermal equilibrium most molecules will initially be in the lower of states 1 and 2, more light will scatter into the lower frequency (Stokes) emission than into the higher frequency (anti-Stokes) emission. As a result, the Raman nonlinearity should result in a shifting of pulse frequencies to the red.

The optical Kerr effect is a result of anharmonic motion of bound electrons in the material and results in an intensity dependent refractive index. The index of refraction of the material is then described by $n = n_0 + n_2 I$ where n_0 is the linear index of refraction and $n_2 I$ is the intensity dependent nonlinear index of refraction. The optical Kerr effect is responsible for three important phenomena in nonlinear pulse propagation: self-phase modulation (SPM), self-focusing (SF), and self-steepening(SS).

Self-Phase Modulation In self-phase modulation, the time-varying index of refraction produces a time dependent phase modulation of the pulse and thereby contributes to spectral broadening of the pulse. Consider the propagation-induced phase of

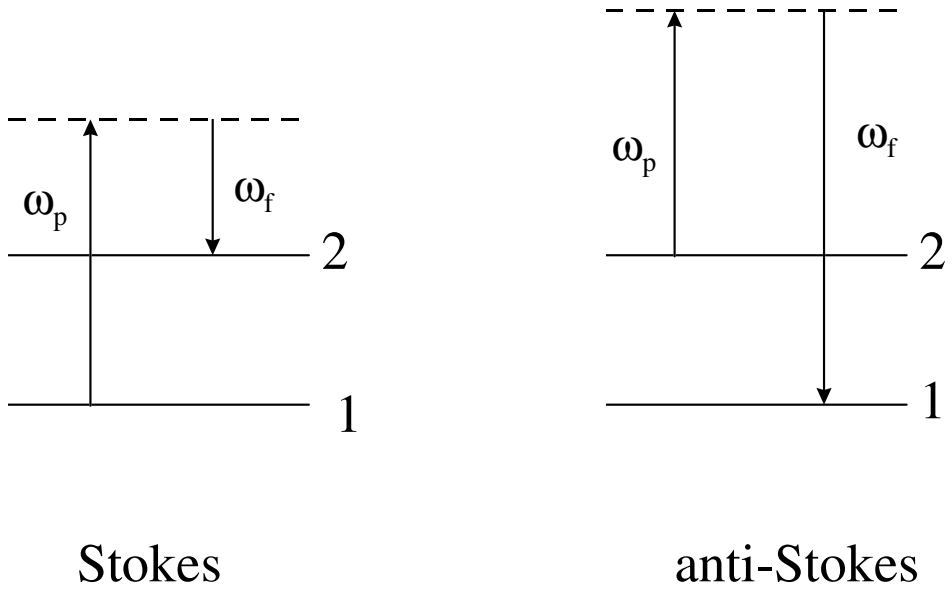

Figure 2.1: Schematic diagram of the Stokes and anti-Stokes Raman scattering processes.

a pulse:

$$\Phi(t) = \omega_0 t - kz$$

where k is the propagation constant, z is the propagation distance through the medium, and ω_0 is the center frequency of the pulse. For a medium of length L, the phase after propagation is given by:

$$\Phi(t) = \omega_0 t - \frac{2\pi n}{\lambda} L$$

where n is the total index of refraction given by $n = n_0 + n_2 I$. Now, the instantaneous frequency is the derivative of the phase with respect to time which is given by:

$$\frac{d\Phi}{dt} = \omega_0 - \frac{2\pi L}{\lambda} \frac{dn}{dt}$$

or

$$\frac{d\Phi}{dt} = \omega_0 - \frac{2\pi n_2 L}{\lambda} \frac{dI(t)}{dt}.$$

The instantaneous frequency, therefore, goes as the negative of the derivative of the intensity profile with respect to time. Assuming n_2 is positive, this leads to a lowering of frequencies on the leading edge of the optical pulse and an increase in frequencies at the trailing edge of the pulse. A pulse with a smooth Gaussian envelope will thus acquire a roughly linear frequency chirp across the central region of the pulse. This situation is illustrated in Fig. 2.2. Note that SPM is similar to GVD in that it produces a frequency chirp. However, SPM actually shifts some of the component frequencies of the pulse to new frequencies while GVD only rearranges the component frequencies.

Self-Focusing Self-focusing is a nonlinear effect that results in a spatial focusing of the beam as it propagates. SF is also a result of the optical Kerr effect. If n_2 is positive, then the higher intensity regions of the pulse experience a larger index of

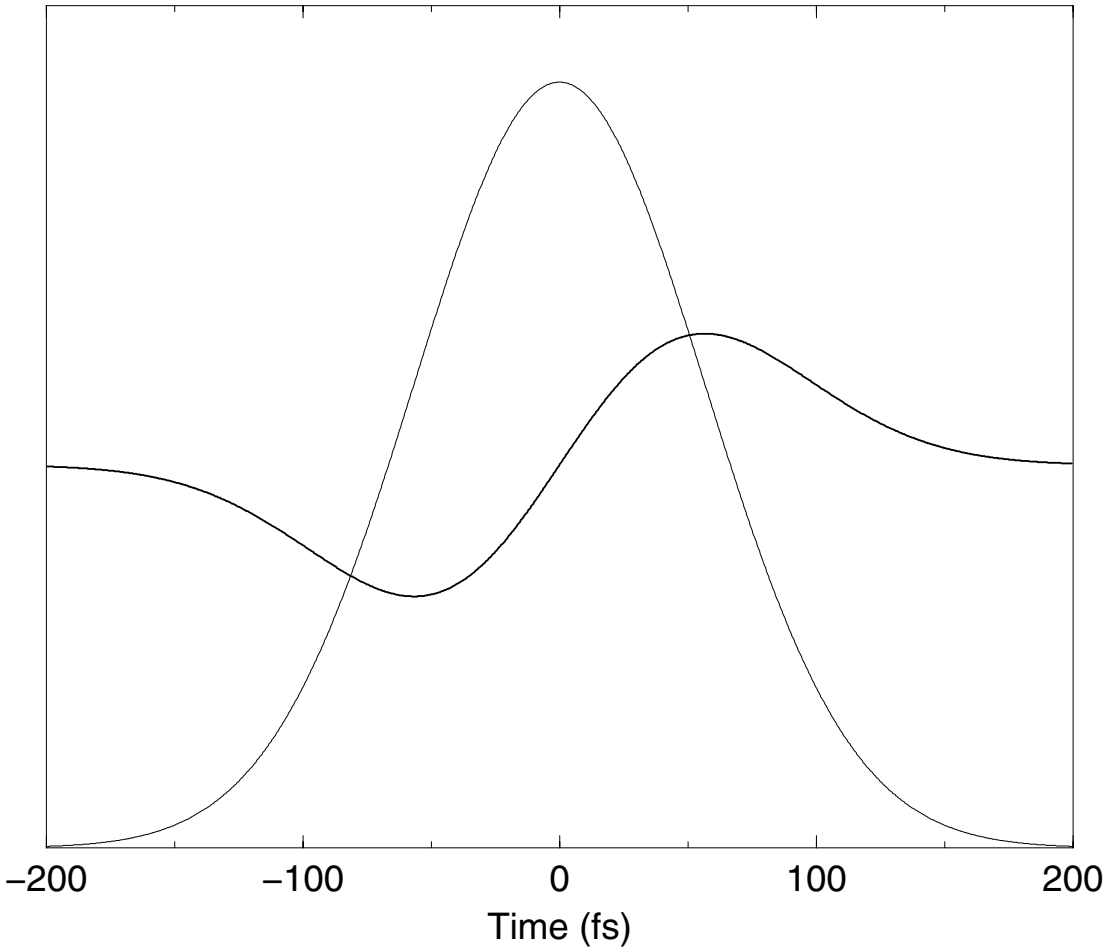

Figure 2.2: A Gaussian function and the negative derivative of that Gaussian. The derivative illustrates the change in frequency a Gaussian pulse experiences as a result of SPM.

refraction than the lower intensity wings of the pulse. In this way, the pulse transforms the medium into a weak positive lens. As the pulse is focused, the center becomes more intense leading to a higher index of refraction and an even stronger positive lens. In this manner, self-focusing can become a large effect very quickly. This type of SF is known as whole beam self-focusing. In similar fashion, any small spike or ripple on the pulse envelope can be magnified greatly and seriously distort the original pulse shape. This type of SF is known as small-scale self-focusing. Either type of SF can be catastrophic in an optical system. The high intensities present in the focusing pulse can be sufficient to damage most optical elements. Two important quantities associated with SF are the critical power for self-focusing, given by $P_{crit} = (0.61\lambda)^2\pi/(8n_0n_2)$, and the self-focusing distance, $z_f = w_0\sqrt{n_0/(n_2 I)}$ [7].

Self-Steepening Self-steepening refers to the steepening of one of the pulse edges in the temporal domain during propagation. This pulse edge deformation is accompanied by an asymmetry in the pulse spectrum [8]. SS occurs as a result of an intensity dependent group velocity. The group velocity decreases with increasing intensity as a result of the intensity dependent index of refraction. The leading and trailing edges of the pulse therefore travel faster than the central portion, leading to a steepening of the trailing edge of the pulse in the temporal domain.

Nonlinear Schrödinger Equation The basic equation describing propagation in a weakly nonlinear medium is the one-dimensional nonlinear Schrödinger equation (NLSE):

$$\frac{\partial \mathcal{E}}{\partial z} + i\frac{k''}{2}\frac{\partial^2 \mathcal{E}}{\partial t^2} - i\frac{2\pi n_2}{\lambda}|\mathcal{E}|^2\mathcal{E} = 0. \tag{2.4}$$

In this equation, $\mathcal{E}$ is the slowly varying complex amplitude of the field in the reference frame moving at the group velocity. GVD is determined by k'', and the third term gives the optical Kerr effect. The field is normalized such that $|\mathcal{E}|^2$ is the intensity in units of

$\mathrm{W/cm^2}$.

The above mentioned linear and nonlinear effects come into play in various aspects of the research presented in this thesis. Many of these effects play a crucial role in the generation of ultrashort pulses. Second-harmonic generation is the nonlinearity on which the most often used measurement technique in this thesis is based. Linear and nonlinear propagation effects are important in the propagation experiments performed throughout this thesis. The preceding discussion of these effects should provide the reader with the background necessary to understand the science presented in this thesis.

2.3 History of Short Pulse Measurement

To interrogate the processes involved in propagation of femtosecond pulses, it is first necessary to be able to measure the pulses themselves. By measuring a pulse before and after traversing the material of interest, one can infer valuable information regarding the materials parameters. Changes in the pulse spectrum, intensity profile, and phase are all important. Also, for numerically modeling pulse propagation, an accurate determination of the peak intensity of the pulse is required. This section provides a brief history of pulse measurement techniques and a description of the full-field techniques available for pulse measurement today.

Acquiring the spectrum of a short pulse is not a difficult task provided one is careful not to distort the pulse spectrum during the measurement. Measuring the temporal duration of the pulse, however, is a more daunting task because measuring a short pulse requires an event that is even shorter. Autocorrelation techniques provide an obvious solution to this quandary because they use the pulse to measure itself. A 1974 publication by Bradley and New [9] provides an excellent overview of the measurement techniques first used to measure short pulses such as linear and nonlinear autocorrelation.

Autocorrelation works by dividing the pulse to be measured into two replicas and then interacting these two replicas over a range of delays to produce a signal. Linear correlation relies on measuring interference fringes between the two pulses while non-linear correlation techniques involve overlapping the two pulses in a nonlinear medium to produce a signal. An example is overlapping the two pulses in a second-harmonic generating crystal. In this case, the signal produced is given by the second-order correlation function: $\int I(t)I(t+\tau)dt$. This signal can be produced in the presence of a constant background or in a background-free configuration. Because a signal will only be observed or enhanced above background while the two pulses are overlapped, these methods give the user some insight into the duration of the pulse. The absolute length of the pulse, however, cannot be obtained. To place any value on the length of the pulse one must first assume a pulse shape. Often a pulse is assumed to be Gaussian or hyperbolic secant squared in shape. If both the autocorrelation and the spectrum are available, the time-bandwidth product gives some insight into phase of the pulse insofar as it confirms the presence or absence of chirp.

Autocorrelations have been performed in a variety of configurations. Because one arm of the autocorrelator is scanned to produce signal over a range of delays, early experiments with short pulses were necessarily multi-shot experiments. In an effort to measure the duration of a single pulse, and not a time average length, researchers turned to performing autocorrelations in laser dyes, observing two photon fluorescence as the signal. Counter propagating pulses led to single shot measurements. The technique, however, did not lend itself to background free configurations and the signal to noise ratio often led to unreliable information. Streak cameras were employed to measure pulses of picosecond and longer duration. Early work also employed ultrafast shutters, where one pulse is used as a gate function, allowing the signal to pass through a Kerr or saturable absorber medium. Borrowing from the field of acoustics in 1971, Treacy first applied the concept of a spectrogram to the optical regime [10]. A spectrogram

is a two-dimensional representation of the pulse as a function of time and frequency. Treacy was, however, unable to retrieve the full intensity and phase of the pulse. Third and higher correlation experiments were also performed in the first attempts to uncover some phase information as well.

As short pulse technology progressed, techniques were developed that could better measure the intensity profile of a femtosecond pulse. Techniques based on four-wave mixing, third-harmonic generation, or a combination of sum- and difference-frequency generation were proposed and implemented to measure complicated or asymmetric intensity profiles [11, 12]. These methods worked well, however they could only measure pulses in the visible. A much later optical Kerr shutter technique allowed measurement of pulse asymmetry and structure of pulses in the UV [13].

Other methods were designed to measure the presence of chirp [14, 15, 16]. These methods, however, were limited either because they used a streak camera and thus were not useful for very short pulses, or they could only resolve whether or not a pulse was chirped. In 1991 Albrecht *et al.* developed a method based on two-photon absorption to characterize the phase function of a pulse up to the fourth order. A separate technique, however, was required to gain any information about the temporal shape or duration of the pulse [17]. Later, Le Blanc and Sauerbrey developed a technique that avoided the use of a nonlinear detector, thus allowing measurement of pulses from the ultraviolet to the XUV. Results of this technique, however, were difficult to interpret, and the technique was only capable of resolving phase shifts of pi or larger [18].

As early as 1985, the first methods to simultaneously measure both the amplitude and phase of femtosecond pulses appeared. The first successful technique was implemented by Diels *et al.* [4]. Theirs is something of a brute force method. The idea is to measure the pulse spectrum, the intensity autocorrelation, and the interferometric autocorrelation and then iteratively fit a pulse to the three results until the process converges to the one pulse that could have produced all three. This technique still requires some

previous knowledge or a reasonable estimate of the functional dependence of the pulse and therefore isn't particularly useful for complicated pulse shapes or modulations. Also, there has been no discussion of the uniqueness of the solution. Naganuma presented a more rigorous variation on this theme and demonstrated that a measurement of the interferometric intensity autocorrelation and the interferogram of the fundamental is mathematically sufficient to reconstruct the pulse with ambiguity only in the direction of time [19]. Later work resolves the time ambiguity by making measurements before and after propagation through a piece of glass [20].

Another method relies on time domain interferometry, but requires a flat phase reference pulse [21]. Diels later introduced a more elegant technique where one applies a known reversible transformation to the pulse to be measured so as to stretch out the signal in time [22]. This pulse is then characterized by interferometric cross correlation with the short version of itself. The fully characterized long pulse is numerically transformed back. In practice this reversible transformation might be propagation through a piece of glass. Of course, this method assumes a full understanding of the processes involved in the propagation as well as accurate parameters associated with these processes. If the pulse is of low enough peak intensity, this assumption is not an unreasonable one.

Each of the preceding measurement techniques for resolving the intensity and phase of a pulse involves measurements in the time domain, in the spectral domain, or in both. The real breakthrough came, however, with techniques involving measurements in a combined temporal-spectral domain. In one of the first optical temporal-spectral measurements, Treacy directly measured chirp in a pulse using time-resolved spectroscopy [23]. Dynamic spectrograms have also been applied to the determination of the presence of temporal asymmetry and chirp in compressed pulses [24]. In fact, it was a spectrographic technique that facilitated the compression of pulses to 6 fs for the first time. Treacy had predicted that cubic phase would be the limiting factor in produc-

ing short pulses [25]. The record in 1987 was 8 fs, produced by grating compression of a pulse spectrally broadened by SPM in a single mode optical fiber [26]. Fork *et al.* produced 8 fs pulses using this method. Then, by mixing six different spectral regions of the compressed pulse with an unbroadened pulse from the amplifier and upconverting each, he was able to measure the relative delay experienced by each frequency component. In this manner he could see that the 8 fs pulse had a residual cubic phase term. By adding a prism pair and adjusting the distances between prisms and gratings, he was able to eliminate both cubic and quadratic phase and achieve 6 fs pulses [2]. Fork's clever measurement technique formed the basis of the first spectrographic pulse measurement techniques.

In 1991 Chilla and Martinez published a combined spectral-temporal pulse measurement technique based on Fork's work that provided the first direct measurement of amplitude and phase [27]. The method first filters the pulse to be measured in frequency, selecting a narrow frequency range. This spectral piece is then cross correlated with a reference pulse to measure delay. By moving the filter and thereby selecting different frequency regions, the derivative of the phase can be found as a function of frequency. An integral yields spectral phase. This information, in conjunction with the power spectrum, gives the spectral amplitude and phase of the pulse. The temporal amplitude and phase are given by Fourier transform. This technique was termed frequency domain phase measurement or FDPM [28].

A similar technique upconverts the pulse to be measured with a spectrally narrow reference pulse [29]. At each value of delay, the spectrum is recorded. The delay at which each wavelength exhibits an intensity maximum is related to the phase. The reference pulse is narrow so that each upconverted sum-frequency corresponds to nearly one frequency component of the pulse to be measured. A rigorous development of the theory behind this technique was presented. This method was experimentally demonstrated to measure only the phase but, in theory, it has sufficient information to

determine the full complex pulse field [30].

Both of the immediately preceding techniques are members of a larger class of techniques whose members are each referred to as a STRUT: spectrally and temporally resolved upconversion technique.

Kane and Trebino introduced a technique similar to FDPM, known as frequency-resolved optical gating or FROG [31]. Instead of temporally resolving spectral slices of a pulse, however, FROG spectrally resolves temporal slices of a pulse. The temporal gating can be accomplished in several ways, but all methods rely on spectrally resolving the signal from an autocorrelation performed in an instantaneously responding nonlinear medium. This measurement yields the spectrogram of the pulse. The intensity and phase of the pulse is then retrieved by means of an iterative two-dimensional phase retrieval algorithm that requires no assumptions about the pulse. The retrieved field has been shown to be essentially unique [31]. The advantage of FROG over the Fourier filtering method of Chilla and Martinez is that it is experimentally simpler and can be extended to a single shot technique. More about the FROG technique can be found in Chapter 3.

Nearly two years after the introduction of FROG, a new technique was introduced by B.S. Prade *et al.* This method is experimentally simpler than FROG and can also be performed in a single shot. The method makes two measurements of the power spectrum of the pulse: one before and one after propagation through a known Kerr medium where the spectrum acquires a complicated fringe structure. A retrieval algorithm starts with an initial guess for the pulse and numerically forward and backward propagates the pulse, replacing the spectrum with the corresponding measured values between each step, until the algorithm converges to a single input that is consistent with both measurements. Uniqueness of the solution is not proven, but the technique has been demonstrated to be robust by introducing known phase distortions on a pulse and then performing the measurement. The technique also provides a measure of the

peak intensity of the pulse assuming the nonlinear index of refraction of the material is known accurately.

In 1995 a method was described that directly measures spectral phase, thus eliminating the need for a retrieval algorithm and the worries of uniqueness [32]. This method, which is essentially the same as a technique developed in femtosecond pulse shaping experiments [33], is called direct optical spectral phase measurement (DOSPM). In DOSPM, the pulse to be measured is spectrally dispersed with a grating. A V-shaped filter then selects two narrow spectral components, one of which is located at the center wavelength. Temporal beat patterns are then measured by cross correlation with a nearly transform limited reference pulse. Phase differences appear as a delay of the center peak of the beat pattern. By varying the height of the V-shaped filter, and thus the spectral component selected, to both positive and negative offsets, the frequency dependent phase can be directly determined. This method, however, gives no information about the amplitude of the pulse. Both DOSPM and the second-harmonic generation form of FROG have been shown to measure phase distortions to within 5% accuracy [34]. DOSPM was later modified to employ a multi-slit arrangement [35]. This arrangement allows for single shot measurement and is capable of measuring more complicated or discontinuous phase profiles.

The preceding techniques are those that were available at the time the investigations presented in this thesis began. For completeness, I mention here other pulse measurement techniques that have since been developed.

Two additional STRUTs have been developed. The first method again overlaps a spectrally narrow $(1.5\ \mathrm{nm})$ reference pulse with the pulse to be measured in a nonlinear crystal to produce an upconversion signal, but it does so in a single shot geometry [36]. The measurement yields a real time group delay spectrogram from which amplitude and phase can be determined using a rapid retrieval algorithm. This method boasts close to real time phase and amplitude displays. It also employs a second-order

nonlinear process and is therefore useful for weak signals. The second method, temporal analysis of spectral components (TASC), is experimentally the same method as FDPM except that it uses a wider slit when selecting spectral components [37]. FDPM is limited to measuring simple phase structures because it discards information on the full temporal dependence of each spectral piece. TASC selects broad enough spectral components that the temporal profile is not determined by the spectral mask. TASC is also a second order technique capable of measuring weak pulses. The method boasts intuitive spectrograms and no time direction ambiguity.

Two methods have recently been introduced to measure not only amplitude and phase but also peak intensity. One technique provides a measurement in the focal region of a pulse and is based on measuring two far-field intensity patterns: one with and one without a known nonlinear material located in the focal spot. This technique was dubbed BRIEFING or beam reconstruction by iteration of an e-field with an induced nonlinearity gauge [38]. A second method involves triple correlation and involves no assumptions about the analytic form of the pulse and uses no iterative algorithms [39].

In the past, femtosecond nonlinear pulse propagation has been studied by spectral observations [40, 41], autocorrelations [42], and cross correlations [43]. Information about the spatial effects of nonlinear pulse propagation have been obtained using the z-scan technique [44, 45]. Although these techniques provide important information, they generally require assumptions about the pulse and they do not provide a measure of the phase. Among the full-field techniques, FROG has emerged as a powerful, robust, and widely-used pulse diagnostic. Although FROG has primarily functioned as a diagnostic technique, it also holds value as a tool for measuring nonlinear materials properties as will be demonstrated in the following chapters.

Chapter 3

Experiment

3.1 Laser System

All of the experiments presented in this thesis were performed using an amplified, femtosecond, Ti:Sapphire laser system. The system consists of an Argon ion laser pumped Ti:Sapphire oscillator, a single-grating pulse stretcher, a Nd:YAG pumped Ti:Sapphire regenerative amplifier, and a single-grating compressor. A schematic diagram of the laser system can be seen in Fig. 3.1. The Argon-ion-laser-pumped Ti:Sapphire oscillator produces $\sim$80 fs pulses, with a central wavelength of 800 nm, at a repetition rate of roughly 100 MHz. The average power out of the oscillator is 400 mW. Pulses from the oscillator proceed into a single grating stretcher where they are spectrally dispersed such that different frequencies travel different path lengths and each pulse stretches out in time. At the output of the stretcher, pulses have a duration on the order of 200 ps. The peak intensity of pulses at this point has dropped by nearly four orders of magnitude. The stretched pulses are then amplified in a Nd:YAG-pumped Ti:Sapphire regenerative amplifier operating at 1 kHz. A single pulse from the amplified pulse train is selected by a Pockels cell in the pulse switchyard, and that pulse proceeds to the compressor. The compressor spectrally disperses the pulse, with different frequencies traveling different path lengths, to compensate for the stretching incurred earlier and to offset any dispersion that occurred in the amplifier and transport optics. The compressed pulses have a duration of 80 fs, a central wavelength of 800 nm, and an average

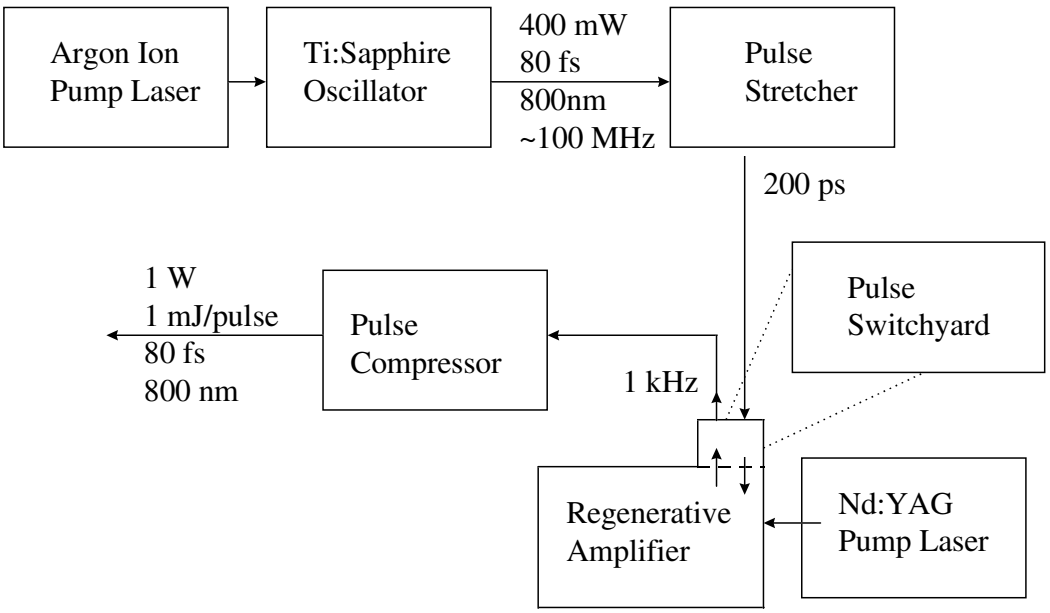

Figure 3.1: Schematic diagram of the amplified Ti:Sapphire laser system.

power of 1 W. The pulses occur at a repetition rate of 1 kHz and have 1 mJ of energy per pulse. The pulses are nearly bandwidth-limited, with a spectral full-width at half maximum (FWHM) of 12 nm. Pulses typically have a small amount of residual cubic phase. Figure 3.2 shows a typical output pulse in both the temporal and spectral domains.

All components of the laser system are fully enclosed and have servo-controlled, heated baseplates to minimize the effects of fluctuations in the ambient environment. Despite these efforts, however, the pulses drift in duration, center frequency, and chirp content with changes in room temperature of as little as 2 degrees Celsius. A temperature drift of more than 2 degrees Celsius often causes the oscillator to cease mode-locking. For these reasons, the room conditions and laser performance must be closely monitored.

Laser performance is monitored in three ways; (1) An Ocean Optics fiber spectrometer observes the center frequency and shape of the spectral intensity profile of pulses from the amplified pulse train by monitoring pulses transmitted through the high-reflectivity end mirror of the amplifier cavity. (2) The transmitted pulses are also detected by a fast photodiode and the pulse train is displayed on an oscilloscope. Changes in relative peak heights of pulses in the train indicate a change in alignment of pulses into the amplifier, and therefore a change in laser performance. (3) The polarization gating (PG) form of frequency-resolved optical gating (FROG) is used to monitor the beam after the compressor. PG FROG provides a nearly real time observation of pulse duration and chirp and will be discussed in more detail later in this chapter.

Aberrations in the calcite polarizers in the pulse switchyard distort the beam profile of the amplified pulses before they are compressed. Figure 3.3 displays contour plots of CCD images of the beam before and after propagation through one of the polarizers. An amplified pulse passes through these polarizers on its way to the compressor. These distortions can result in regions of high spatial intensity or “hot spots” on the

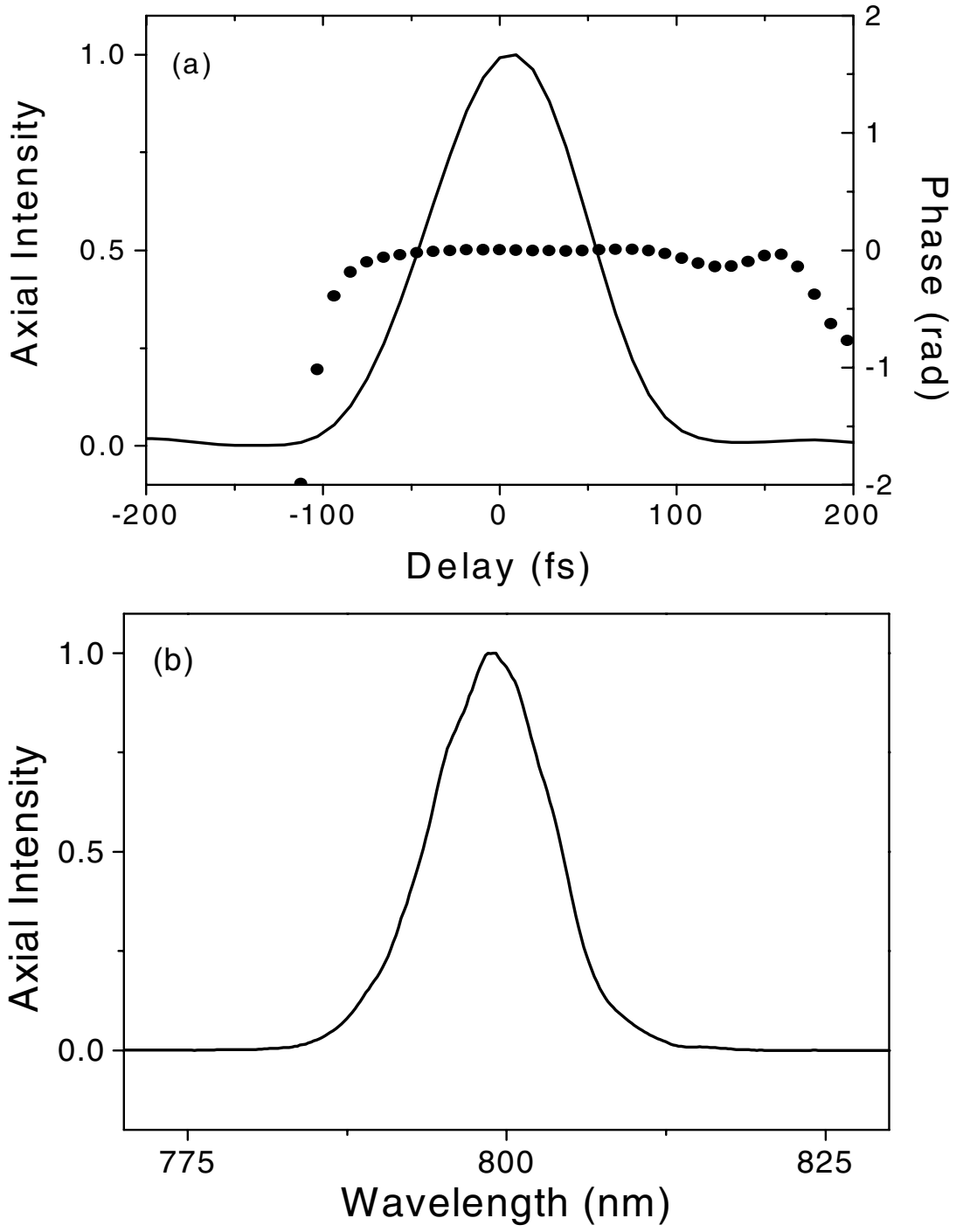

Figure 3.2: A typical pulse from the amplified Ti:sapphire laser system: (a) its temporal intensity (solid line) and phase (points), and (b) its spectrum.

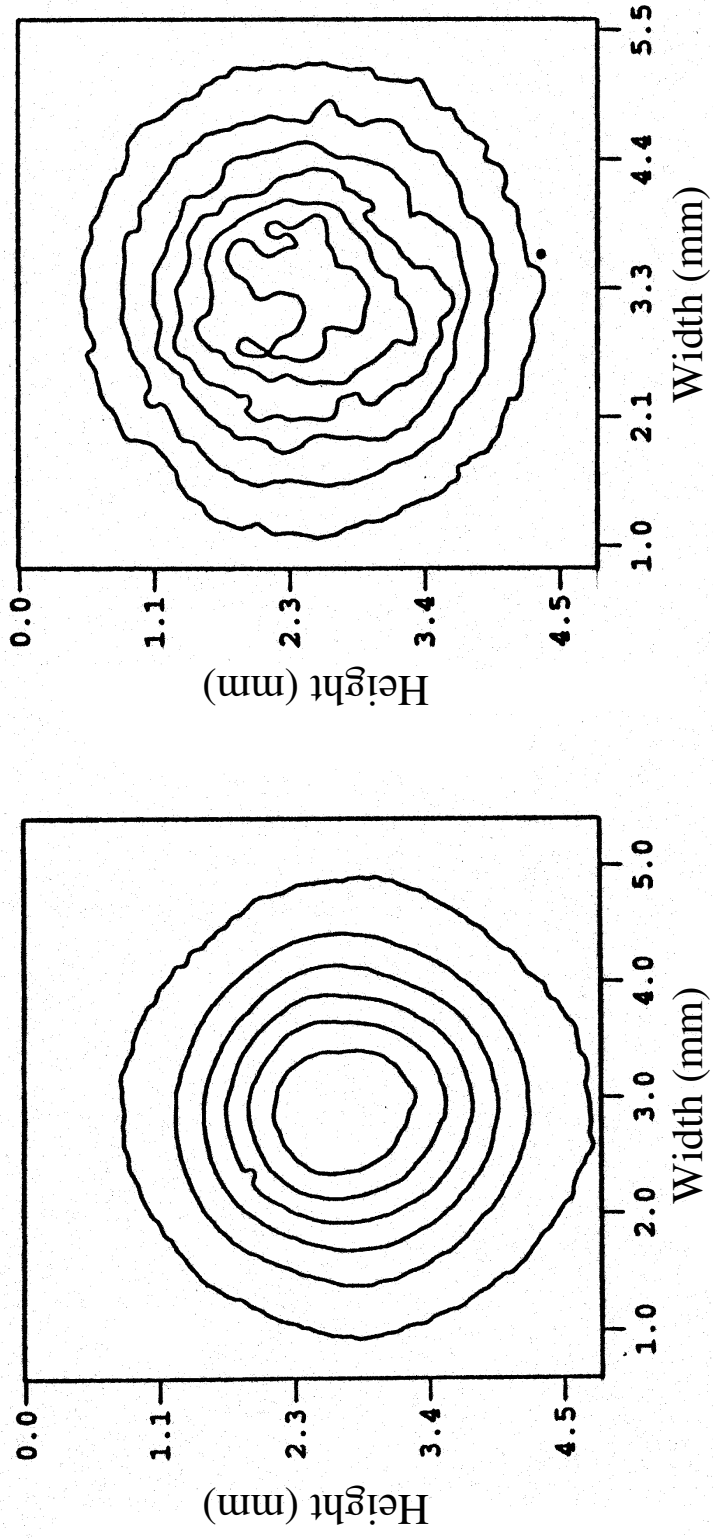

Figure 3.3: Beam profile before (left) and after (right) propagation through calcite polarizers in pulse switchyard.

beam. These hot spots can potentially damage optics and can result in propagation data that is difficult to interpret. Therefore, we spatially filter the beam in order to have a better spatial profile for performing experiments. For experiments in which only a low intensity beam is used, the beam is sent through an ambient spatial filter consisting of a 30 cm focal-length lens, an 80 μm diamond pinhole, and a 15 cm focal-length recollimating lens. In addition, a vacuum spatial filter is used for high intensity beams. A 75 cm focal-length lens focuses the beam into a 300 μm pinhole located approximately at the center of a 1 meter long glass vacuum chamber at a pressure of 2×10^{-2} Torr. A second 75 cm focal-length mirror recollimates the spatially filtered beam outside the vacuum chamber.

A spatial filter works in the following manner. The beam from the laser is mostly Gaussian with some high frequency noise added. Beam propagation through a lens produces the spatial Fourier transform in the focal (or transform) plane such that low frequency components appear closest to the axis and high frequency components appear further out. Insertion of an aperture in the beam selects only the low frequency components. A second lens recollimates the beam and performs the inverse Fourier transform. The beam is now devoid of high frequency noise. In a sense, spatial filters trade high frequency noise for low frequency noise because the top-hat type filtering performed in the focal plane adds some low frequency noise in the spatial wings. This added low frequency noise is convolved with the nearly-Gaussian pulse, however, and is therefore usually quite small. The resulting pulse is more uniformly Gaussian than the input pulse and is far less likely to damage optics or to cause appreciable experimental error due to "hot spots" on the beam. When choosing lens and aperture sizes for a spatial filter, the minimum noise wavelength, n, transmitted by the aperture of diameter d is given by:

$$n = 2\frac{f\lambda}{d}, \tag{3.1}$$

where f is the focal length of the first lens and λ is the optical wavelength of the light. A recommended aperture diameter, d_{opt}, is given by:

$$d_{opt} = \frac{f\lambda}{a}, \tag{3.2}$$

where a is the beam radius prior to the first lens [46]. For an ideal Gaussian pulse, this aperture diameter passes 99.3% of the total beam energy and blocks spatial wavelengths smaller than $2a$. The fraction of power passed through an aperture of diameter d is given by:

$$\frac{P}{P_{total}} = 1 - \exp\left[-\frac{1}{2}\left(\frac{\pi a d}{\lambda f}\right)^2\right]. \tag{3.3}$$

For some experiments, pulses centered at wavelengths other than 800 nm are needed. These pulses are generated by a home-built optical parametric amplifier (OPA) similar to the one described by Yakovlev [47]. A diagram of the OPA is shown in Fig. 3.4. Roughly 1 μJ of the amplified laser beam is selected and focused into a 2 mm thick piece of sapphire to generate a broadband continuum. The continuum serves as a seed for the parametric amplification. The infrared portion of the continuum is collinearly combined with about 500 μJ of 800 nm pump light in a 4 mm thick BBO crystal in a Type-1 phase matching configuration. Different spectral components of the seed beam arrive at the BBO crystal at different times and are phase matched at different angles. By adjusting the delay of the continuum and angle tuning the nonlinear crystal, the desired infrared wavelength can be amplified. The OPA shown in Fig. 3.4 uses a single pass amplification. This OPA can easily be adapted to a double pass configuration with the addition of a dichroic beam splitter, a couple of mirrors, and a translation stage. The OPA can be tuned continuously from 1100 to 1400 nm. Pulses are compressed with a standard prism pair. Typical pulse energies range from 1 μJ to 50 μJ. Figure 3.5 shows the normalized OPA output spectra for several angles of the crystal. Figure 3.6 shows the temporal intensity and phase of a pulse centered near 1200 nm. Short, Gaussian, IR pulses can readily be obtained.

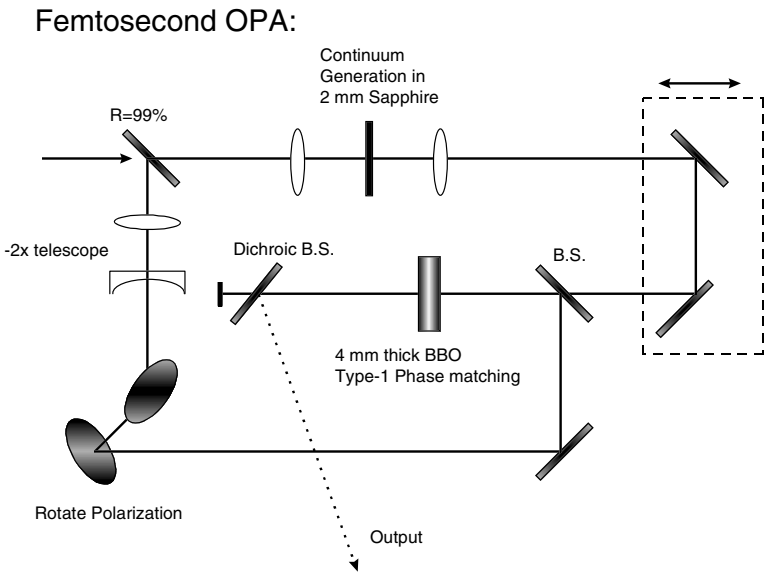

Figure 3.4: Schematic diagram of optical parametric amplifier. The notation B.S. indicates beam splitters and the dotted rectangle indicates a translation stage.

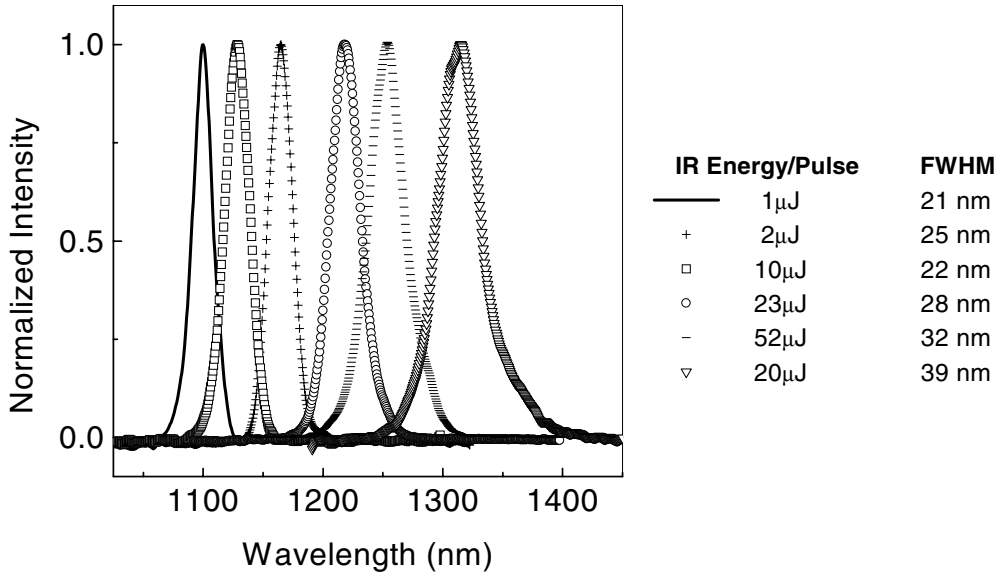

Figure 3.5: Normalized spectra of pulses from the OPA corresponding to different angles of the BBO crystal. The energy per pulse and spectral FWHM are also listed for each case.

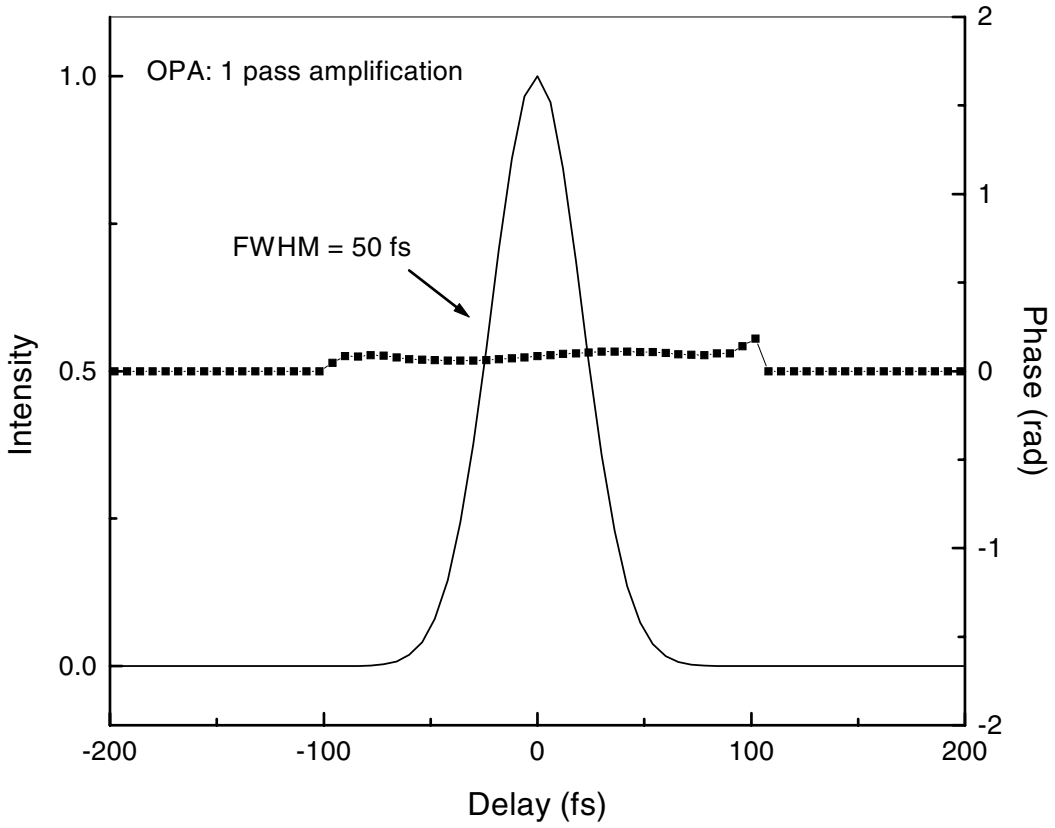

Figure 3.6: Temporal intensity (solid line) and phase (points) for a pulse from the OPA centered spectrally at 1200 nm.

3.2 Overview of Experimental Method

All propagation experiments are conducted using frequency-resolved optical gating (FROG) to obtain the full electric field of the pulses. Specific details of each experiment are presented with the data in later chapters. A brief overview of the experimental method is described here.

Pulses from the compressor are spatially filtered and directed to the entrance of the FROG apparatus. The on-axis portion of the beam is selected using a 1 mm aperture. This beam is measured with FROG and provides the reference field for the experiments. A nonlinear sample is then placed in the beam path prior to the FROG apparatus and a second measurement is made. Comparison of the field after propagation with the reference field gives insight into the processes involved in propagation through that material. Beam size and average power are also measured at the entrance face of the sample. The average power at the entrance face of the sample can be altered by rotating one of a pair of polarizers placed in the beam path before the spatial filter. A brief introduction to FROG as a technique follows in Section 3.3. Specifics of our SHG FROG device and related experimental considerations are presented in Section 3.3.4.

3.3 FROG

Frequency resolved optical gating (FROG) was developed in 1993 as a method for acquiring the full field of a pulse without making assumptions about pulse shape [31, 48]. By full field, we refer only to the axial temporal slowly varying amplitude and phase of a pulse: $\mathcal{E}(t) \propto \sqrt{I(t)}e^{i\varphi(t)}$, and not to the full spatio-temporal field. FROG is a spectrally resolved autocorrelation technique, and yields the spectrogram of the pulse to be measured. A spectrogram, $S(\omega, \tau)$, is a two-dimensional representation of the

pulse as a function of time and frequency:

$$S(\omega,\tau)=\left|\int_{-\infty}^{\infty}E(t)\,g(t-\tau)\,exp(-i\omega t)\,dt\right|^{2}, \tag{3.4}$$

where $E(t)$ denotes the complex electric field, and $g(t-\tau)$ is a variable-delay gate function. The gating can be performed using nearly any instantaneously responding nonlinearity. Experimentally, a FROG device splits the pulse to be measured into two replicas. These two replicas interact in a nonlinear medium yielding an autocorrelation signal. This autocorrelation signal is then spectrally resolved, and the resulting spectrum is recorded on a CCD.

The first FROG apparatus used self-diffraction as the nonlinearity and is referred to as SD FROG [31]. Other FROG devices introduced include polarization gating (PG) [49, 50], second-harmonic generation (SHG) [51, 52], third-harmonic generation (THG) [53], and transient grating (TG) [54] FROG. All of these versions, with the exception of SHG FROG, rely on third order nonlinearities for performing the autocorrelation. SHG is a second order nonlinearity. The spectrogram obtained with each of these geometries is of a different mathematical form. Since in FROG the pulse is used to gate itself, the quantity $E(t)\,g(t-\tau)$ is simply the autocorrelation signal which we will denote $E_{sig}(t,\tau)$.

The signal field in the case of each of the FROG geometries mentioned above are shown below:

$$\begin{aligned}
\text{SD}: \quad E_{sig}(t,\tau) &= E^{2}(t)\,E^{*}(t-\tau) \\
\text{PG}: \quad E_{sig}(t,\tau) &= E(t)\,|E(t-\tau)|^{2} \\
\text{SHG}: \quad E_{sig}(t,\tau) &= E(t)\,E(t-\tau) \\
\text{THG}: \quad E_{sig}(t,\tau) &= E^{2}(t)\,E(t-\tau)\,.
\end{aligned} \tag{3.5}$$

In these expressions, $E(t)$ denotes the complex-valued electric field, and τ is the delay between pulses in the autocorrelation. Depending on which pulse is delayed in TG

FROG, the signal field is mathematically equivalent to that of SD or PG FROG.

In each case, the spectrogram obtained is referred to as the measured "FROG trace". The FROG trace is a plot of intensity versus frequency and time delay. The electric field of the pulse that created the FROG trace can be essentially uniquely determined from the FROG trace. Ambiguities associated with the various types of FROG will be discussed in Section 3.3.2.

Once the FROG trace has been measured, the next step is to retrieve the electric field of the pulse that created the trace. The spectrogram obtained in the FROG measurement can easily be transformed into a two-dimensional phase retrieval problem by a simple change of variables. An in-depth discussion of this transformation can be found in Ref. [55]. The two-dimensional phase retrieval problem is a well known problem in the field of image science. The method of retrieving the intensity and phase of a pulse from the FROG trace is to apply an iterative phase retrieval algorithm. The task of the FROG retrieval algorithm is to find a signal field that satisfies two constraints. The first constraint is that the measured FROG trace must be the squared magnitude of the one-dimensional (1-D) Fourier transform of $E_{sig}(t,\tau)$ with respect to time:

$$I_{FROG}(\omega,\tau) = \left| \int_{-\infty}^{\infty} E_{sig}(t,\tau) \exp(-i\omega t)\, dt \right|^2 . \tag{3.6}$$

The second constraint is the mathematical form of the signal field as given by Eq. 3.5. This constraint is the ability of the calculated field to be generated from a realistic signal field by a known nonlinear optical process. The basic FROG algorithm is as follows. A 1-D Fourier transform algorithm is employed that involves Fourier transforming back and forth between $E_{sig}(t,\tau)$ and $E_{sig}(\omega,\tau)$. The first constraint is applied in the frequency domain, where the magnitude of $E_{sig}(\omega,\tau)$ is replaced by the square root of the measured FROG trace. The second constraint is applied in the temporal domain. This process is iterated until the algorithm converges. Convergence is determined by considering the root mean square (rms) difference between the measured FROG trace

and the trace computed from the retrieved pulse field. When this "FROG error" is acceptably low, the algorithm is said to have converged. The FROG error is computed as a normalized intensity and is therefore unitless. The value of the FROG error at which the algorithm is considered converged differs depending on the type of FROG involved, and the size of the grids used in acquiring and retrieving the FROG trace. For a 128×128 grid, SHG FROG error is typically less than 0.002.

Several versions of the retrieval algorithm for FROG have been published [31, 48, 50, 51, 56, 57, 58]. Some have included an additional constraint in the form of an independently measured spectrum, but this added constraint causes instabilities and stagnation of the algorithm and therefore should not be used [52]. The most robust algorithm available during the time these thesis investigations were performed involves the use of generalized projections. The method of generalized projections basically involves projecting the solution back and forth onto two sets, each of which constitutes the set of all fields that satisfy a particular constraint. In the case of FROG, each of these sets corresponds to one of the two algorithmic constraints discussed earlier. A projection onto the other set involves moving to the closest point inside that set, where the closest point is determined by minimizing a defined distance metric between the two sets. These distance metrics necessarily differ for different FROG types and will not be discussed in detail here. Further information on the application of the method of generalized projections can be found in Refs. [52] and [57]. It should be noted here that generalized projections do not guarantee convergence. However, the method typically has been found to work very well in FROG applications, especially when used in combination with other algorithmic methods. It is interesting to note that the FROG algorithm typically converges fastest when the initial guess for the field is one of random noise, not a Gaussian pulse. The FROG algorithm used for the experiments presented in this thesis combines several algorithmic techniques, switching between methods as each one stagnates. The algorithm we use is a software package available

from Femtosoft technologies. It should be noted that in April of this year, a genetic algorithm was introduced [58]. This algorithm retrieves SHG FROG traces better than the composite algorithm used in these studies. The genetic algorithm is much slower to converge, but converges to lower errors, and is a very promising FROG algorithmic technique.

One reason that the FROG algorithm converges well despite the absence of a guarantee of convergence with generalized projections is that the FROG trace is overdetermined. An electric field sampled at N points has $2N$ degrees of freedom, N in magnitude and N in phase. The FROG trace, however, has N^2 pixels. It is for this reason that a measured FROG trace having a fairly large amount of random noise can still be retrieved well. In fact, the algorithm often converges to a field that produces a less noisy calculated FROG trace [59]. The overdetermined nature of the FROG trace also reveals systematic errors in acquiring the trace by failure of the algorithm to converge [60]. Systematic errors cause nonconvergence because of the physically realizable field constraint included in the retrieval algorithm.

Another very useful feedback mechanism inherent in FROG is the presence of consistency checks of the measured FROG trace. These consistency checks occur in the form of 1-D curves called marginals that are obtained by integrating the FROG trace over the frequency or delay variable. The mathematical form of the marginals obtained depend, of course, on the type of FROG being implemented. Since the SHG form of FROG is used for collecting most of the data presented in this thesis, its marginals are discussed here.

The frequency marginal is obtained by integrating the FROG trace over the delay variable, τ. For the case of SHG frog, the resulting curve is given by [61]:

$$M_{SHG}^{\omega}(\omega) = 2I(\omega) * I(\omega) \tag{3.7}$$

which is simply the autoconvolution of the fundamental pulse spectrum. In Eq. 3.7,

$M_{SHG}^{\omega}(\omega)$ denotes the frequency marginal, and $I(\omega)$ denotes the pulse spectrum. Therefore, all that is needed to perform a consistency check on the FROG measurement is to independently measure the pulse spectrum, calculate the autoconvolution of that spectrum, and compare to the frequency marginal. Not only can this method be used to check for systematic errors, but it is also useful for alignment of the nonlinear crystal in the FROG device and for correcting for phase matching problems that occur in the crystal.

The delay marginal for SHG FROG is obtained by integrating the FROG trace over the frequency variable, ω, and is given by [61]:

$$M_{SHG}^{\tau}(\tau) = \int_{-\infty}^{\infty} I(t)\, I(t-\tau)\, dt \tag{3.8}$$

Equation 3.8 is simply the second-order autocorrelation of the pulse. Hence, a second consistency check is to perform an independent second order autocorrelation and compare to the delay marginal.

3.3.1 Some Practical Issues Concerning FROG

As with any measurement technique, the data must be sampled properly. The FROG sampling rate (FSR) is satisfied when all non-zero FROG data lie completely within the FROG grid, where non-zero is defined as an intensity equal to or greater than 10^{-4} times the peak intensity [60]. In other words, since the temporal and spectral domains are related by a Fourier transform, the time step must be chosen such that the spectrum does not extend off the edge of the FROG grid. The step sizes in the two domains are related by the following expressions:

$$\Delta t = \frac{1}{f_s} \text{ and } \Delta f = \frac{f_s}{n} \tag{3.9}$$

or

$$\Delta t = \frac{1}{n\Delta f} \tag{3.10}$$

where Δt is the temporal sampling interval, f_s is the sampling frequency, Δf is the spectral sampling interval, and n is the number of samples in the temporal and spectral domains. Sampling near the FSR limit allows one to use the smallest possible grid and therefore allows quick algorithmic convergence, however the retrieved field often has a sharp, jagged profile. Since all necessary data are present, more attractive spectral and temporal profiles can be obtained by symmetrically adding zeroes to both ends of the data set in one domain and Fourier transforming to the other. Another obvious way of avoiding jagged retrieved field profiles is to sample data on a larger grid and therefore above the FSR. FROG traces are most visually appealing when both the delay and frequency domains are equally sampled. However, any sampling rate that satisfies the FSR is sufficient.

Careful calibration of the frequency and delay axes is also particularly important. Since the step size in each domain, as well as the central wavelength of the data are used as input parameters in the retrieval algorithm, accuracy of these parameters determines the accuracy of the retrieved field. It has been shown that inaccuracy on the order of 10% in the input parameters introduces roughly 10 to 20% inaccuracy in retrieved pulse parameters such as temporal and spectral FWHM and phase distortion [52]. Since the two domains are related by Fourier transform, an error in any calibration will affect all aspects of the retrieved field.

3.3.2 Ambiguities Inherent in FROG

FROG essentially retrieves the full field of the measured pulse, however there are a few ambiguities inherent in various forms of FROG that should be mentioned. Three ambiguities are inherent in all forms of FROG [31, 48]. The first ambiguity is an arbitrary constant phase factor, which is irrelevant in ultrashort pulse measurements. The second ambiguity is an arbitrary shift in time and is similarly unimportant. The third ambiguity is the distinction between $E_{sig}(t,\tau)$ and $E^*_{sig}(-t,-\tau)$. The latter sig-

nal, however, is not consistent with the mathematical form of the signal field constraint and therefore cannot occur in FROG. Additional ambiguities are specific to various versions of FROG. SHG FROG, for instance, has two important ambiguities. The first of these is the direction of time. Since SHG is a second order technique and produces traces that are symmetric with respect to time, an upchirped pulse cannot inherently be distinguished from a downchirped pulse. The direction of time of the retrieved pulse must be determined independently. Methods for resolving this ambiguity will be discussed in Section 3.3.4. The second SHG FROG ambiguity exists in the relative phase of multiple pulses. In this case relative phases of φ and $\varphi + \pi$ yield the same FROG trace. A similar ambiguity in the relative phase of multiple pulses exists for the THG form of FROG. In this case, however, it is for relative phases of φ and $\varphi \pm 2\pi/3$. For the SD, PG, and TG forms of FROG, no additional ambiguities are known.

It was mentioned previously that the PG form of FROG is used as a pulse diagnostic technique for the work presented in this thesis. PG FROG was chosen as a pulse diagnostic because the associated FROG traces are essentially a graphic display of pulse instantaneous frequency versus time and are thus very intuitive. PG FROG can be used in a single-shot configuration and thus can yield nearly real time qualitative information about the pulse. Figure 3.7 shows simulated PG FROG traces for a flat phase, a downchirped, and an upchirped pulse. The delay axis increases from the top to the bottom of each graph, and the wavelength axis increases from left to right. Intensity is plotted on an arbitrary color scale, with the most intense regions in the center of the FROG trace falling off to lower intensities at the edges of the signal. The approximate temporal duration of the pulse can be determined by observing the width of the signal along the delay axis. With frequent monitoring, the trace is a good indicator of changes in the output of a laser system.

The SD and TG forms of FROG also yield intuitive traces, while SHG and THG do not. The SHG and THG forms however offer higher sensitivity than their more

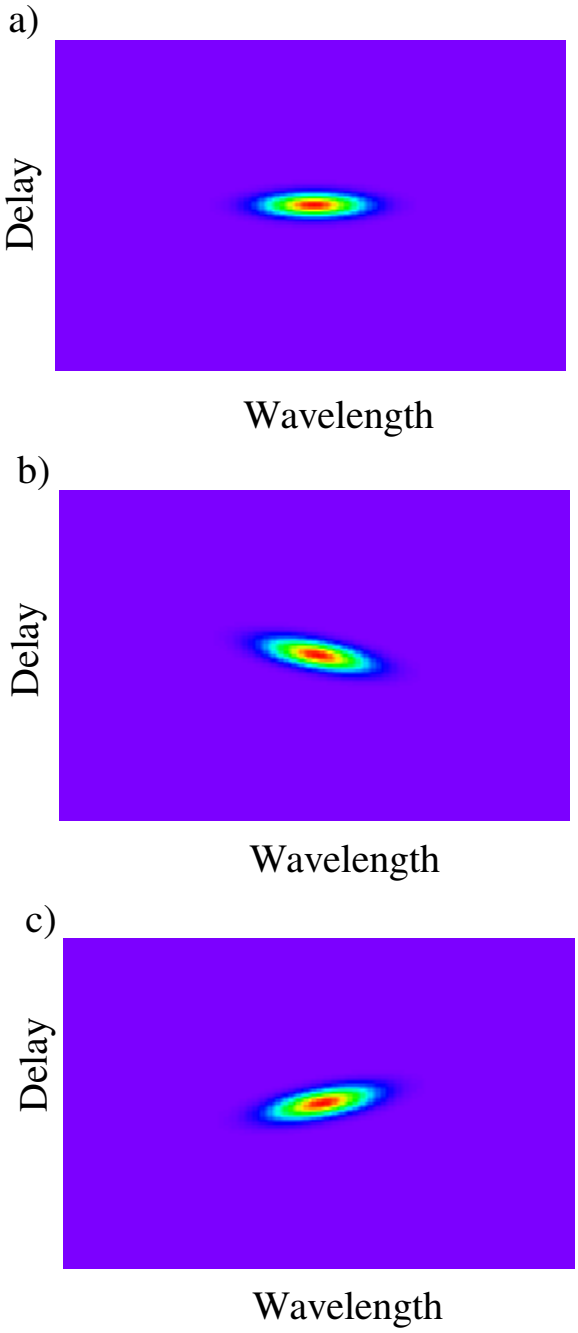

Figure 3.7: PG FROG traces for (a) an unchirped pulse, (b) a downchirped pulse, and (c) an upchirped pulse.

intuitive counterparts. As mentioned earlier, some forms of FROG have important ambiguities as well. The type of FROG used for any application should be chosen to meet the needs of each individual experiment. Table 3.1 gives a summary comparison of the various forms of FROG mentioned here.

FROG techniques are generally simple to implement, insensitive to noise, and provide the user with a full-field characterization of a pulse with only minor ambiguities. The technique can be very broadband and has been implemented for pulses in the ultraviolet, visible, and infrared. FROG was first introduced as a multiple shot technique, but can also be adapted to single shot measurements [49, 62, 63]. FROG has been demonstrated for pulses with energies as low as 1 pJ [55] and when combined with spectral interferometry can measure a pulse train with average energy of only 42 zeptojoules, or 42×10^{-21} J [64]. Since any nearly instantaneously responding nonlinearity can be used, FROG can be tailored to fit individual requirements. Non-instantaneous nonlinearities present in the autocorrelation crystal can also be accounted for in the retrieval process [50]. Since FROG has inherent consistency checks, systematic errors can be easily identified and removed. Recently, efforts have been made to extend FROG to a real-time measurement technique [65, 66], and a method of placing error bars on a FROG measurement has been determined [67].

Several improvements on the basic FROG technique have been invented, some of which have been given excessively cute names. TADPOLE is a combination of FROG and spectral interferometry that allows the measurement of very weak pulses [64]. TREEFROG allows simultaneous recovery of two independent ultrashort pulses from a single spectrogram. TREEFROG has been implemented in a mulitshot configuration using SHG FROG [68] and in a single shot configuration using PG FROG [69]. Multi-pulse Interferometric (MI) FROG is an extension of FROG that allows real-time, single-shot imaging of ultrafast phase shifts. This technique is also capable of resolving three pulses in a single shot [70]. MI FROG has been applied to pump-probe coherent

Table 3.1: Comparison of some common variations of FROG.

	SD	PG	SHG	THG	TG
Intuitive traces?	Yes	Yes	No	No	Yes
Additional advantages:		Automatic phase matching	Very sensitive	Very large bandwidth	Background-free
Disadvantages:	Not phase matched; requires thin nonlinear medium	Requires polarizers	Short wavelength signal	Very short wavelength signal	Involves three beams
Ambiguities:			Time direction; relative phase of multiple pulses: $\varphi, \varphi + \pi$	Relative phase of multiple pulses: $\varphi, \varphi + \frac{2\pi}{3}$	
Sensitivity: (multi-shot, single shot)	1 μJ, 10 μJ	0.1 μJ, 1μJ	1 pJ, 10 nJ	3 nJ, 30 nJ	10 nJ, 0.1 μJ

spectroscopy, measuring ultrafast, high-field ionization rates in gases [71, 72]. A version of FROG using the Kerr nonlinearity in an optical fiber has the same sensitivity as SHG FROG, but it does not have an ambiguity in the direction of time [73, 74]. A version of FROG using cascaded second-order nonlinearities also boasts high sensitivity without the time direction ambiguity [75, 76].

FROG has primarily been applied as a laser diagnostic [77, 78, 79, 80, 81] until recent years when it has been extended to a variety of other scientific endeavors. FROG has been used for the measurement of nonlinear materials properties [82]. It has been applied to understanding modelocking dynamics in external cavity semiconductor diode lasers [83]. It has also been used in the study of relativistic accelerations in plasmas [84] and ionization induced pulse shortening and retardation [85]. FROG has also been used in feedback systems to generate tailored pulses from a compressor [86, 87] and in using tailored pulses to control condensed-phase vibrational excitation [88].

For the purpose of this thesis, I now delve into a little more detail on the PG and SHG forms of FROG in general and discuss the details relevant to our implementation of these devices.

3.3.3 PG FROG

The polarization gating form of FROG is the most intuitive form of FROG and is used in this work as a laser diagnostic. A diagram of the apparatus is shown in Fig. 3.8. The pulse to be measured is split into two replicas. One replica, the probe beam, is sent through a pair of crossed polarizers. The more intense gate beam undergoes a polarization rotation of 45 degrees by out of plane propagation before interacting with the probe beam in a thin piece of fused silica. The gate beam induces a birefringence in the fused silica through the optical Kerr effect. When the probe beam overlaps the gate beam in the fused silica, the probe beam undergoes a slight polarization rotation, allowing a portion of it to pass through the second polarizer to the detector. PG FROG

PG FROG:

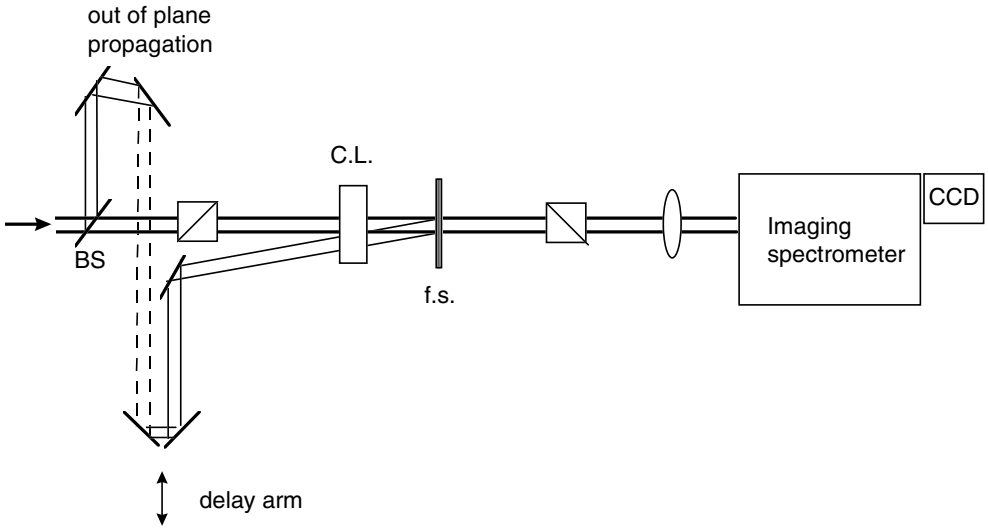

Figure 3.8: Schematic diagram of polarization gating FROG. C.L. denotes cylindrical lens; BS, beamsplitter; and f.s., fused silica. Polarizing beam splitter cubes are drawn as squares with a diagonal line through the center.

can be arranged in a multishot or single shot configuration. Multiple shot configurations rely on scanning one arm through a range of delays. A single shot configuration is used here. In this arrangement, a cylindrical lens focuses both the probe and gate beams to vertical lines in the fused silica. The beams are crossed horizontally at an angle in the fused silica. In this way, each position along the axis of beam overlap corresponds to a specific value of relative delay between the two beams. The entire autocorrelation signal can then be imaged onto the slits of an imaging spectrometer, and the entire FROG trace can be acquired in a single shot with a CCD camera. Although our diagnostic system employs a single shot geometry, because of the speed of the CCD, actual FROG traces are acquired by averaging over several shots. All adjustments to the lasers are made manually, therefore integration over several pulses is sufficient to allow pseudo-real time viewing of how these adjustments affect the output pulses. Pulses are monitored with PG FROG while the length of the compressor is adjusted to set the chirp of the laser pulses to the desired level.

The thickness of the nonlinear medium in PG FROG is important. If the medium is too thick, the pulse to be measured will broaden temporally and acquire a linear chirp on propagation through the glass. If the medium is too thin, the signal will be distorted by an etalon effect. Light can reflect off the back surface of the glass, travel to the front surface, and reflect back into the direction of signal. If the nonlinear medium is too short, the time it takes for the light to travel back and forth in the glass can be shorter than the duration of the pulse. This is especially true for longer pulses such as the ones used in these investigations. For this reason, a 1 mm thick piece of fused silica is used.

The difference in angle of propagation between probe and gate beams should be kept as small as is reasonably possible. This angle is typically less than 10 degrees. As each beam propagates through the crystal it experiences an angle dependent path length, and hence an angle dependent delay. The difference in delay experienced by the two beams leads to a blurring of the time delay at any given spatial coordinate. This

blurring effect also increases with the thickness of the nonlinear medium.

Since, in this single-shot configuration, the delay is mapped to a spatial coordinate, spatial quality of the beams is particularly important [55]. For this reason, if the PG FROG were to be used to obtain more quantitative information, the input beam should be spatially filtered. In our experiments, there was no spatial filtering before the PG FROG device. For this reason, it is likely that comparisons between PG and SHG measurements taken simultaneously reveal inaccuracies in the PG measurement. The retrieved fields from traces acquired in rapid succession with PG FROG also vary appreciably. It is for these reasons that the PG form of FROG is used solely as a qualitative pulse diagnostic in these experiments. Because of its intuitive traces, it serves this purpose well.

3.3.4 SHG FROG

SHG FROG employs a second order nonlinearity and is therefore the most sensitive of the most commonly employed FROG techniques. It is capable of making high dynamic range measurements, making it suitable for propagation experiments where small changes in the low intensity wings of the pulse bear important information about the physics involved in the propagation process. A diagram of the SHG FROG apparatus is shown is Fig. 3.9. The pulse to be measured is split into two replicas using a 1.6 mm thick beamsplitter with a broadband Inconel coating. Front surface metallic reflectors are used to minimize dispersion as the pulse propagates to the frequency-conversion crystal. A 10 cm focal length spherical mirror focuses the two replicas of the pulse into the second harmonic conversion crystal, and the resulting signal at 2ω is imaged onto the entrance slits of an imaging spectrometer. The pulse in one arm of the interferometer is delayed with respect to the other by a stepper-motor controlled translation stage. The spectrum at each delay is recorded with a thermoelectrically-cooled, 16-bit CCD camera. For each value of delay, the signal is averaged over 300 pulses.

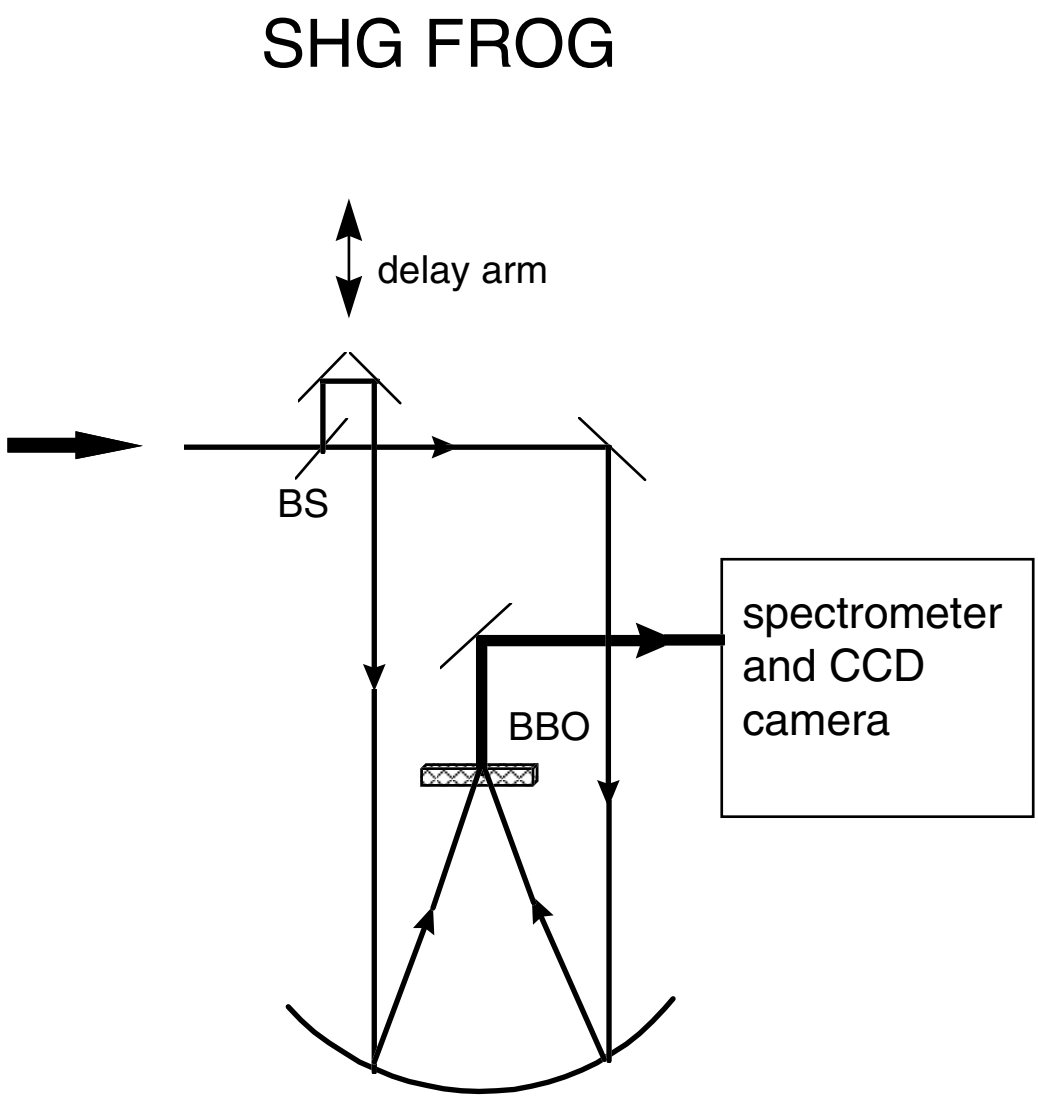

Figure 3.9: Schematic diagram of SHG FROG apparatus. BS denotes the beam splitter; and BBO, the second harmonic generating crystal. (From Ref. [89].)

FROG spectrograms are recorded on 128 by 128 or 256 by 256 grids depending on the spectral content of the pulse to be measured. Typical peak intensities recorded on the camera produce 50,000 counts, while the dark current level is at 970 counts. In addition, the noise level is $\sim$2–5 counts, providing a signal-to-noise ratio of better than 10,000:1. Propagation experiments using SHG FROG are conducted by measuring the pulses with and without a nonlinear sample in the beam.

There are several important issues that should be taken into consideration when using SHG FROG. A good discussion of some of the issues can be found in Ref. [52]. One obvious issue is the ambiguity of the direction of time. This time ambiguity can be removed in three ways: 1) repeat the measurement after chirping the pulse in a known manner, such as propagating the pulse through a glass with known dispersion, 2) propagate through a thin piece of glass such that surface reflections introduce a small pulse behind the main pulse [78], or 3) have some *a priori* understanding of the processes that produced the measured pulse. Initially we chose the first option, propagating the pulse through a 5 cm thick piece of BK-7 glass. As our research progressed, however, we switched to the third option, using information from our developing model of pulse propagation as described in later chapters [90, 91].

As mentioned earlier, SHG FROG yields a trace that is symmetric about delay. One may find it tempting then to only measure half the trace, thereby reducing the amount of time required to complete a measurement. However, if the trace is not centered at the exact zero delay point, some broadening of the measured pulse could result. Also, acquiring half of the trace and numerically inserting the mirror image before running the algorithm has the unfortunate side effect of symmetrizing noise as well. Asymmetric noise will be discarded by the algorithm because of the physically realizable signal constraint, but symmetric noise will remain. Therefore, acquiring only half of a trace, or symmetrizing a fully acquired trace, serves to increase the effects of noise and should thus be avoided. It is also noteworthy that the symmetric nature of the

FROG trace does not imply that only symmetric pulses can be retrieved. The symmetry of the trace has no bearing on the symmetry of the retrieved pulses.

Because SHG FROG is such a sensitive technique, it is imperative to limit the intensity of light being measured. Because of the high intensities present in the focus of the two beams, it is relatively easy to damage the nonlinear crystal. Also, if conversion efficiency in the crystal is too high, depletion of the input fields occurs, invalidating the expression for the signal field: $E_{sig}(t,\tau) = E(t)E(t-\tau)$. In this case, the algorithm will necessarily fail to converge to the correct pulse. A rule of thumb guideline is to keep the peak intensity conversion efficiency below 3% [52].

Propagation of intense femtosecond pulses through several centimeters of a bulk nonlinear medium such as fused silica can result in complicated temporal and spectral intensity profiles, as well as dramatic spectral broadening. As an example, the intensity in the wings of the spectrum after propagation (at wavelengths that are $\geq$50 nm from the spectral peak) can be just three orders of magnitude less than the peak intensity. Compare this to our input pulse, where the intensity spans six orders of magnitude over the same 50 nm spectral region. Because of the large spectral bandwidths of the propagated fields it is important to take into account the finite phase matching bandwidth of the second harmonic conversion process. This finite phase matching bandwidth arises from a phase mismatch between the fundamental and second harmonic frequencies. The conversion efficiency due to phase mismatch is given by [7, 92]

$$\eta = \left[\frac{\sin(\Delta kL/2)}{\Delta kL/2}\right]^2, \tag{3.11}$$

where $\Delta k = (2\omega/c)[n_e(2\omega,\theta) - n_o(\omega)]$, ω and 2ω are the fundamental and second harmonic frequencies, n_e and n_o are the extraordinary and ordinary refractive indices, L is the length of the crystal, and θ is the phase matching angle in the crystal. Therefore, the thinner the crystal, the larger the range of frequencies that can be converted for a given crystal orientation. For lower peak intensity propagation experiments,

where the resulting pulse spectral bandwidth is lower, we use a 100 μm thick piece of $\beta - \mathrm{BaB_2O_4}$ (BBO) as the SHG crystal. For experiments in which high peak intensities lead to dramatically broadened pulses, we use a 50 μm piece of BBO. In both cases, the crystal is cut at an angle of $\theta = 29.1^\circ$ for type-I phase matching at 800 nm. For all experiments, the frequency marginal is used to check and correct for problems associated with the phase-matching bandwidth of the nonlinear crystal.

3.3.5 SHG FROG Data

An example measured SHG FROG trace and the calculated FROG trace corresponding to the retrieved field are shown in Fig. 3.10. The FROG trace was collected and retrieved on a 128 by 128 pixel grid, and the FROG error associated with this retrieval is 0.00312. The measured and retrieved traces match very well, indicating good convergence of the algorithm. A further test of the convergence of the algorithm is to compare the marginals of the measured FROG trace to those of the retrieved trace. A comparison of the marginals for the traces shown in Fig. 3.10 is shown in Fig. 3.11. Agreement is excellent in both the frequency and time domains.

That the measured and retrieved fields are in such close agreement is very good. But it is also important to verify that the measured and retrieved FROG traces correspond to the pulse actually being measured. For this, it is necessary to compare FROG results with independently measured parameters. One comparison that is easy to implement in the laboratory is a comparison between the retrieved pulse spectrum and an independently measured spectrum. An example using the same retrieved field as above is shown in Fig. 3.12. The agreement shown in this figure is typical. The SHG form of FROG is also particularly nice in that its delay marginal is simply the second order intensity autocorrelation of the pulse. As a further demonstration that SHG FROG indeed measures the actual pulse field, an example of an independently measured autocorrelation compared with both the measured and reconstructed delay marginals is shown in

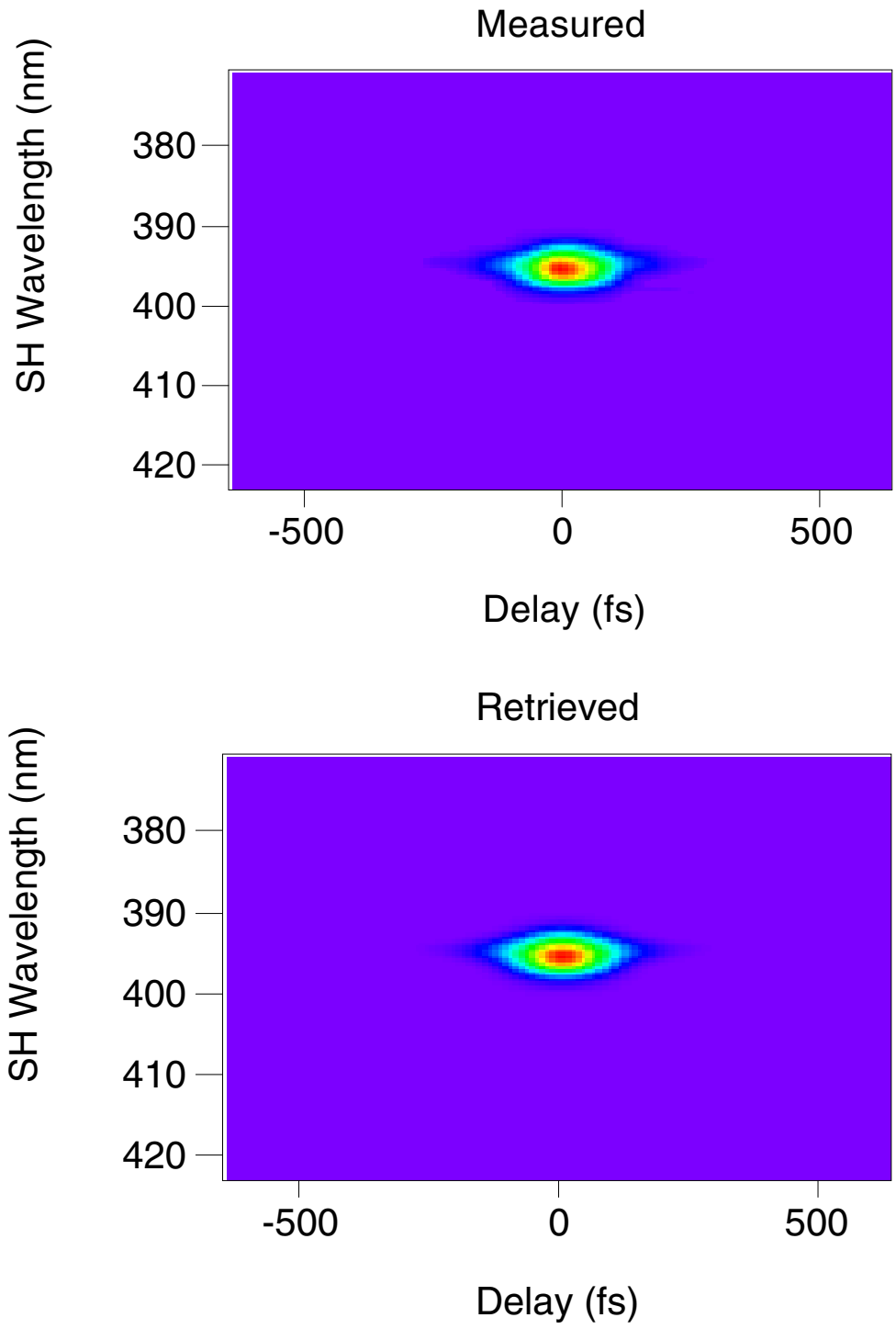

Figure 3.10: A measured SHG FROG trace and a FROG trace calculated from the corresponding retrieved field.

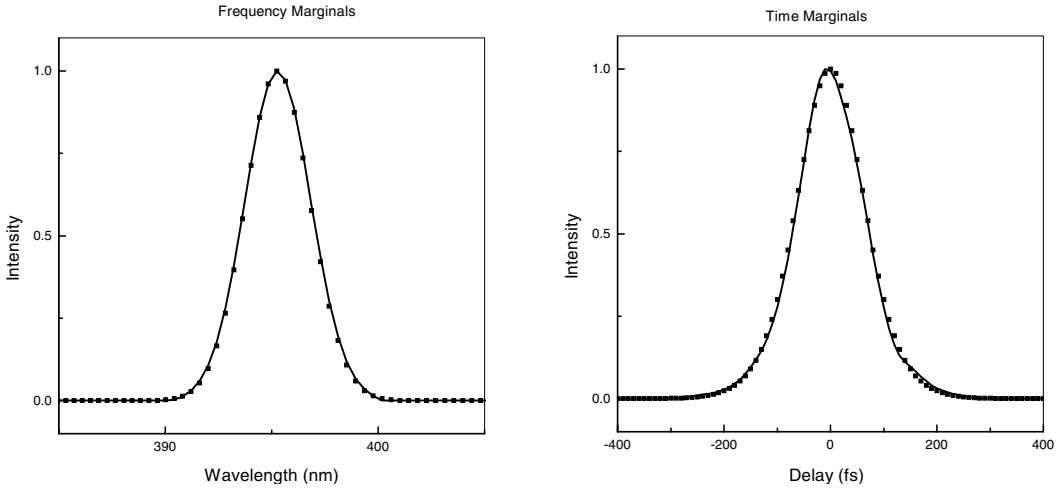

Figure 3.11: Measured (solid lines) and retrieved (points) frequency and time marginals corresponding to the FROG traces presented in Fig. 3.10.

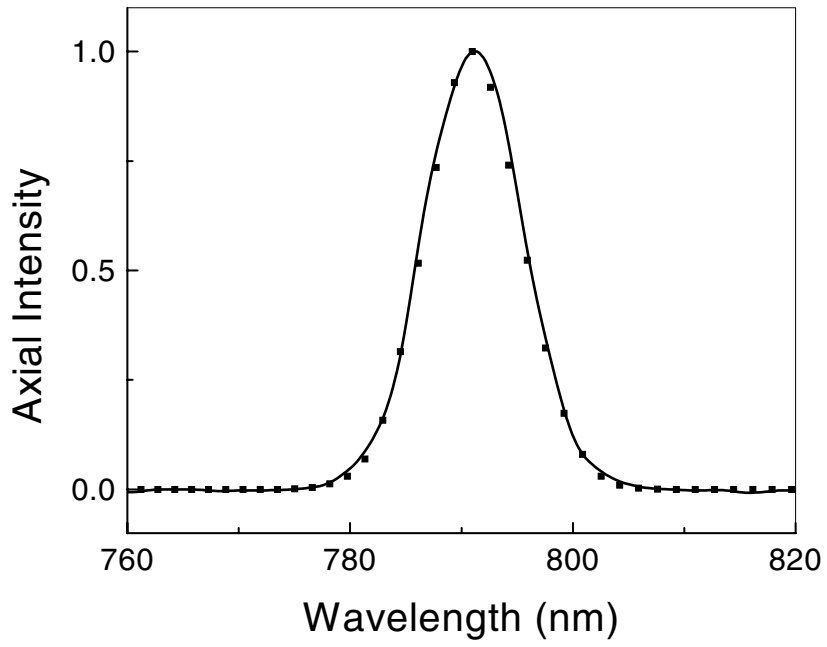

Figure 3.12: Independently measured spectrum (solid line) along with retrieval spectrum (points) for the pulse measured in Fig. 3.10.

Fig. 3.13. Once again, agreement is very good.

Figure 3.14 shows the retrieved fields from two separate measurements. The top graph plots the temporal fields as a function of intensity and phase. The bottom graph plots the retrieved pulse spectra. These two FROG measurements were performed roughly 15 minutes apart and demonstrate the repeatability of the measurement technique.

The preceding measurements were all made using pulses having a relatively narrow spectral bandwidth. As mentioned previously, in propagation experiments one often needs to measure a pulse that has been spectrally broadened appreciably. Even using the thin BBO crystal, phase matching can become an issue. The phase matching efficiency for the 50 μm BBO crystal used in some experiments has a FWHM of 52 nm. The pulses measured in these experiments typically have a bandwidth after conversion to the second harmonic of $\sim$40 nm (FWHM), thus the phase matching bandwidth provided by this crystal is sufficient for conversion of most of the spectrum. However, the conversion efficiency is not constant over the entire bandwidth of the pulse. Figure 3.15 shows the phase matching efficiency curve for 50 μm of BBO cut at an angle of 29.1° for type-I phase matching. Fortunately, this does not present a formidable problem because of the consistency check provided by the frequency marginal. As has been demonstrated previously [78], the FROG trace can be corrected prior to being input into the retrieval algorithm by using the frequency marginal and the autoconvolution of the fundamental spectrum. This correction eliminates bandwidth limitations due to finite phase matching efficiencies, as well as grating and detector responses.

Comparison of the frequency marginal with the autoconvolution of the fundamental spectrum is also used for alignment of the second harmonic conversion crystal. The angle of the crystal is tuned for the smallest difference between the autoconvolution and the frequency marginal. At this angle, there is optimal overlap of the conversion efficiency curve with the second harmonic pulse spectrum.

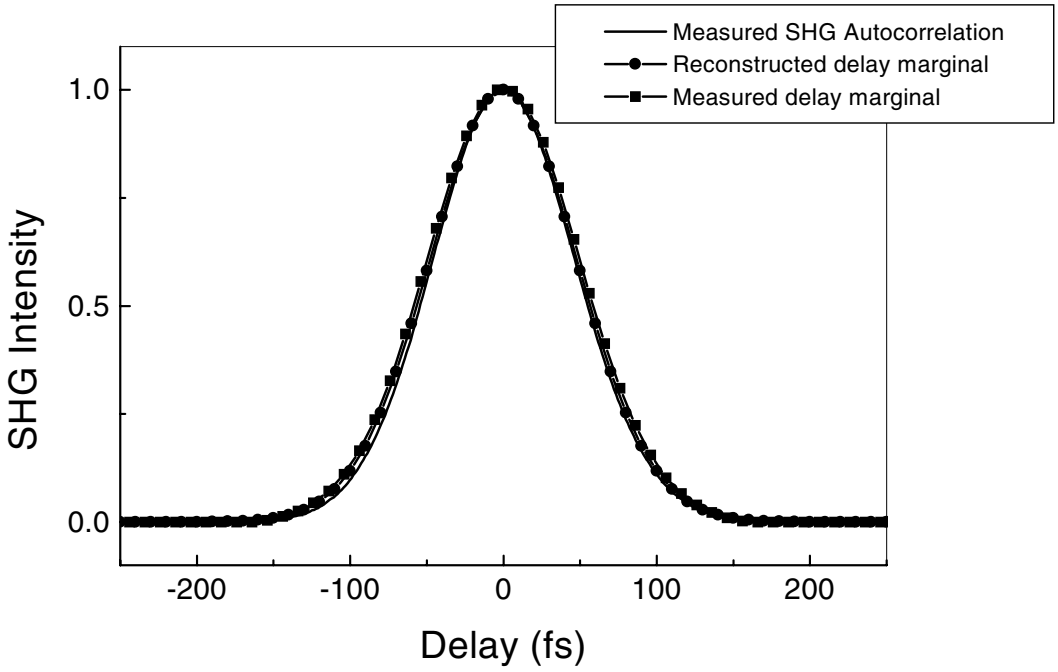

Figure 3.13: An example of the agreement between an independently measured autocorrelation of a pulse and the corresponding measured and reconstructed SHG FROG delay marginals.

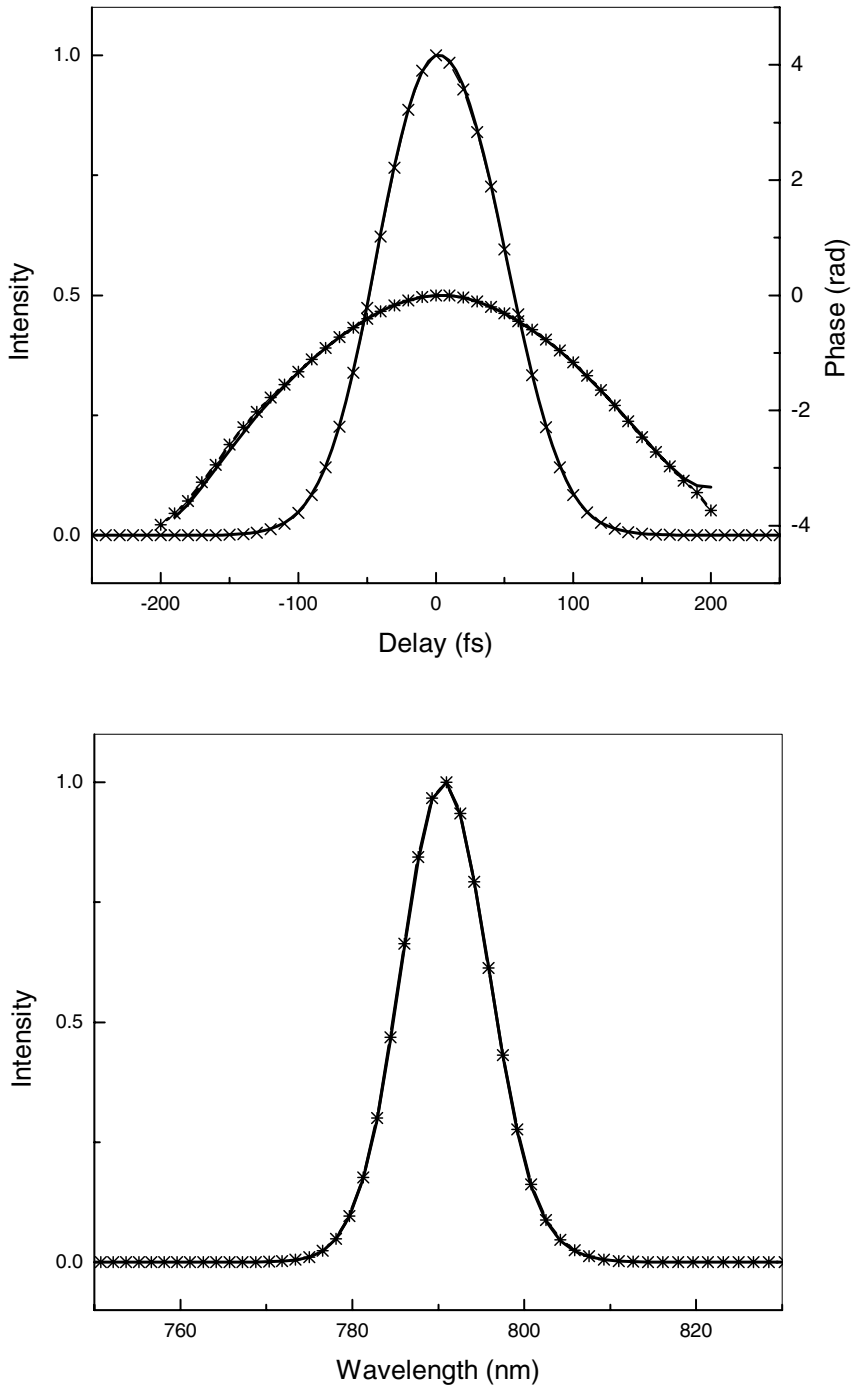

Figure 3.14: Retrieved intensity and phases (top) and retrieved spectra (bottom) of two SHG FROG measurements. The excellent agreement illustrates the repeatability of the SHG FROG technique.

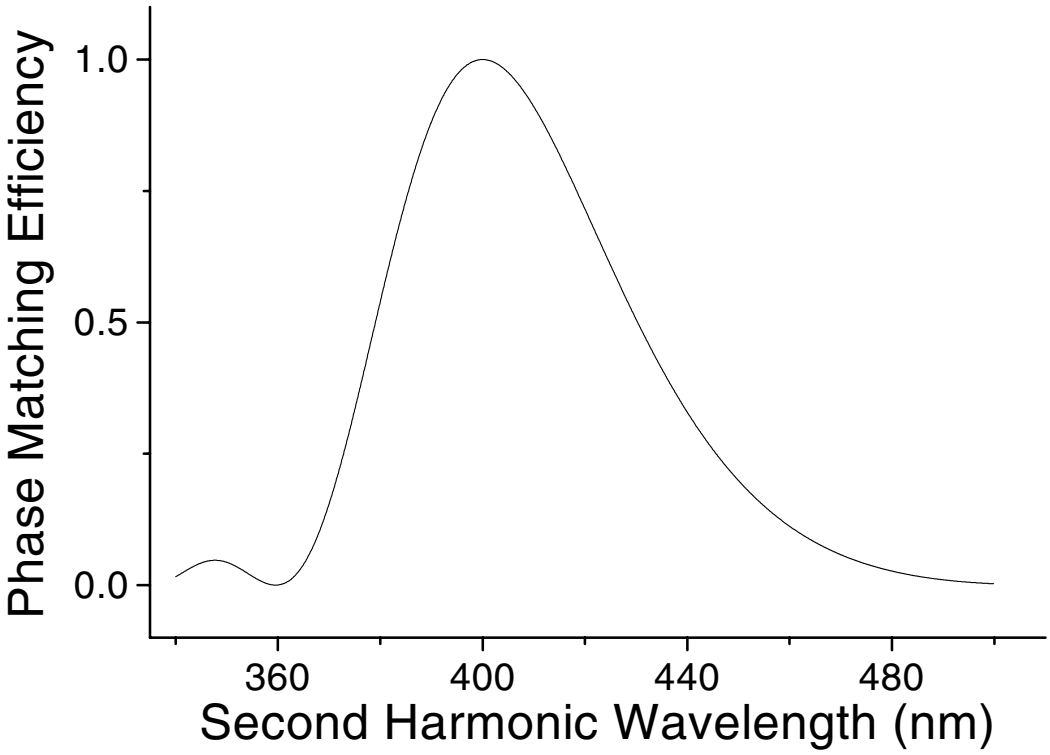

Figure 3.15: Phase matching efficiency curve for 50 μm BBO.

Measurement of more complicated pulses that result from highly nonlinear propagation is also accomplished well by SHG FROG. Gray scale intensity plots of the measured and retrieved FROG traces of a complicated pulse are shown in Fig. 3.16. The square root of the second harmonic intensity is shown for display purposes to emphasize the wings of each trace. Darker shading corresponds to higher intensity regions, and a contour plot with a contour interval of 40 units is overlaid on each trace. The actual intensity values (not the square root) range from 2 to $\sim 45,000$ counts. Very good agreement between the two traces is seen, even at the lowest intensity values. As discussed previously, the thin second harmonic crystal used in these experiments enables the full second harmonic spectrum of the pulse to be measured.

Figure 3.17 shows the spectrum recovered from the FROG algorithm (dashes) and an independently measured fundamental spectrum (solid line) corresponding to the data in Fig. 3.16. The spectra are plotted on a log scale to emphasize the very good agreement in the wings, down to the noise level of the spectrometer. The short wavelength side of the measured fundamental spectrum cuts off before the noise level is reached due to the spectrum extending beyond the edge of the CCD camera in the spectrometer. The excellent agreement between the two spectra demonstrates the high dynamic range capabilities of SHG FROG which make it suitable for characterizing the broad-bandwidth pulses that can result from nonlinear propagation.

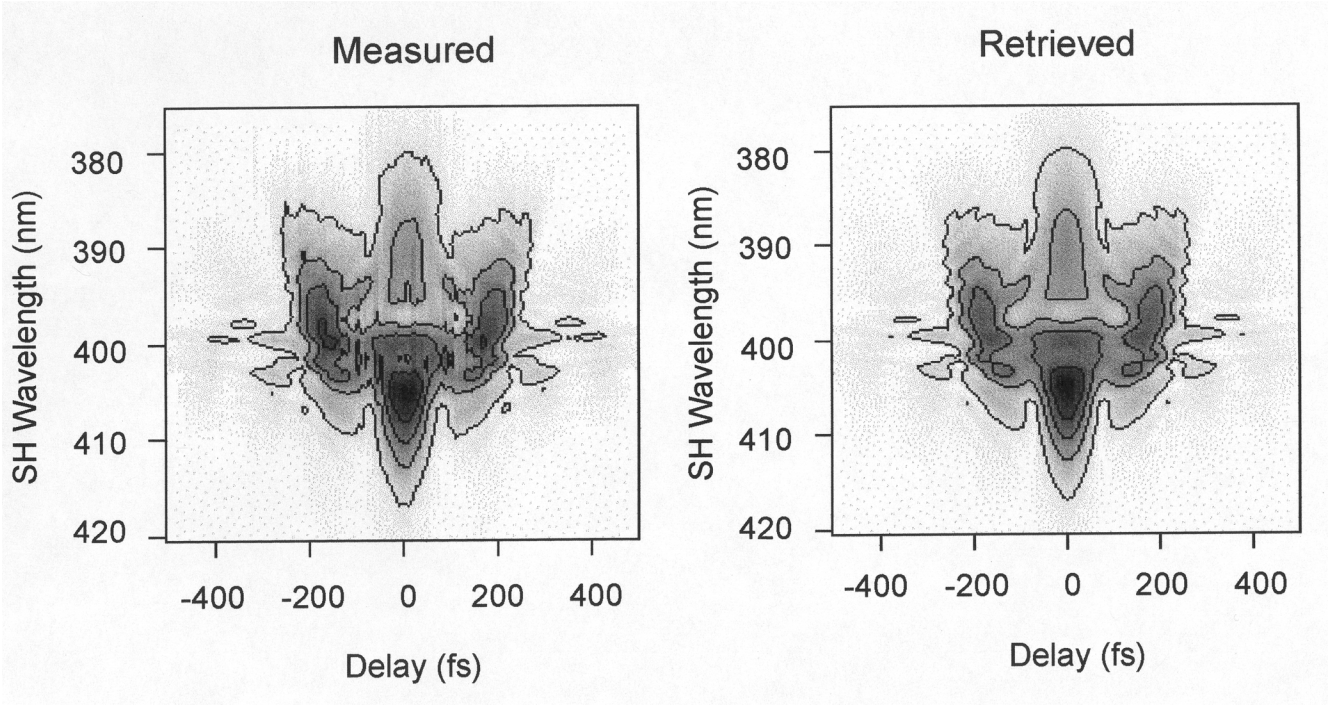

Figure 3.16: Measured and recovered SHG FROG traces, plotted as the square root of intensity, of a spectrally broad and temporally complicated pulse. Darker regions correspond to regions of higher intensity. The contour interval is 40 units.

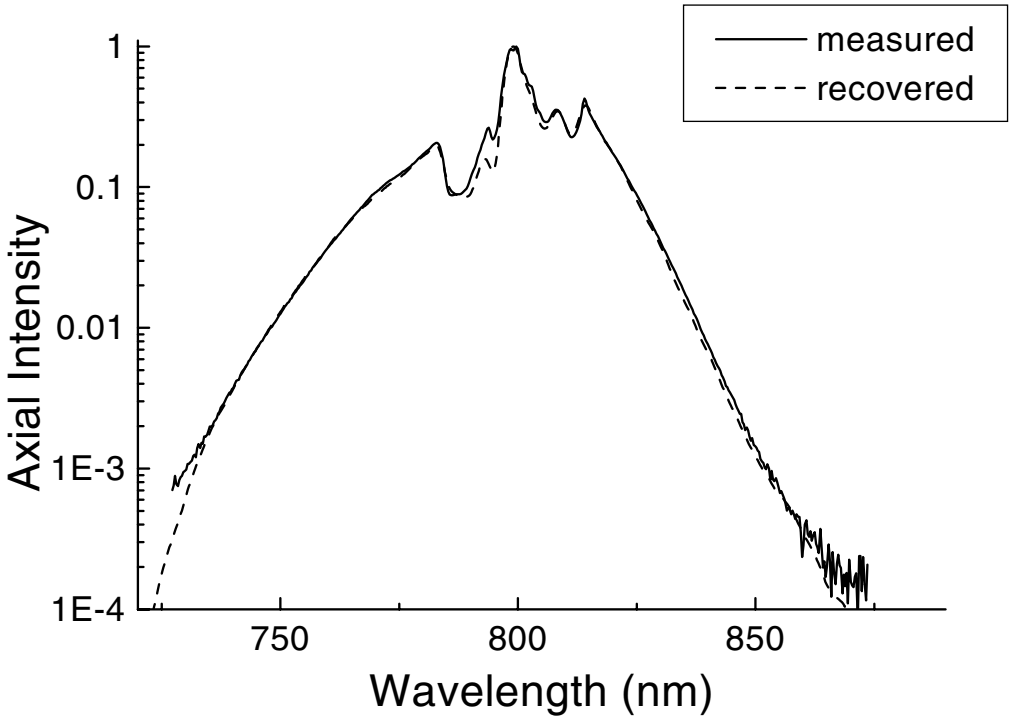

Figure 3.17: Independently measured (solid line) and recovered (dashed line) spectra corresponding to the FROG traces shown in Fig. 3.16. (From Ref. [89])

Chapter 4

Propagation in Fused Silica

Full-field measurements of femtosecond pulses provide valuable information in the study of ultrafast phenomena. For example, improvements in measurement techniques have contributed to a more comprehensive understanding of femtosecond lasers [4, 93, 77]. Femtosecond pulse diagnostics should not, however, be limited to the study and optimization of femtosecond sources. The study of light-matter interactions in general can benefit greatly from knowledge of the amplitude and phase of the electric field. Measurements of the nonlinear indices of refraction of materials [94, 82, 95] and the characterization of nonlinear propagation in optical fibers [96] demonstrate the utility of these full-field measurements. Such experiments not only elucidate light-matter interactions but can also serve to test the measurement technique itself.

In this chapter, we extend these full field measurements to the study of propagation of short pulses through fused silica. Section 4.1 presents early attempts to measure the nonlinear index of refraction of various materials using FROG. Difficulties in these measurements led to a study of one-dimensional (plane wave) propagation in fused silica (Section 4.2). These studies also serve to demonstrate the validity of FROG as a technique for investigating nonlinear pulse propagation. In Section 4.3, the experimental method is applied to the more complicated case of three-dimensional pulse propagation where nonlinear effects cause the pulse to change spatially as well as temporally during propagation. In this more complicated propagation regime, the combined effects

of group velocity dispersion and optical nonlinearities lead to the splitting of a pulse into two or more sub-pulses.

4.1 Measuring the Nonlinear Index of Refraction

The original goal of our investigations was to provide accurate measurements of the nonlinear index of refraction of various materials. The index of refraction of a given medium can be expressed as the sum of the linear index of refraction plus the nonlinear index of refraction times the intensity of the laser pulse and is typically written:

$$n = n_0 + n_2 I. \tag{4.1}$$

To measure the nonlinear index of refraction, one needs to measure the phase change acquired as a pulse traverses the material of interest. Assuming the change in phase of the pulse, $\Delta\Phi\left(t\right)$, is derived solely from self-phase modulation, $\Delta\Phi\left(t\right)$ is proportional to the change in index of refraction times the length of the medium. The change in index of refraction is simply $n_2 I$, and $\Delta\Phi(t)$ is given by

$$\Delta\Phi\left(t\right) = \frac{2\pi}{\lambda} n_2 I\left(t\right) L \tag{4.2}$$

where λ is the optical wavelength, and L is the length of the medium. Solving for n_2 yields

$$n_2 = \frac{\lambda}{2\pi L} \frac{\Delta\Phi\left(t\right)}{I\left(t\right)}. \tag{4.3}$$

The change in phase can be measured by making two separate measurements with FROG: one before (reference) and one after propagation through the sample. A simple subtraction of retrieved phase profiles yields $\Delta\Phi\left(t\right)$. Since the change in phase is assumed to be solely the result of self-phase modulation, $\Delta\Phi\left(t\right)$ should be proportional to the intensity profile, $I\left(t\right)$. It is common to separate the effects of GVD and SPM because GVD temporally rearranges frequencies within the pulse while SPM creates new frequencies. Contributions to the phase change from group velocity dispersion

can be calculated and added to the reference phase before subtraction of the two phase profiles. Some relevant equations are given later in this section. A fit of the measured intensity profile to the measured phase change gives a constant of proportionality, ζ, such that

$$n_2 = \frac{\lambda}{2\pi L}\frac{\zeta}{I_0} \tag{4.4}$$

where I_0 denotes the peak intensity of the pulse.

The peak intensity can be recovered from the FROG measurement, along with independent measurements of beam size and average power of the pulses. The measured average power divided by the repetition rate of the laser equals the energy per pulse. Energy per pulse is equivalent to the integral of the pulse intensity over space and time:

$$\text{Energy/pulse} = \int_0^\infty \int_0^{2\pi} \int_{-\infty}^{\infty} I\left(r,t\right) r \, dr \, d\phi \, dt. \tag{4.5}$$

If we assume a Gaussian spatial profile,

$$\text{Energy/pulse} = I_0 \frac{\pi\omega_0^2}{2} \int_{-\infty}^{\infty} I\left(t\right) dt. \tag{4.6}$$

The $1/e^2$ beam waist, ω_0, is determined from an intensity profile captured by a CCD camera. The integral $\int_{-\infty}^{\infty} I\left(t\right) dt$ can be obtained from a FROG measurement of the reference field thus allowing n_2 to be determined.

Measurements of this type are performed using the method presented by Taylor *et al.* [82]. The PG form of FROG is used for these initial measurements, with a 0.5 mm slit inserted before the cylindrical lens. This slit is centered on the beam and selects the most intense portion of the spatial profile. This aperture eliminates spatial averaging effects in the single-shot polarization gate geometry [82]. Measurements are performed with samples of fused silica of varying lengths. In order to induce phase changes of greater than 1 radian, sample lengths greater than 0.64 cm are used. After

propagation through the fused silica, the intensity profile is broadened significantly. Because of this broadening, a problem then arises in performing the fit between change in phase and the intensity profile. Using each of the two measured intensity profiles for performing the fit yields values of n_2 that differ by as much as 10%. Figure 4.1 shows a plot of intensity versus time for a pulse before and after propagation through a 2.54 cm sample of fused silica. The measured phase difference between the two pulses is also shown. Values of n_2 at 800 nm using the two intensity curves are 1.62×10^{-16} cm^2/W and 1.81×10^{-16} cm^2/W.

Pulse broadening due to GVD alone cannot account for such a large change. Assuming a Gaussian input pulse, the spectral field of the pulse is given by [97]

$$\mathcal{E}\left(\Omega, z\right) = A_0 \exp^{-x\Omega^2} \exp^{iy(z)\Omega^2} \tag{4.7}$$

where A_0 is a complex amplitude factor, Ω is frequency, and x and y are given by

$$x = \frac{T_G^2(0)}{4\left(1+a^2\right)} \quad \text{and} \quad y\left(z\right) = \frac{aT_G^2(0)}{4\left(1+a^2\right) - \frac{k''z}{2}}. \tag{4.8}$$

$T_G(0)$ represents the $1/e^2$ width of the input pulse in time, a is the input chirp parameter, and k'' — the second derivative of the wave vector k — determines the group velocity in the material. The $1/e^2$ width of a pulse broadened during propagation through a material of length z is then given by

$$T_G\left(z\right) = \sqrt{\frac{4}{x}\left[x^2 + y^2\left(z\right)\right]}. \tag{4.9}$$

For an unchirped input pulse, with $a = 0$, substituting Eq. 4.8 into Eq. 4.9 gives

$$T_G\left(z\right) = T_G\left(0\right)\left(1 + \left(\frac{z}{L_d}\right)^2\right)^{1/2} \tag{4.10}$$

where L_d is a characteristic length due to GVD and is given by

$$L_d = \frac{T_G\left(0\right)^2}{2|k''|}.$$

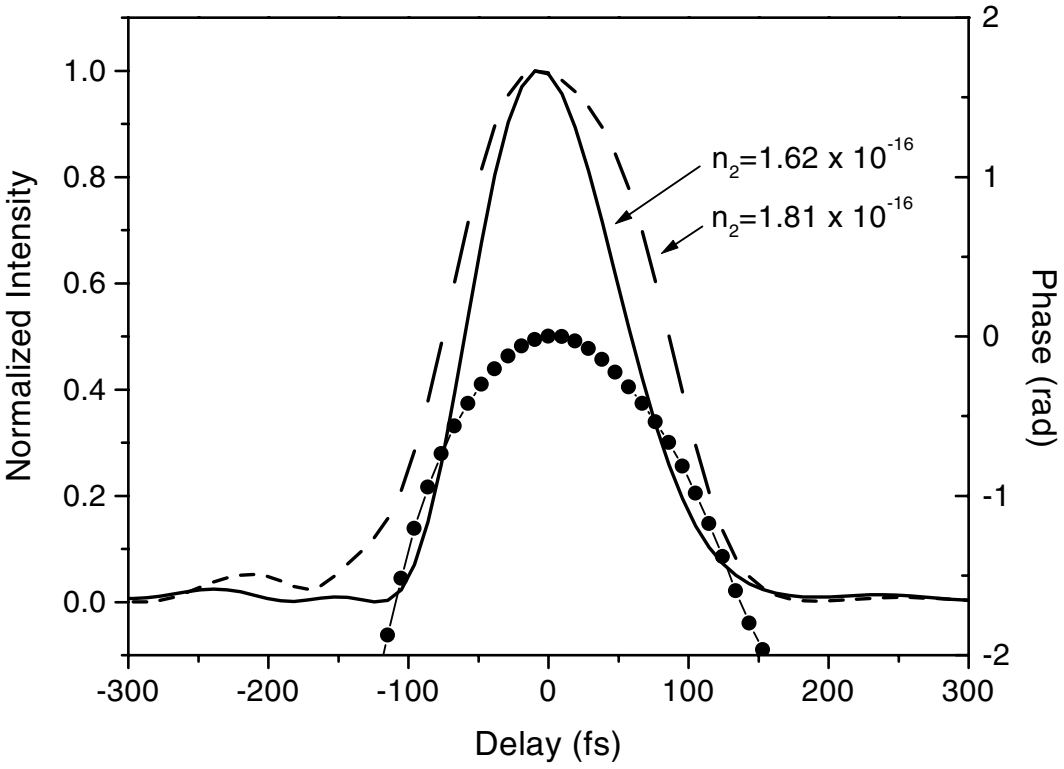

Figure 4.1: Retrieved intensity as a function of delay before (solid line) and after (dashed line) propagation through 2.54 cm of fused silica. Circles indicate phase difference. Calculated values of n_2 corresponding to each intensity profile are also shown.

A calculation of the expected pulse broadening due to GVD of a 92 fs pulse — a typical pulsewidth in our experiments — traversing 2.54 cm of fused silica reveals that the pulse should broaden by about $5\ \mathrm{fs}$. The observed broadening under the same conditions is on the order of $90\ \mathrm{fs}$. Clearly, then, the assumption that GVD and SPM can be treated separately works well only for short samples and longer pulses where broadening effects are minimized. It is only by looking at the combined effects of GVD and SPM on pulse propagation that such observations can be explained.

4.2 (1+1)-Dimensional Propagation

Fused silica is often used in applications involving short pulses in the visible and near infrared because it has low dispersion and is therefore presumed to contribute little to the broadening of femtosecond pulses. This may not be the case, however, when intensities greater than $\sim 1\ \mathrm{GW/cm^2}$ are present. At these intensities the nonlinear contribution to the index of refraction becomes important. Furthermore, the interplay between the nonlinearity and the linear dispersion can lead to surprisingly large changes in the pulse width over relatively small propagation lengths as seen in Fig. 4.1.

Neglecting changes in the transverse spatial profile, the propagation of a pulse in a nonlinear, dispersive medium can be modeled by the (1+1)-dimensional nonlinear Schrödinger equation (NLSE):

$$\frac{\partial \mathcal{E}}{\partial z} + i\frac{k''}{2}\frac{\partial^2 \mathcal{E}}{\partial t^2} - i\frac{2\pi n_2}{\lambda}|\mathcal{E}|^2\mathcal{E} = 0. \tag{4.11}$$

In this equation, $\mathcal{E}(z,t)$ is the slowly varying complex amplitude of the field in the rest frame moving at the group velocity. The GVD is determined by k'', which is the second derivative of the wave vector k with respect to frequency, evaluated at the center frequency. The third term gives the effects due to the instantaneous nonlinearity. The field is normalized such that $|\mathcal{E}|^2 = I$ is the intensity in units of W/cm^2.

Figure 4.2 shows the evolution of the on-axis temporal field of an intense pulse

as it propagates through fused silica. All fields are retrieved from SHG FROG measurements. In Fig. 4.2(a), the intensity and phase of the input pulse is plotted. Plots (b) and (c) of this figure show the intensity and phase of the same pulse after propagation through 1.27 cm and 2.54 cm of fused silica, respectively. In addition, plots (b) and (c) show the calculated intensity and phase using the measured field of Fig. 4.2(a) as an initial condition to Eq. 4.11.

As is illustrated in Fig. 4.2(b) and (c), good agreement exists between the measurement and the model. The peak intensity of the input pulse is $57\ \mathrm{GW/cm^2}$. In addition, $\lambda = 800\ \mathrm{nm}$ and $k'' = 360\ \mathrm{fs^2/cm}$ are used as parameters for the calculation. The value of n_2 can then be used as a fitting parameter. For these measurements, $n_2 = 2.5 \times 10^{-16}$ cm^2/W gives the best agreement between experiment and theory. This value of n_2 is in good agreement with other recent measurements [94, 82].

To lowest order, Eq. 4.11 includes the effects of group velocity dispersion and temporal self-phase modulation. During propagation at 800 nm, in the regime of positive GVD (k'') and positive n_2, both dispersion and temporal SPM will act to impose a predominantly positive chirp on the pulse. GVD then acts to broaden the chirped pulse. Similar results have been observed in optical fibers where the (1+1)-D NLSE, Eq. 4.11, also applies. The data in Fig. 4.2, however, provide the first amplitude and phase measurements detailing the interplay of positive GVD and SPM in bulk propagation.

The use of Eq. 4.11 to model the experimental conditions is justified as long as the field is well approximated by a plane wave during its propagation. For these experiments, a large diameter beam with confocal parameter $z_0 = \pi n_0 \omega_0^2/\lambda$ on the order of many tens of meters is used. The confocal parameter is defined as twice the Rayleigh range and the Rayleigh range is the distance a Gaussian beam propagates from the focal waist, ω_0, to the point where the diameter has increased by a factor of $\sqrt{2}$. In other words, the confocal parameter gives the full distance between positions where the spot size is $\sqrt{2}\omega_0$ in a focusing beam. Self-focusing due to the nonlin-

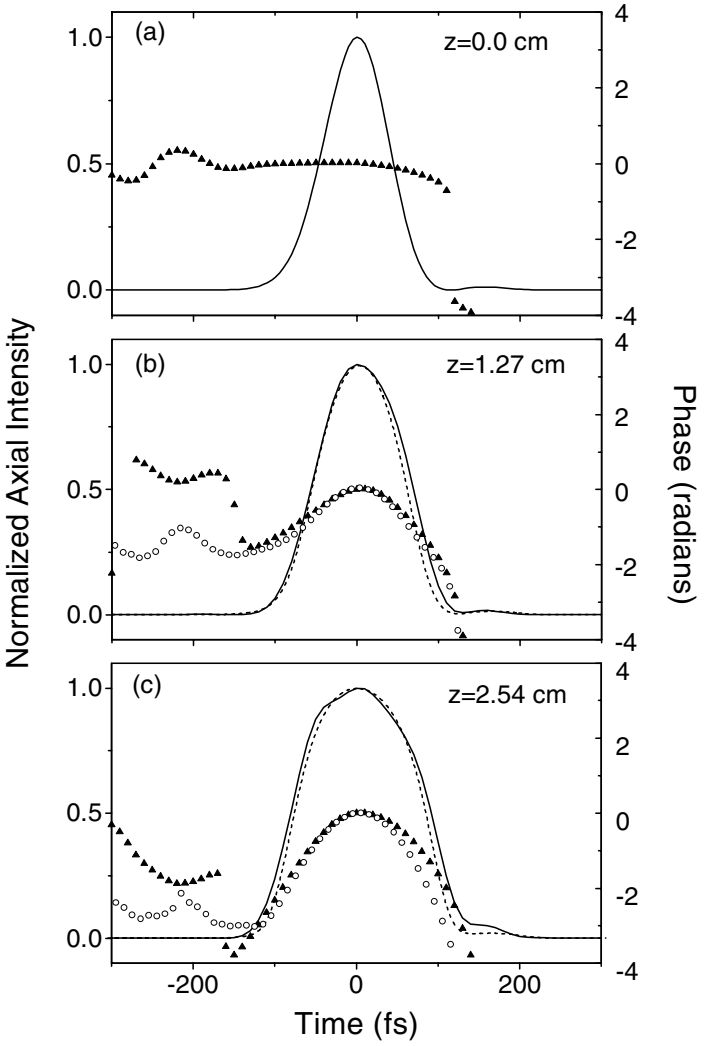

Figure 4.2: Temporal field of an intense femtosecond pulse at propagation distances in fused silica of z = 0, 1.27, and 2.54 cm. The experimentally measured intensity (solid lines) and phase (solid triangles) are shown in all three plots. The calculated intensity (dashed lines) and phase (open circles) are also shown in plots (b) and (c). (From Ref. [98]).

ear index of refraction can also affect the plane wave nature of the beam. The peak power of pulses used in these measurements is near $10\ \mathrm{GW}$. This power is many orders of magnitude above the critical power for self-focusing which is approximately given by $P_{crit} = (0.61\lambda)^2\pi/(8n_0n_2)$. In fused silica, at a wavelength of 800 nm, this expression evaluates to $P_{crit} = 2.6$ MW. The critical power for self-focusing is only defined for continuous wave propagation, and therefore the number given here is only a guideline. Even though the peak power is well above the critical power for self-focusing, the pulse propagates as a plane wave because the self-focusing length, defined as $z_f = \omega_0\sqrt{n_0/(n_2 I)}$, is on the order $50\ \mathrm{cm}$, which is more than twenty times greater than the propagation length. The validity of this plane wave approximation is further confirmed by comparing the results calculated by Eq. 4.11 with the results of a three-plus-one-dimensional [(3+1)-D] model presented later in this chapter. For the experimental conditions presented here, both the (1+1)-D and (3+1)-D models give nearly identical results.

The importance of the interplay between SPM and positive GVD is further illustrated in Fig. 4.3, where the full-width at half maximum (FWHM) of the measured and calculated intensities are plotted as a function of propagation length. In addition, the FWHM for the case of GVD alone is also plotted. As can be seen, inclusion of the nonlinearity results in dramatic pulse broadening over GVD alone. The fact that the calculated FWHM is slightly less than the measured value is still under investigation.

One possible explanation for this discrepancy was investigated. It is well known that the nonlinear susceptibility of fused silica is comprised of both a near-instantaneous electronic response and a slower nuclear response. The slower response, called the Raman response, is due to nuclear vibrations excited by the optically induced perturbation of the electronic structure. The characteristic Raman response time is on the order of $50 - 100\ \mathrm{fs}$ and can comprise up to 20% of the total nonlinear response [99, 100, 101]. We hypothesized that the Raman response of the fused silica could be responsible for

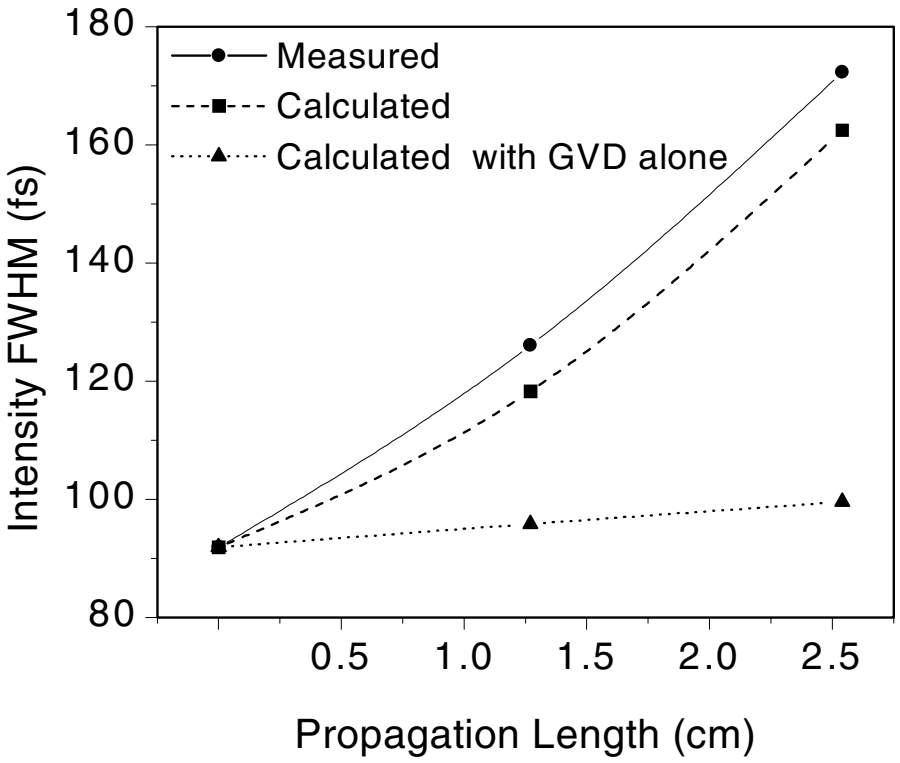

Figure 4.3: Measured and calculated FWHM of the intensities of the fields presented in Fig. 4.2. All calculations us the measured field of Fig. 4.2(a) as input. (From Ref. [98]).

the observed differences between the calculated and measured broadening. To test this, the Raman response was added into the model by replacing the nonlinear term of the (1+1)-D NLSE,

$$n_2 \left|\mathcal{E}(t)\right|^2$$

with

$$n_2 \left\{ (1-\alpha) \left|\mathcal{E}(t)\right|^2 + \alpha \int_{-\infty}^{t} f(t-t') \left|\mathcal{E}(t')\right|^2 dt' \right\}.$$

In this equation, α is the fraction of the nonlinearity resulting from the Raman contribution and $f(t-t')$ is the normalized Raman response function, which is approximated by [101]

$$f(t) = \frac{1+(\omega_r \tau_r)^2}{\omega_r \tau_r^2} \exp\left(-\frac{t}{\tau_r}\right) \sin(\omega_r t). \tag{4.12}$$

For the numerical simulations, α is varied, τ_r is the Raman response time taken to be 50 fs, and the dimensionless quantity $\omega_r \tau_r$ is taken to be 4.2. Calculations using this modified equation show that contributions from the Raman effect should not be observed in this regime. In fact, appreciable contributions from the Raman nonlinearity do not appear until peak intensities reach $100\ \mathrm{GW/cm^2}$ and higher. Peak intensities in these one-dimensional propagation experiments are an order of magnitude below that level. Other experiments, based on cross-correlations alone observe a similar discrepancy between measured and calculated broadening [102].

Despite the small discrepancy between calculated and measured broadening, agreement between the experiment and the model is quite good. These positive results give us confidence that the SHG-FROG technique can be successfully applied to the more complicated propagation measurements presented in later sections of this chapter.

4.3 (3+1)-Dimensional Propagation

As shown in the previous section, plane-wave propagation in the regime of positive GVD and positive n_2 leads to a lengthening of the pulse in time due to the combination of dispersion and SPM continuously separating the component wavelengths of the pulse. The addition of transverse dimensions to the problem, however, can result in interesting and complicated spatio-temporal effects, including temporal pulse splitting [103, 104, 105, 106]. We emphasize this in contrast to the (1+1)-D situation presented in the previous section and in contrast to nonlinear propagation in single-mode optical fibers where pulse splitting is not observed due to the spatial constraints of the field [107]. For Gaussian input pulses, the (1+1)-D NLSE does not predict pulse splitting even with higher intensities and greater propagation distances. Temporal pulse splitting during nonlinear propagation in bulk media has been verified experimentally by spectral [108, 41] and autocorrelation measurements [42, 109]. These measurements, however, lack full information about the amplitude and phase of the field. In order to provide a more complete picture of the complicated dynamics involved in the pulse splitting process, we use SHG-FROG to measure the complete on-axis temporal field of a pulse after propagation in a self-focusing regime. These experiments allow us to make detailed comparisons with theoretical models and gain a better understanding of the processes involved in the propagation.

For the following measurements, the output from the laser system is spatially filtered, strongly attenuated, and focused with a $50\ \mathrm{cm}$ focal length lens to a spot size of $70\ \mu\mathrm{m}$ FWHM at the entrance face of a 2.54 cm long fused silica sample. After propagation, the pulse is allowed to diverge for $\sim 75\ \mathrm{cm}$. The central portion of the beam is then selected with an aperture and used as input to the SHG-FROG. In contrast to the (1+1)-D experiments mentioned in the previous section, the peak power of the pulses used in these experiments is much lower. Typically, the peak power is only one

to three times the critical power for self-focusing. Both the self-focusing length and the confocal parameter are on the order of the propagation length, however, meaning that transverse changes in the beam may no longer be neglected.

4.3.1 Experimental Results at 800 nm

Figure 4.4 shows the results of successive SHG FROG measurements for increasing input powers. The intensity and the phase in the time domain are shown in the left column. Independently measured spectra and the spectra recovered from the SHG FROG measurements serve as a check of FROG convergence and are shown in the right column. The top row of Fig. 4.4 is the input field, with a temporal intensity FWHM of 92 fs. The time-bandwidth product is 0.6, and some uncompensated second- and third-order phase variations are evident. Moving down the rows of Fig. 4.4, the pulse undergoes a partial splitting, a full splitting, and then multiple splittings. The fully split pulses of Figs. 4.4(c) and (d) are nearly two times shorter than the input pulse, having durations on the order of 50 fs. With the instantaneous frequency defined as $\omega_{inst} = \omega_0 - d\phi/dt$, the predominant negative curvature of the temporal phase implies upchirped pulses. The calculated critical power for self-focusing in fused silica is $P_{crit} = 2.6$ MW for values of $n_0 = 1.45$, $n_2 = 2.5\times10^{16}$ cm^2/W, and $\lambda_0 = 800$ nm. The measured peak powers for Fig. 4.4(b), (c), and (d), are 1.7 P_{crit}, 1.9 P_{crit}, and 2.3 P_{crit}, respectively. The associated spectra for the split pulses show pronounced broadening and modulation, with the characteristic modulation frequency being equal to the inverse of the time spacing between the pulses. Agreement between the measured and the recovered spectra is considered very good in view of the complicated structure. Experiments were performed which show that increasing the length of the sample has the same qualitative effect as increasing the peak input intensity.

From a simple physical standpoint, the basic process of pulse splitting can be understood as follows. Initially, strong self-focusing moves off-axis energy toward

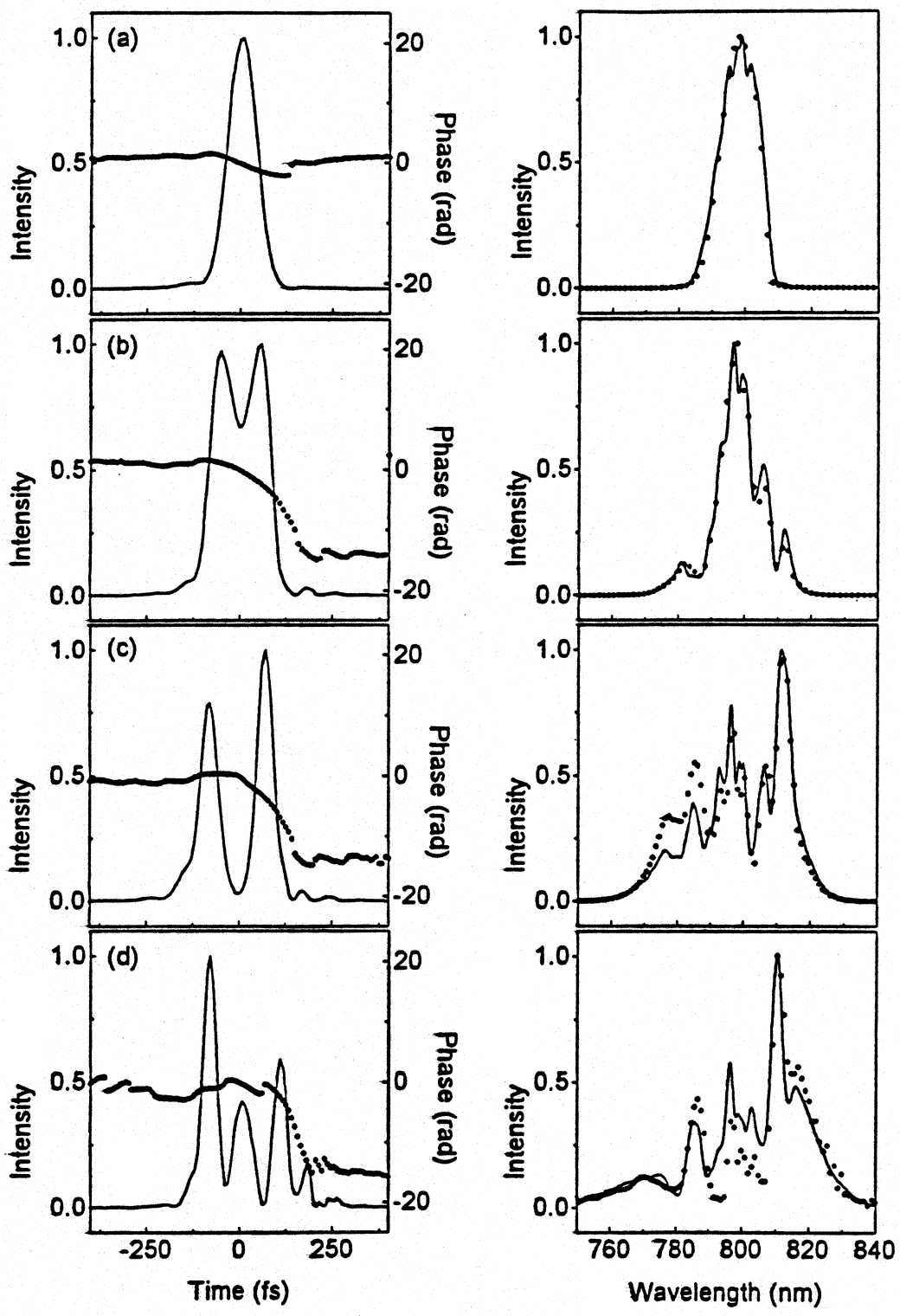

Figure 4.4: Left column: Measured temporal intensity (lines) and phase (points) of the input pulse (a) and the pulse after propagation through 2.54 cm of fused silica (b)–(d). Plots (b)–(d) correspond to a peak input power of 1.7 P_{crit}, 1.9 P_{crit}, and 2.3 P_{crit}, respectively. Right column: The corresponding independently measured (lines) and retrieved (points) spectra. (From Ref. [91])

the peak of the pulse and compresses it in both space and time [110]. As the peak intensity increases, effects due to SPM also increase, thereby generating new frequency components. The combination of the SPM-induced upchirp and positive GVD then act to push the energy away from the temporal center of the pulse, initiating pulse splitting. As this process continues, the peak intensity drops, stopping the collapse at the temporal pulse center. Off-axis energy, however, continues to focus away from the temporal center such that two pulses are resolved [105].

Variations in the phase of the input pulse can strongly affect the output. It is possible to create a predominantly linearly chirped input pulse by lengthening or shortening the grating compressor of the chirped pulse amplification system. Experiments were performed using both upchirped and downchirped input pulses. The sample is a 2.54 cm long piece of fused silica. The upchirped pulse for these measurements has a temporal FWHM of 147 fs, and the downchirped pulse has a temporal FWHM of 153 fs. The time-bandwidth product of the input pulse in both cases is ~ 0.8. Each of the chirped input pulses propagates through the fused silica sample at two different peak intensities. The lower peak intensity values are 45 and 49 $\mathrm{GW/cm^2}$ for the upchirped and downchirped pulses, respectively. The higher input peak intensity is 57 $\mathrm{GW/cm^2}$ for both upchirped and downchirped pulses.

Figure 4.5 shows the measured SHG FROG traces obtained with chirped input pulses in each of the higher power cases. In addition, both the retrieved and independently measured spectra are plotted for comparison. The characteristic shape of the SHG FROG trace for pulse splitting with a downchirped pulse [Fig. 4.5(a)] is very different than when the input pulse is upchirped [Fig. 4.5(c)]. An upchirped input pulse leads to SHG FROG traces after propagation which are largely diamond shaped, with decreasing intensity in the center of the trace, implying greater splitting. The downchirped input pulse, on the other hand, maintains a significant intensity in the center of the trace. Figure 4.6 shows the retrieved time and spectral domain intensity

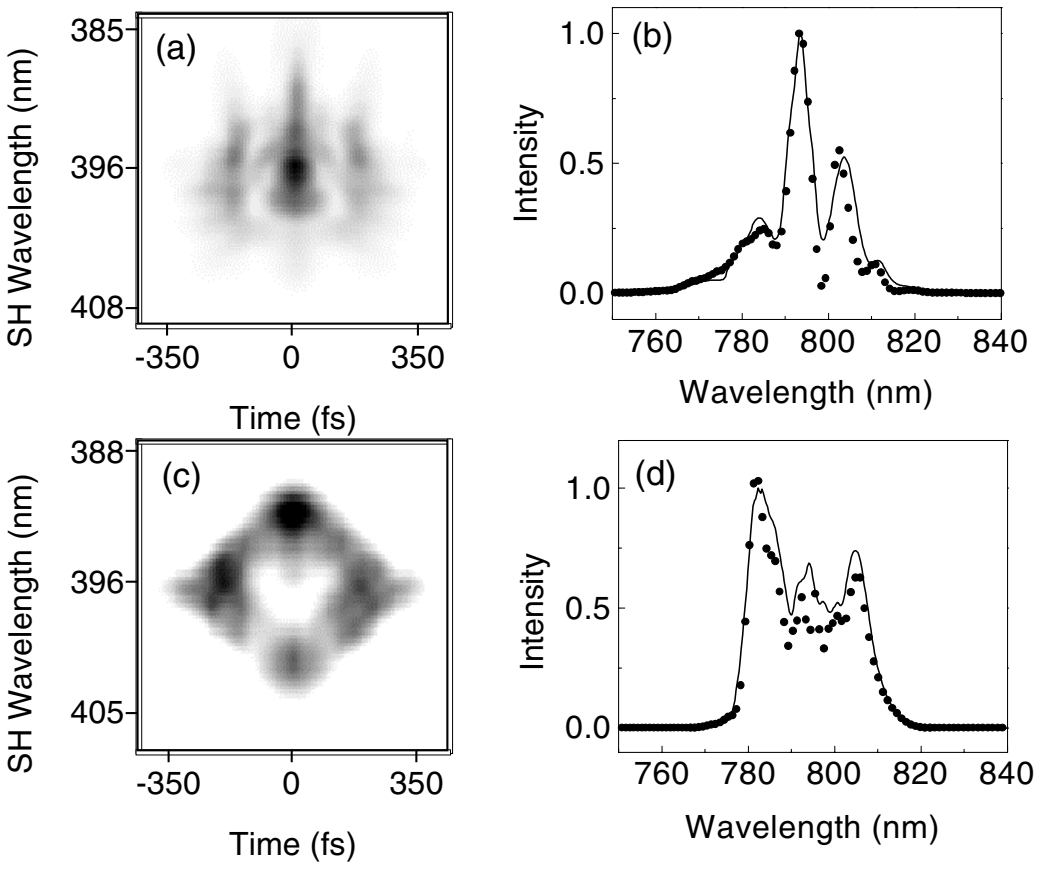

Figure 4.5: Left column: Measured SHG FROG traces after propagation with (a) downchirped and (b) upchirped input pulses. Right column: Corresponding independently measured (lines) and retrieved (points) spectra. The peak intensity is 57 GW/cm^2 in each case. (From Ref. [98])

and phase for each of the four input pulse cases. At higher peak powers, the amount of pulse splitting and spectral modulation increases. When an initially downchirped pulse [Figs. 4.6(a) and (b)] splits temporally, the resulting pulses are about two times narrower than those produced from the splitting of an upchirped pulse [Figs. 4.6(c) and (d)]. In addition, the spectra in Figs. 4.6(e) and (f) (downchirped input) are narrower than the spectra of Figs. 4.6(g) and (h) (upchirped input). A simple explanation for these observations arises from the fact that both positive GVD and SPM (from positive n_2) act to produce positive, linear chirp over the central region of the pulse. Thus, an initial upchirp on the pulse acts as a head start to the propagation induced upchirp, resulting in broader pulses. On the other hand, an initial downchirp, acts to negate the propagation induced upchirp, yielding shorter split pulses at the output. The narrower and deeply modulated spectrum seen with the downchirped input can be interpreted as destructive interference between existing frequencies and new frequencies created by SPM. Note also that the spectral phase after propagation for all four cases has an overall concave-up curvature, regardless of the sign of the chirp of the input pulse. This phase curvature implies an upchirp across the total split field such that the leading pulse is spectrally red-shifted compared to the trailing pulse. This upchirp is due to the combined effects of positive GVD and self-phase modulation in the regime of positive n_2, as discussed in the (1+1)-D case.

4.3.2 Experimental Results at 1200 nm

Measurements were also performed using the output of a femtosecond optical parametric amplifier (OPA). When pumped at 800 nm, the OPA produces signal fields with wavelengths in the range of 1100-1400 nm. This is an interesting regime in which to study propagation because these wavelengths are predominantly used for optical communications in fused silica fibers. In addition, in this wavelength range, the GVD in fused silica decreases in magnitude and then changes sign from positive to negative

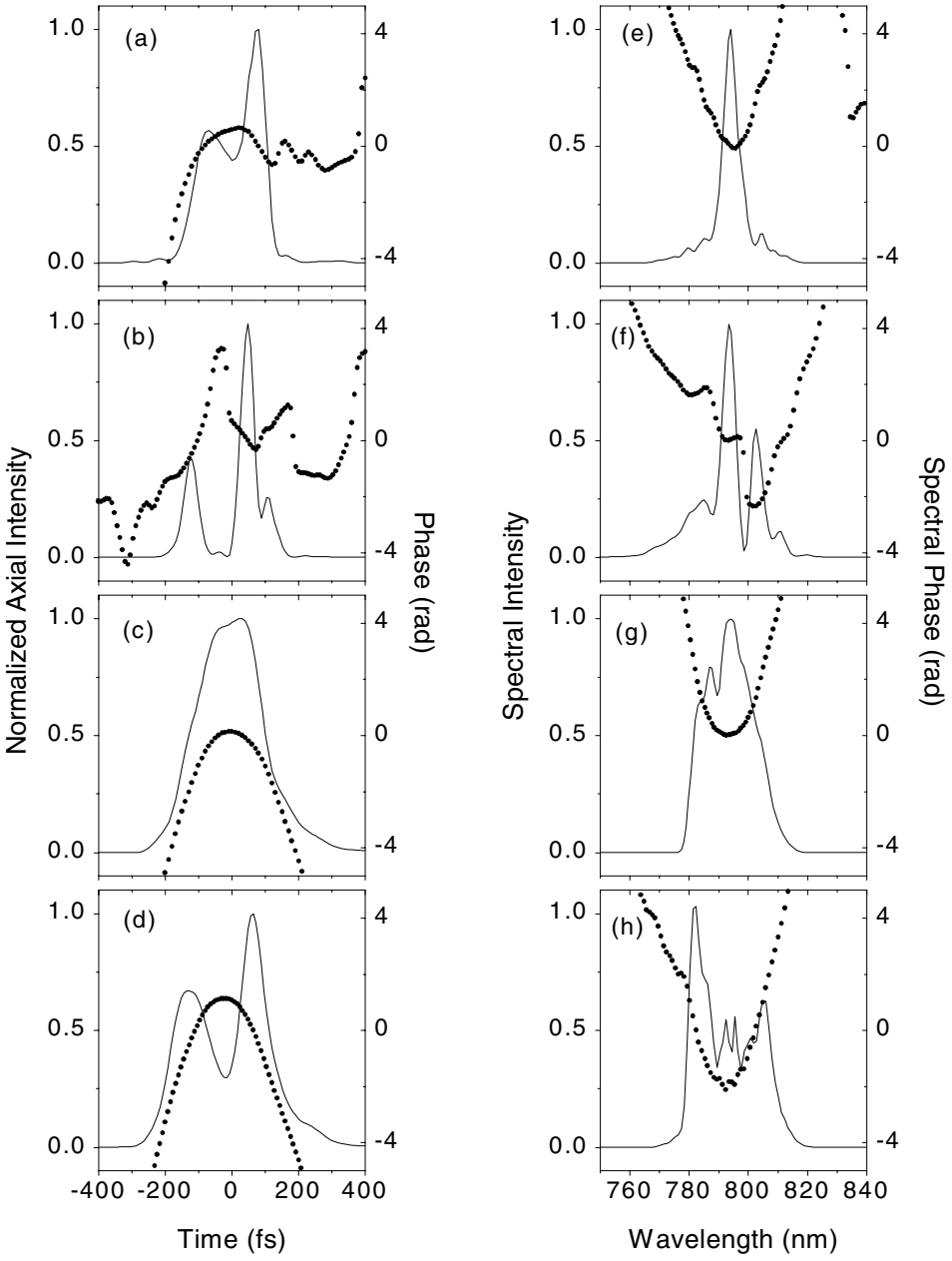

Figure 4.6: Retrieved fields from SHG FROG: (a)–(d) temporal intensity (lines) and phase (points); (e)–(h) associated spectral intensity (lines) and phase (points). Plots (a) and (b) correspond to downchirped input pulses at 49 and 57 GW/cm^2, respectively; (c) and (d), to upchirped input pulses at 45 and 57 GW/cm^2, respectively. (From Ref. [98])

near 1250 nm, while n_2 remains approximately constant. With negative GVD (anomalous dispersion) and positive n_2, it has been predicted that spatio-temporal solitons can propagate [111]. From a practical point of view, such 3-D solitons could have important implications for optical communications and all-optical switching [112, 113].

To insure good beam quality, the output of the OPA is spatially filtered and recollimated before being focused onto the entrance face of the fused silica sample in the same manner described for the $800\ \mathrm{nm}$ experiments. Beam parameters are approximately the same as those used at 800 nm, so that qualitative comparisons can be made between the two situations. Results at the wavelength of 1200 nm are shown in Fig. 4.7. In this figure, the temporal intensity and phase before and after propagation through 3.0 cm of fused silica sample are shown. The corresponding spectra recovered from SHG FROG and the independently measured spectra are also shown. Here again, very good agreement between the recovered and measured spectra is demonstrated. The input field of Fig. 4.7(a) has a FWHM duration of 92 fs, but the large negative curvature of the phase indicates the existence of significant linear upchirp. The time-bandwidth product is three times the transform limit which implies that 30 fs pulses could be generated if the upchirp were properly compensated. After propagation through the fused silica, the pulse begins to split, as can be seen in Figure 4.7(c). The input peak power in this case is $9\ \mathrm{MW}$, and assuming the value of n_2 is the same at both 800 and 1200 nm, this equals 1.5 P_{crit}. With a 10% increase in the power above $9\ \mathrm{MW}$, rapid spectral broadening and continuum generation are observed. The splitting observed in Fig. 4.7(c) is comparable to the splitting observed with an upchirped input pulse at 1.2 P_{crit} at 800 nm. The splitting at 1200 nm, however, is more symmetric. One would expect the splitting to be less pronounced at 1200 nm because of the decrease in the GVD at these wavelengths. The amount of splitting observed here is thus surprising.

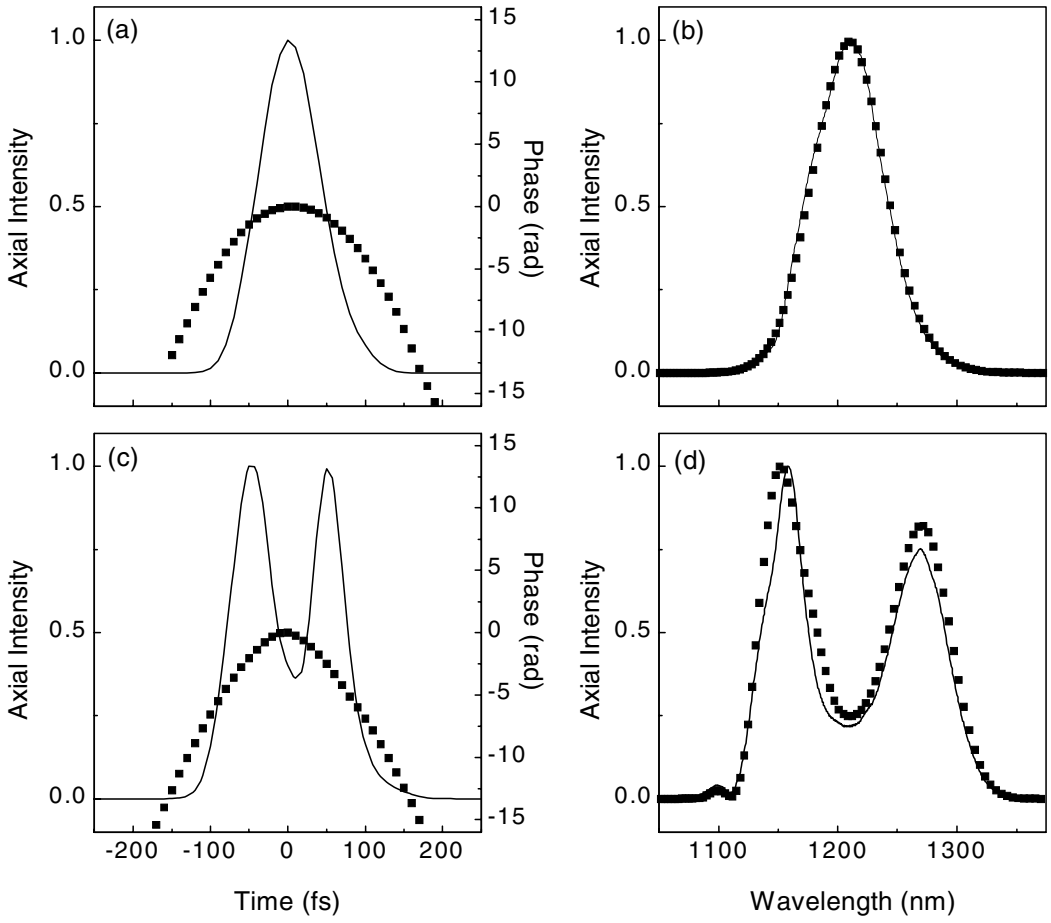

Figure 4.7: Measured fields at 1200 nm. (a) Intensity (line) and phase (points) of the input field, and (b) the corresponding independently measured spectrum (line) and the spectrum retrieved from SHG FROG (points). Plots (c) and (d) show the same pulse after propagation through 3.0 cm of fused silica. (From Ref. [98])

4.3.3 Theory

As opposed to our plane-wave experiments, to model the pulse-splitting experiments presented here, it is necessary to take into account the spatial dimension of the beam. If azimuthal symmetry is assumed, the transverse dimension can be added to the nonlinear Schrödinger equation in the following manner:

$$\frac{\partial \mathcal{E}}{\partial z} - \frac{i}{2k_0}\Delta_\perp^2 \mathcal{E} + \frac{ik_0''}{2}\frac{\partial^2 \mathcal{E}}{\partial t^2} - i\frac{k_0 n_2}{n_0}\left|\mathcal{E}\right|^2 \mathcal{E} = 0. \tag{4.13}$$

The only differences between this equation and Eq. 4.11 are the addition of the radial Laplacian $\Delta_\perp^2$ and the additional radial dependence of the field, $\mathcal{E}\left(z, r, t\right)$. The wave vector is $k = 2\pi n_0/\lambda$, with n_0 being the linear index of refraction at the center wavelength. Again, the field is normalized such that $\left|\mathcal{E}\right|^2 = I$ is the intensity in units of $\mathrm{W/cm^2}$. Equation 4.13 is referred to as the (3+1)-D nonlinear Schrödinger equation (NLSE), and takes into account diffraction, linear dispersion, spatial self-focusing, and temporal self-phase modulation. It has been predicted that self-focusing could eventually lead to catastrophic collapse of the pulse as focusing increases the peak intensity, which in turn increases the focusing effect [114]. The (3+1)-D NLSE has been used, however, to show that below a certain power threshold GVD is sufficient to stop this collapse and temporal pulse splitting results [115]. Numerical solutions of Eq. 4.13 are performed using the Crank-Nicholson method to compute the derivatives. For all simulations, the real input field is assumed to have a Gaussian spatial profile and either a Gaussian or hyperbolic secant squared temporal profile. Both temporal profiles have been found to yield similar numerical results, and the initial temporal profile is chosen that most closely resembles the experimental input pulse for each set of conditions. All parameters used, such as temporal and spatial beam size and initial peak intensity, are taken from experiment. The value of n_2 is again taken to be $2.5 \times 10^{-16}\ \mathrm{cm^2/W}$.

Figure 4.8 shows the results of numerical simulations of propagation of a Gaussian input pulse through $3.0\ \mathrm{cm}$ of fused silica. At the lowest input power, $P_{peak} = 0.2\, P_{crit}$,

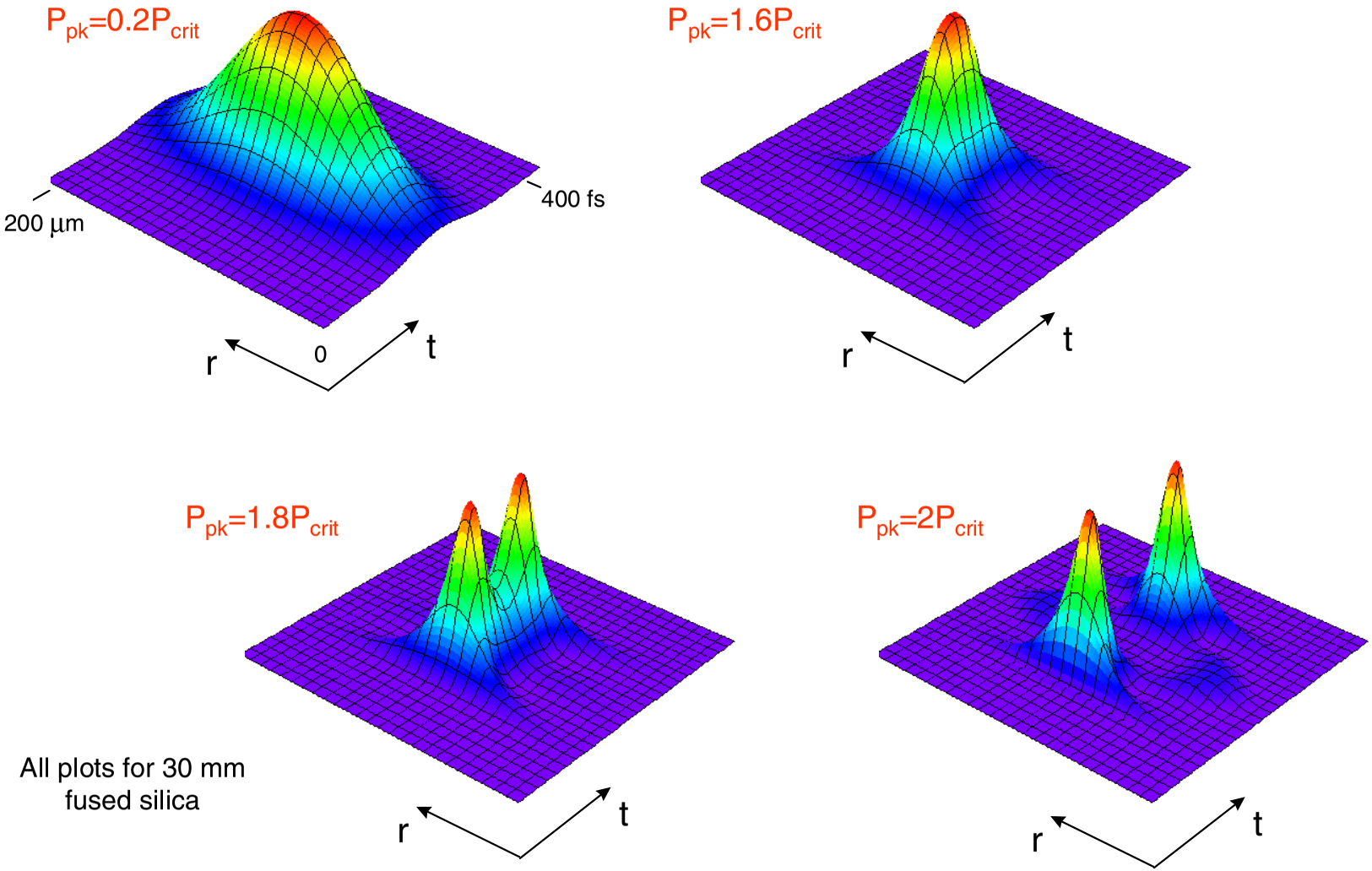

Figure 4.8: Calculated (using Eq. 4.13) intensity surface plots for a Gaussian input pulse after propagation through 3.0 cm offused silica.

the pulse has remained mostly Gaussian, with essentially only the effects of GVD and SPM coming into play. When the input peak power is increased to 1.6 P_{crit}, self-focusing has significantly compressed the pulse in space, and the pulse is also compressed in time. This pulse sharpening effect was predicted and measured more than 30 years ago [110, 116]. Put simply, this pulse sharpening effect is the result of the self-focusing induced transfer of off-axis energy toward the peak of the pulse. At the same time, SPM has created many new frequencies within the pulse. At a peak power of 1.8 P_{crit}, GVD has begun to spread the component frequencies in time, initiating pulse splitting. At this point, the peak intensity of the pulse has dropped. With a peak power of 2.0 P_{crit}, the pulse completely splits in time and two sub-pulses are resolved, each of which are narrower in time than the original pulse.

The theory predicts a pulse splitting that is symmetric in intensity. The experiment, however, reveals asymmetric pulse splitting. Figure 4.9 shows a comparison of the model with experiment at two different input peak powers. At the higher input power, the experiment shows split pulses with the trailing pulse larger than the leading pulse. There is also a corresponding rapid change in the phase at the trailing edge of the pulse. These two observations are consistent with the formation of a shock front. The increased intensity at the peak of the pulse leads to a higher index of refraction for those pulse components. The center of the pulse experiences a larger group delay than the wings of the pulse, resulting in a piling up of energy at the trailing edge of the pulse. Space-time focusing is believed to contribute to the observed asymmetry [105]. Cubic phase variations on the initial field are expected to play a lesser role [117]. Unlike the (1+1)-D case, peak intensities in this self-focusing regime reach high enough levels that the Raman response of fused silica is likely to become important during the propagation. The peak intensity of the self-focused field approaches the $\mathrm{TW/cm^2}$ level, however, no intensity-dependent loss indicative of multi-photon ionization or absorption is observed. Furthermore, no visible signs of permanent damage are observed

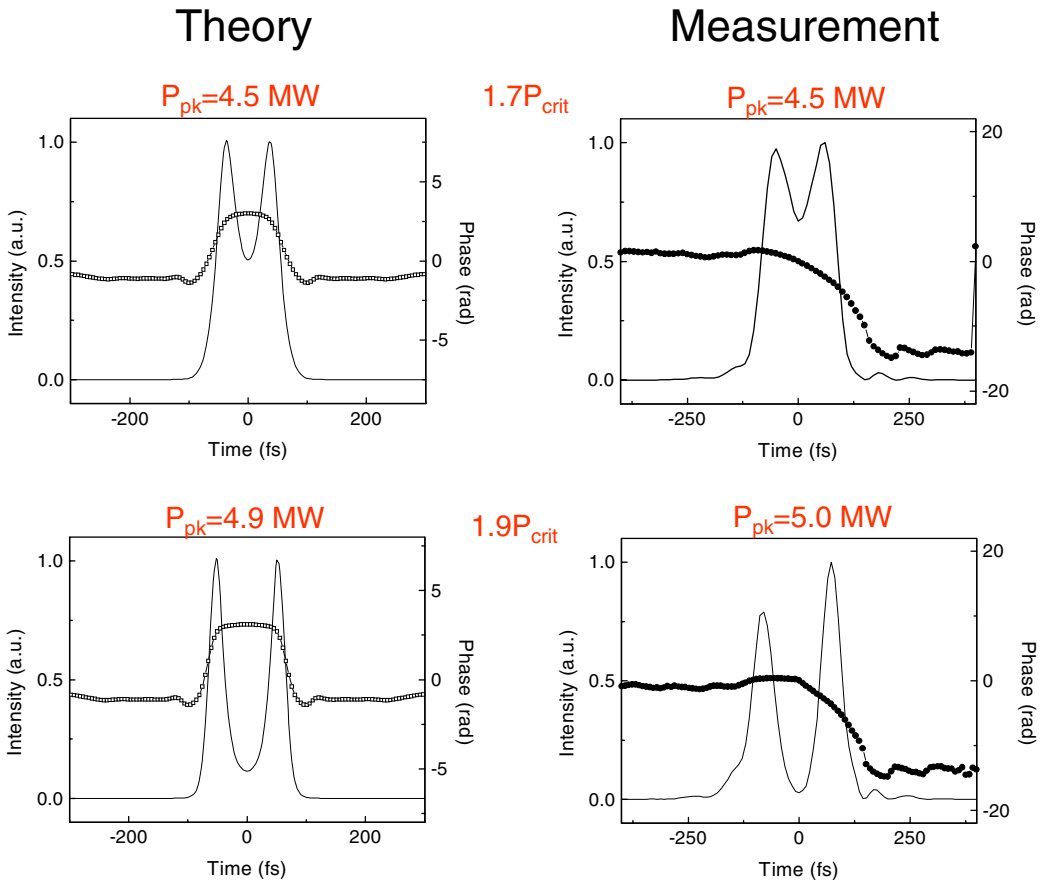

Figure 4.9: Calculated (using Eq. 4.13) and measured fields after propagation through 3.0 cm of fused silica. For all plots, lines represent intensity; and points, phase. Theory predicts symmetric pulse splitting while the experiment observes asymmetric splitting.

in the fused silica.

Measurements illustrating changes in the spatial profile of the beam, along with the calculated beam diameter, are shown in Fig. 4.10. Here, the measured beam diameters (FWHM) at the exit face of a 3.0 cm fused silica sample for four different input powers are presented. SHG FROG measurements of the temporal field are also made at these same input powers, allowing the degree of temporal splitting to be monitored. The time domain results are similar to those presented in Fig. 4.4. The beam diameters shown in Fig. 4.10 are obtained by imaging the exit face of the fused silica sample onto a CCD camera with a magnification of +2.8. The FWHM of intensity is measured along x and y dimensions. The calculated beam diameters are obtained by integrating over the temporal dimension of intensity plots similar to those presented in Fig. 4.8. The two points at the lowest powers correspond to pulses that have broadened temporally, but have not yet split. At the third point, the pulse is partially split, such that the intensity between the two pulses drops to half the peak value. At the highest peak power, the pulse is completely split – similar to Fig. 4.4(c). Both the numerical and experimental results demonstrate that the spot size approaches a constant value at powers where pulse splitting occurs. The measurements indicate that this regime occurs at lower powers than predicted by the theory. Although, as seen in Fig. 4.10, the error in the measured power is on the order of 25% due to uncertainties in the measured pulse energy and the temporal profile of the pulse. In addition, the measured spot size is never as small as the calculated value. This discrepancy may arise from spatial profile deviations of the actual beam from an ideal Gaussian.

The simple (3+1)-D NLSE fares even less well in comparison to the experiments at 1200 nm. Because of the decreased amount of linear dispersion in this regime, one would expect decreased pulse splitting activity. In fact, using Eq. 4.13 with a value of $k'' = 60$ fs^2/cm at 1200 nm, no splitting is predicted even for higher input powers. These results, together with recent simulations by Trippenbach *et al.*, indicate that third-

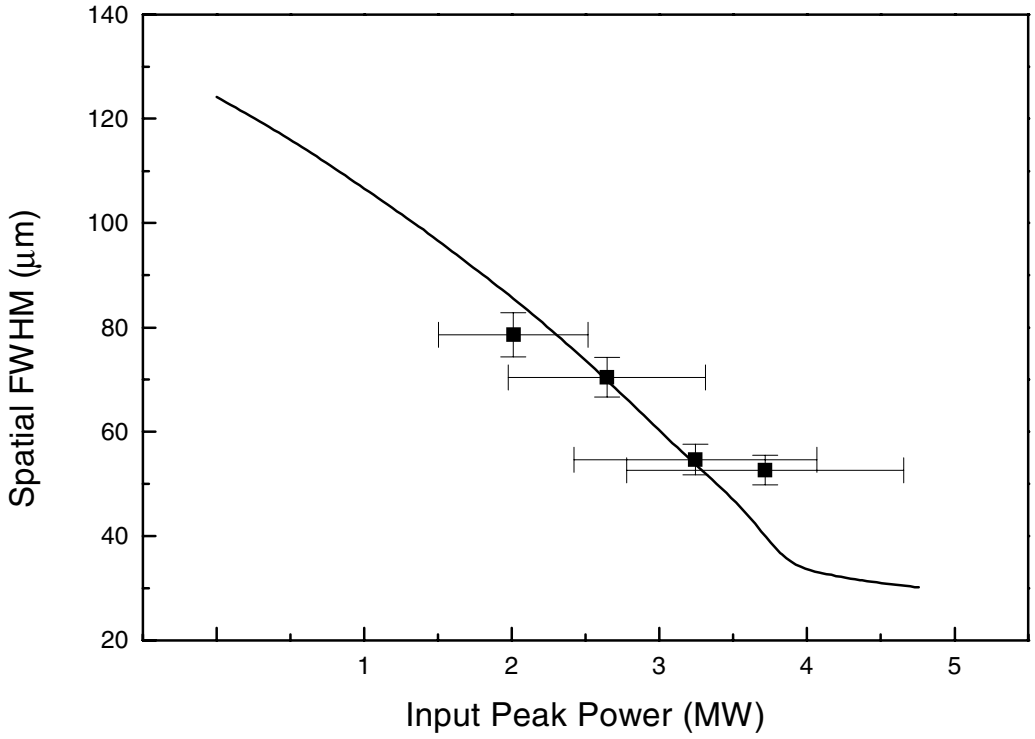

Figure 4.10: Measured spatial FWHM of beam size as a function of input peak power (points). The solid curve is the calculated beam size assuming a Gaussian spatial pulse for the input beam. (From Ref. [98])

order dispersion plays an important role in pulse splitting in this regime [118].

The differences in the experimental and calculated results point out that it is necessary to modify the (3+1)-D NLSE to include additional terms. From comparisons with the experiment at 800 nm, we find it necessary to include terms for space-time focusing, nonlinear shock, and a Raman response of the fused silica. Comparisons with experiments at 1200 nm indicate the need for inclusion of third-order dispersion. In addition, self-focusing can result in spot sizes in the sample that are on the order of or less than a few wavelengths of the light, invalidating the paraxial approximation. For this reason, we also include a term for nonparaxiality. These terms are included by modifying the (3+1)-dimensional NLSE as follows:

$$\frac{i}{2k}\nabla_{\perp}^{2}\mathcal{E} - \frac{ik'}{k}\frac{\partial^{2}\mathcal{E}}{\partial z\partial t} + \frac{i}{2k}\frac{\partial^{2}\mathcal{E}}{\partial z^{2}} - \frac{ik''}{2}\frac{\partial^{2}\mathcal{E}}{\partial t^{2}} + \frac{\left(k^{2}\right)'''}{12k}\frac{\partial^{3}\mathcal{E}}{\partial t^{3}} + \frac{in_{2}k}{n_{0}}\left(1+\frac{i}{\omega_{0}}\frac{\partial}{\partial t}\right)^{2}\left[(1-\alpha)\left|\mathcal{E}\right|^{2}+\alpha R(t)\right]\mathcal{E} = \frac{\partial\mathcal{E}}{\partial z}. \quad (4.14)$$

In order of their appearance, the terms in Eq. 4.14 include effects due to diffraction, space-time focusing, nonparaxiality, second-order dispersion, third-order dispersion, nonlinear shock, and a Kerr-type nonlinearity. The third-order Kerr-type nonlinearity includes terms for both instantaneous and delayed (Raman) contributions. An in-depth discussion of this equation can be found in a paper by Zozulya *et al.* [90] It should be noted that all of the parameters used in this equation are taken directly from published or experimentally determined values, and none are used as fit parameters in the calculations. Only diffraction, second-order dispersion, and the instantaneous nonlinearity are included in Eq. 4.13 and have been shown to predict symmetric pulse splitting. Again, the assumed input pulse is a Gaussian in both space and time and has characteristics similar to those of the experimental input pulses. Numerical experiments isolating the effects of each term individually during propagation through 3.0 cm of fused silica have been performed [90]. The effects of each additional term are described briefly in the following few paragraphs.

Raman Nonlinearity

As in the one-dimensional case, the Raman nonlinearity is included by replacing the instantaneous nonlinearity with a term that includes both an instantaneous and non-instantaneous response. In Eq. 4.14, $R(t)$ is the Raman nonlinearity given by

$$\int_{-\infty}^{t} f(t-t') \left|\mathcal{E}(t')\right| dt'$$

where

$$f(t) = \frac{1+(\omega_r \tau_r)^2}{\omega_r \tau_r^2} \exp\left(-\frac{t}{\tau_r}\right) \sin(\omega_r t) . \tag{4.15}$$

The principal change resulting from inclusion of the Raman effect is the asymmetry between the leading and trailing pulses. After propagation through a 3.0 cm sample, the leading pulse has almost twice the intensity of the trailing pulse. The relative increase of the leading pulse at the expense of the trailing pulse can be understood simply in terms of Raman gain. The response function given by Eq. 4.15 is simply the time-domain representation of the more common frequency-domain picture of stimulated Raman scattering. Stimulated Raman scattering can be described as the process in which a photon is absorbed, leaving an atom in a virtual state which then decays to a level that is higher or lower in energy than the initial state. Lower energy (Stokes) frequencies are observed more often than their higher energy (Anti-Stokes) counterparts because the ground state is more heavily populated than excited states. Therefore, Raman scattering preferentially amplifies red-shifted frequency components of the pulse at the expense of blue-shifted frequencies. Since, in this case, positive GVD moves the red components ahead of the blue components, it follows that the leading pulse becomes larger due to the Raman gain.

Shock terms

Both linear and nonlinear shock terms are included in Eq. 4.14. In the case of nonlinear shock, the peak of the pulse experiences a nonlinear increase in index of re-

fraction and thus experiences a slower group velocity than the lower intensity regions of the pulse. This results in shock formation at the trailing edge of the pulse. Simulations including only nonlinear shock indicate that, during the pulse splitting process, the trailing pulse starts off larger than the leading pulse. By the exit face of the sample, however, this asymmetry has reversed. The reason for this is that the shorter, more intense trailing pulse diffracts faster than the longer leading pulse in the absence of continued compression after pulse splitting. With an input peak intensity of $85\ \mathrm{GW/cm^2}$, pulses begin to split after about 2.0 cm of propagation and, by 3.0 cm of propagation, the leading pulse has a higher peak axial intensity than the trailing pulse.

Linear shock occurs in the space-time focusing term. Space-time focusing accounts for the group delay due to a nonzero angle between a ray and the optic axis. As a pulse passes through a nonlinear focus, some of the energy is shifted to later times by this effect. As a result, this linear shock also leads to an amplification of the trailing pulse. And, as with nonlinear shock, the trailing pulse diffracts rapidly after pulse splitting. For these experiments, contributions from linear shock are on the same order as those from nonlinear shock. A combination of both linear and nonlinear shock leads to more dramatic enhancement of the trailing pulse during the pulse splitting process.

The Raman nonlinearity, which preferentially intensifies the leading pulse, is not strong enough to completely offset the effects of the shock terms, however, it does serve to dampen them. With Raman included, the trailing pulse does not get as sharp or as intense during the splitting process. Also, the Raman nonlinearity contributes to a larger leading pulse at the exit of the sample.

Third-order dispersion

In the normal dispersion regime of fused silica, third-order dispersion acts to increase the GVD of blue components while decreasing the GVD of red components. As a result, the trailing pulse spreads faster than the leading pulse. In this way, third-

order dispersion results in a larger leading pulse. While contributions from third-order dispersion should not be ignored, they are smaller than those from Raman and shock effects.

Nonparaxiality

Nonparaxiality turns out to be a negligible effect in this regime. It may become important, however, during propagation at even higher powers, where the process of self-focusing results in smaller beam sizes before it is arrested by pulse splitting.

4.3.4 Results

Although the calculated examples here all point to split pulses with a larger leading pulse, changing input pulse parameters or propagating through a shorter sample (e.g. Fig. 4.4) can result in split pulses with the opposite symmetry. A comparison of the calculated field including the Raman nonlinearity, space-time focusing, nonlinear shock, and third-order dispersion in addition to diffraction, second-order dispersion and an instantaneous nonlinearity with an experiment involving similar peak input powers is shown in Fig. 4.11. The calculated field in this case is able to reproduce the asymmetry observed in the experiment. The overall downward curvature of the phase in both cases is indicative of an upchirp across the entire field, meaning that the leading pulse is red-shifted compared to the trailing pulse. Also, the rapid change in phase at the trailing edge of the experimental pulse is well modeled by the inclusion of shock terms. The calculated split pulses are narrower in time than the measured pulses. This may be explained by deviations of the experimental beam from an ideal Gaussian in space and time.

At higher peak input intensity, as in Fig. 4.4(d), the experiment observes the splitting of a pulse into multiple sub-pulses. Increasing peak input intensity in calculations using the modified NLSE given by Eq. 4.14, however, does not lead to splitting into

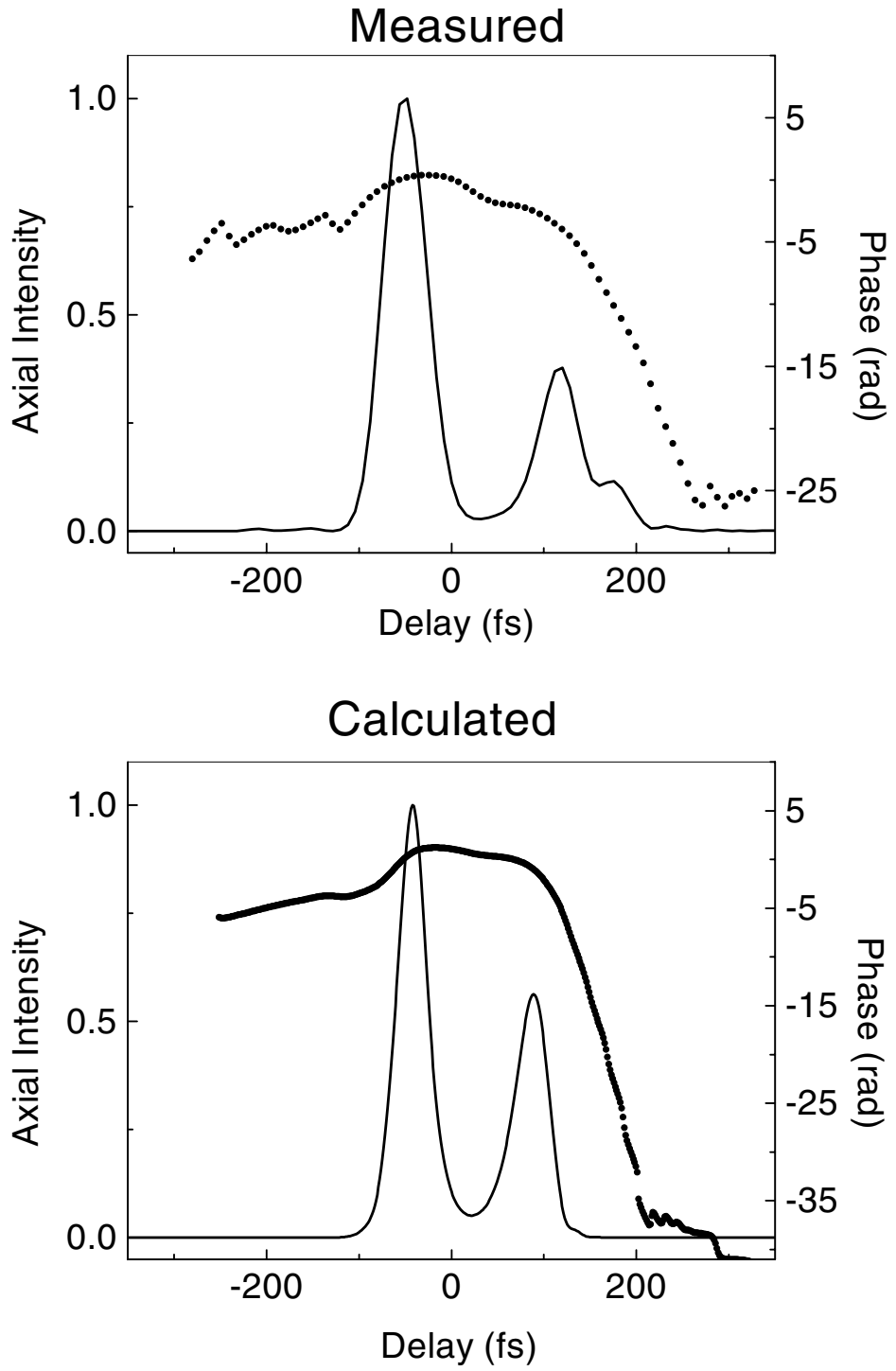

Figure 4.11: (a) Measured and (b) calculated on-axis intensity (solid line) and phase (dashed line) after propagation through 3.0 cm of fused silica. The input pulses for both the experiment and the calculation have a peak power of 4.9 MW. (Adapted from Ref. [90])

any more than two sub-pulses. The reason for this is that Eq. 4.14 calculates the field at the exit face of the sample. In the experiment, however, the pulse propagates for 75 cm before being measured with the SHG FROG. Another way of saying this is that the model calculates the near-field, while the experiment makes measurements in the far-field. The on-axis far-field can be calculated by integrating over the near-field spatial cross section for each temporal slice of the pulse. In other words, we assume that a spatial point in the near-field diffracts as a point source to the corresponding temporal plane in the far-field. A maximum in the far-field intensity can arise from either a cross section involving intense regions of the near-field pulse, or a cross section involving lower intensity regions of the pulse, but constant phase. A more in-depth discussion of this type of calculation can be found in Ref. [119]. A consequence of this calculation is that a maximum in the far-field can arise from a region of the near-field where the temporal intensity is near zero. The calculated spectrum does not extend quite as far to short wavelengths as the measured spectrum. One possible explanation for this result is the absence of multiphoton ionization in the model.

Figure 4.12 shows both the calculated near-field and far- field intensity profiles of a pulse after propagation through 3.0 cm of fused silica at two different input powers, along with the corresponding measured fields. The top row of Fig. 4.12 illustrates that full pulse splitting is observed in the far-field while only partial splitting has occurred in the near-field. Again, the asymmetry of the calculated field is similar to that of the measured field. The second row illustrates the case of a pulse in the far-field occurring in a region of the temporal axis that is a valley in the near-field. These calculations are now able to predict the splitting of a pulse into two or more sub-pulses. For completeness, the calculated and measured spectra corresponding to the pulses shown in the second row of Fig. 4.12 are plotted in Fig. 4.13. The spectra are broadened significantly after propagation and are plotted on a log scale to illustrate the agreement even in the low intensity spectral wings of the pulse. Figure 4.13(a) shows both the spectrum retrieved

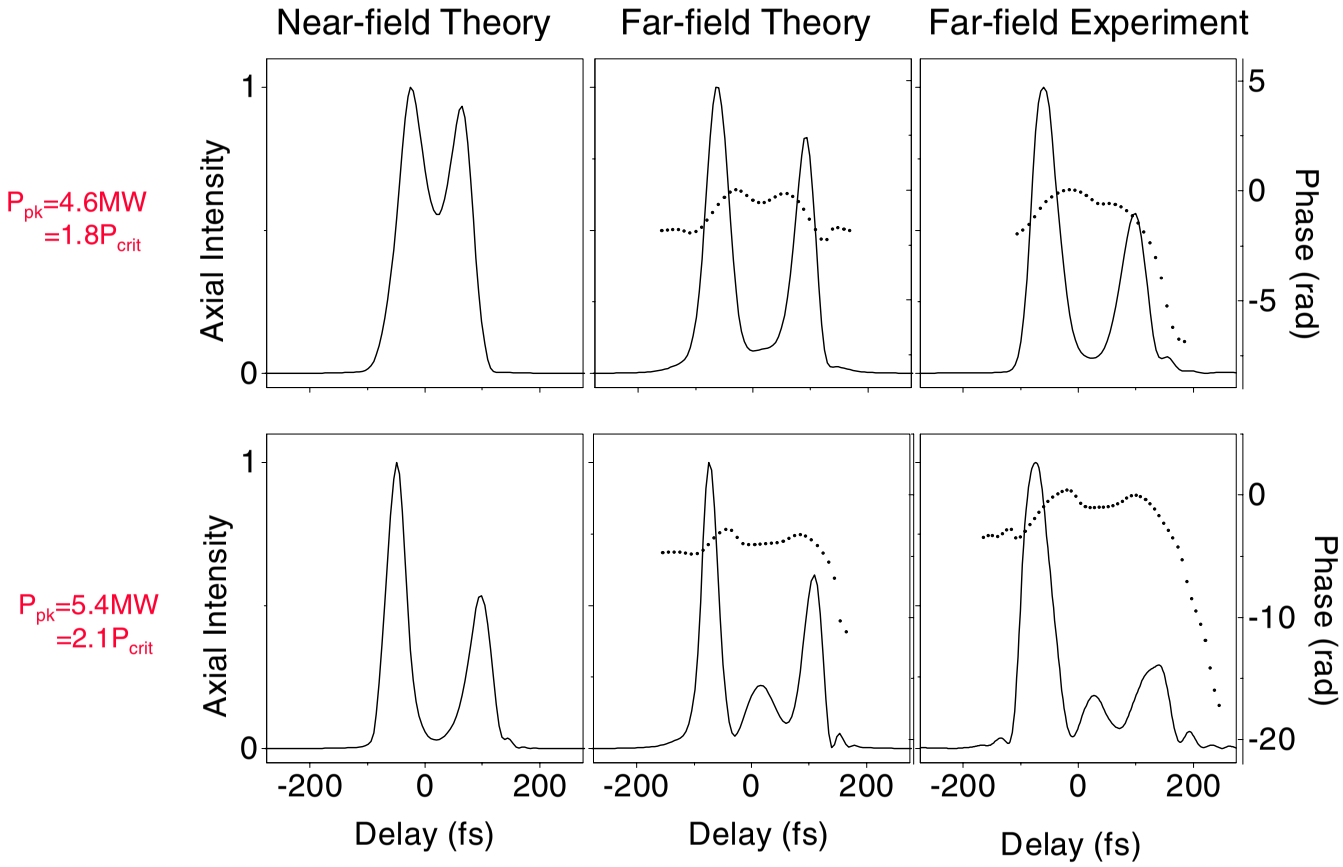

Figure 4.12: A comparison of near- and far-field theory with the far-field measurements at two different input peak powers as indicated in the figure. Lines represent the intensity; and points, the phase. (Adapted from Ref. [119])

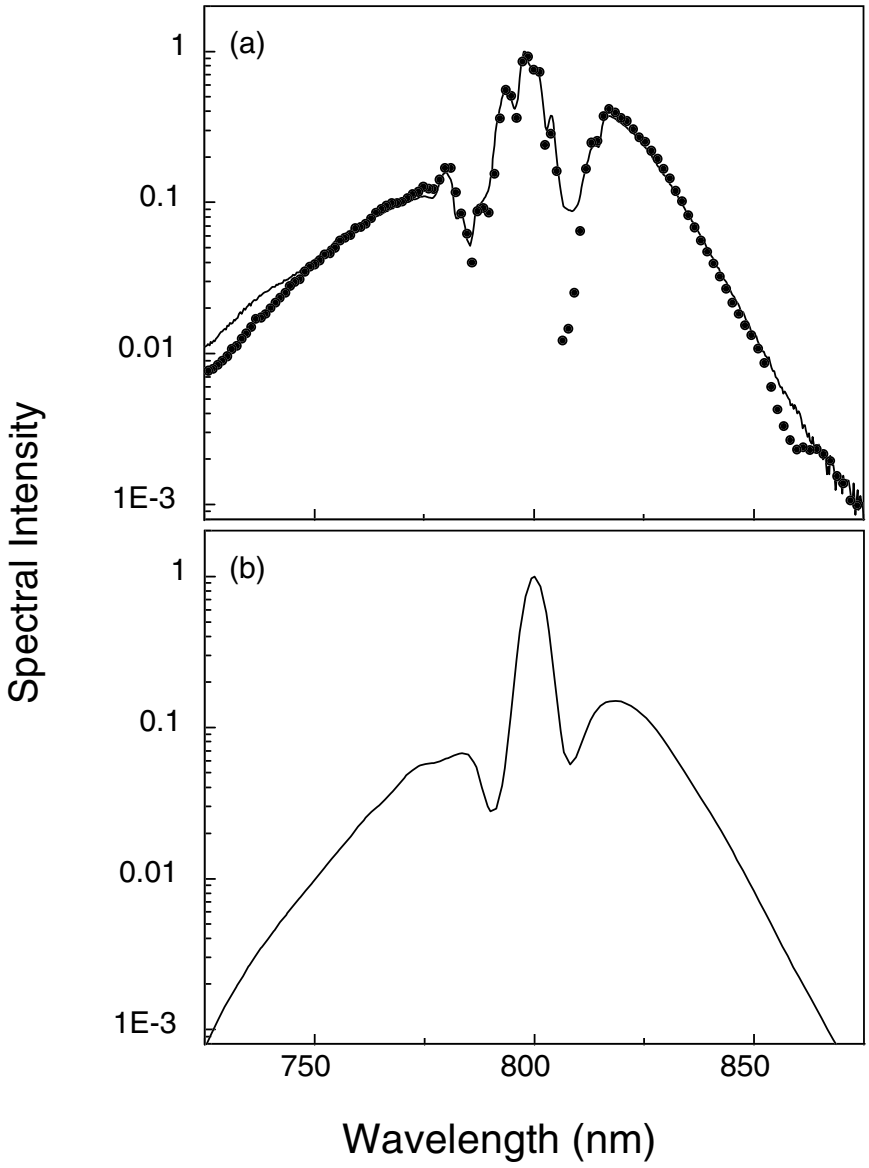

Figure 4.13: Measured (a) and calculated (b) spectra corresponding to the data in the second row of Fig. 4.12. In (a) the solid line is the independently measured spectrum, while the points represent the retrieved spectrum. (From Ref. [89])

from the SHG FROG measurement, and an independently measured spectrum. Figure 4.13(b) shows the calculated on-axis far-field spectrum. All major features, in both the time and frequency domains, are reproduced by the calculation.

Previous theories concerning multiple pulse splitting often relied on one pulse splitting into two pulses and each of these pulses undergoing secondary splitting. The calculations presented here indicate that this does not have to be the case, and in most situations, multiple pulses in the far-field arise from constructive and destructive interference of components of the near-field pulse in the far-field. In addition, the calculations indicate that the position of maximum self-focusing, which occurs in the medium, and the position of pulse splitting are spatially separated along the propagation axis. The pulse first self-focuses and then, at some later propagation distance, it splits. Moreover, the distance between the self-focusing event and the splitting is inversely proportional to the input power.

4.4 Summary

This chapter demonstrates the ability of FROG to follow nonlinear propagation in systems where both instantaneous and noninstantaneous nonlinearities are present. Our experiments have shown that SHG FROG is capable of high-dynamic range measurements of complicated pulses having over 100 nm of total spectral bandwidth. Experiments involving temporal pulse splitting exemplify the mutually beneficial relationship that is possible between experiment and theory. These experiments also demonstrate the ability of FROG to lend insight into the nature of complex propagation problems.

In the plane wave regime, a (1+1)-D model based on the nonlinear Schrödinger equation compares favorably with measurements. These experiments illustrate the importance of the interplay between GVD and SPM that leads to dramatic temporal broadening of a pulse.

At experimental conditions where the pulse undergoes self-focusing during prop-

agation, we observe the splitting of the pulse into two and more sub-pulses, each of which has a shorter temporal duration than the initial pulse. The overall upchirp across the split field indicates that the leading pulse is red-shifted compared to the trailing pulse. The asymmetric nature of the measured split pulses indicates that a simple (3+1)-D NLSE is not sufficient to describe the propagation. The asymmetry can be accounted for numerically with the addition of a Raman nonlinearity, nonlinear shock, space-time focusing, and third-order dispersion to a basic (3+1)-D NLSE.

We find that shock terms have the largest effect on the propagation, resulting in an enhancement of the trailing edge of the pulse in the time domain. This sharp trailing pulse diffracts faster than the leading pulse and appears less intense at the exit of a 3.0 cm sample. The Raman nonlinearity serves to partially offset the effects of shock and results in a red-shifting of pulse frequencies. In the presence of positive GVD, this red-shift contributes to the larger leading pulse observed in some experiments. Contributions from third-order dispersion are much smaller, but they do affect the symmetry of the split field. In addition, this work demonstrates that, at high peak powers, a pulse splits into more than two sub-pulses.

Extension of the calculation to include propagation to the far-field correctly predicts multiply-split pulses for the first time. In the following chapter, experiments carry this research into even higher intensity regimes where continuum generation accompanies pulse propagation.

Chapter 5

Continuum Generation

We have seen in the previous chapter that at powers high enough for self-focusing, interesting pulse propagation dynamics can result. Experiments above the critical power for self-focusing can result in the splitting of pulses into two or more sub-pulses. This pulse splitting arises in part because of the broad spectral bandwidths that are created by self-phase modulation and then separated temporally by group velocity dispersion. But, what happens at even higher input powers? Do the pulses continue to split into even more sub-pulses? And how broad does the spectrum get? It has been observed that at powers above the critical power for self-focusing, propagation in solids, liquids, and gases can produce an extremely broadened spectrum. The range of wavelengths produced often spans the entire visible spectrum and extends into both the IR and the UV. This phenomenon has been called spectral super-broadening or continuum generation. The continuum spectrum produced has been used in optical parametric amplification [120, 47, 121, 122], time-resolved broadband absorption and excitation spectroscopy [123, 124], and the generation of short pulses [125]. The exact process responsible for the generation of this continuum, however, is currently unknown.

Spectral super-broadening was first observed by Alfano and Shapiro in 1970 [126]. Their experiment involved propagating $530\ \mathrm{nm}$ picosecond pulses in glass with an input power of $\sim 1\ \mathrm{GW/cm^2}$. At the output, they observed a spectrum that spanned from $400\ \mathrm{to}\ 700\ \mathrm{nm}$. They also observed the formation of self-trapped filaments within

the glass. The first evidence of self-trapped filaments was reported in 1964 when extremely long, thin damage spots were observed in glass and other materials [127]. For self-trapped filaments to form, a process must be involved that arrests the self-focusing effect and allows the pulse to propagate without spreading. Self-trapped filaments have been explained in a variety of ways. Some of these explanations include a self-produced dielectric waveguide [128], a self-guiding structure similar to a fiber consisting of a Kerr cladding and a weakly ionized core [129], and as a moving focus [130]. One or more self-trapped filaments are often present with continuum generation. It has been asserted that regardless of the medium in which the continuum is generated, two requirements for continuum generation are self-trapped filaments and dielectric breakdown [131]. Although the validity of the first remains a question, the second has been proved incorrect. Evidence that dielectric breakdown is not necessary for continuum generation is found in the properties of the transmitted continuum beam. The spatial properties are only slightly modified from that of the incident beam [132], and the emitted continuum is collimated, modulated, and polarized [133]. Dielectric breakdown should result in emission that is neither collimated nor polarized. The necessity of self-trapped filaments has been brought into question by an experiment involving continuum generation in a thin ($500\ \mu\mathrm{m}$) jet of ethylene glycol [43]. The length of the sample is small enough that self-trapped filaments may not form. The role of self-focusing is also minimized in this experiment. It is commonly believed, however, that self-focusing plays an important role in the continuum generation process. That self-focusing is important is evidenced by the fact that continuum generation only occurs with input powers above the critical power for self-focusing [134].

The white light continuum appears as a central beam of white light surrounded by rings of color. These rings do not extend continuously from the central white light, but occur as distinct rings of red, green, and blue light, often separated from the central white light beam — and from each other — by rings of darkness. The higher

frequency light appears in the outermost ring, and the lower frequency light forms the ring nearest the white light continuum. This arrangement of frequency components is exactly opposite that which would be predicted by diffraction. An example of white light continuum generated in sapphire is shown in Fig. 5.1. The central white light continuum is also observed to be both spatially [133, 41] and spectrally modulated [131, 132, 134, 41]. Super-broadened spectra have been observed in a variety of materials including glasses such as fused silica and BK-7 [133, 135]; crystals such as calcite, quartz, sodium chloride and potassium bromide [133, 136]; semiconductors such as gallium arsenide and zinc selenide [136]; gases such as neon, argon, krypton, xenon, nitrogen and air [137, 132, 134, 138, 129]; and liquids such as water, methanol, carbon tetrachloride, carbon diselenide, and benzene [131, 135]. Both picosecond and femtosecond pulses have been used to generate continua, with incident pulses spectrally centered from around 248 nm [134] to around 9.3 μm [136]. Continuum spectra under all conditions share certain similarities including the central white light continuum surrounded by rings of color, an asymmetric pulse spectrum with the blue spectral wing extending further than the red, a dependence on input power rather than intensity, and a polarization that is in the same direction as that of the input pulse. These striking similarities indicate that the mechanism responsible for continuum generation is very general, having little to do with the spectroscopic features of the material involved. The width of the spectrum generated is, however, dependent on the medium in which it is generated [124], but it does not scale with the size of the nonlinear index of refraction as might be expected. In fact, in materials with high n_2, and therefore stronger self-focusing and self-phase modulation, the spectrum is actually narrower than for materials with low n_2 [135].

Several approaches have been taken to explain the observed spectra. On first observing continuum generation in glass, Alfano and Shapiro attributed the broad spectrum to a stimulated, nondegenerate four wave mixing process [126]. This four wave

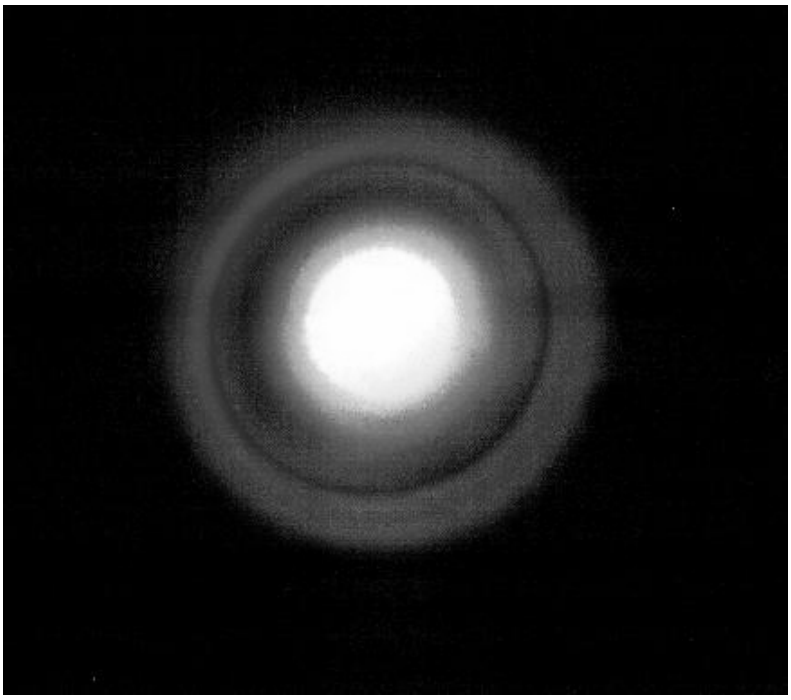

Figure 5.1: Far-field image of continuum generated in sapphire.

mixing paradigm was championed in many following papers by Penzkofer *et al.* [139, 140, 141, 142]. Penzkofer's work asserts that there are several processes that can be involved in continuum generation. The primary process is the amplification of quantum noise by a stimulated, parametric four-photon interaction. In certain materials, and under certain conditions, stimulated Raman scattering and a second parametric process driven by the pump laser and stimulated Raman light come into play. These generated frequencies can result in a cascaded frequency upconversion effect, generating a broad spectrum. The asymmetry of the spectrum is explained as absorption of the red and infrared components of the pulse [141]. Experiments by this same group indicate that the on-axis spectrum consists of a spectrally broadened central peak, with low intensity wings extending into the UV and IR. The four-wave mixing theory predicts broad wings, but it does not account for the significant broadening near the input wavelength. To explain this effect, self-phase modulation is invoked as a special case of four-wave mixing in which the amplified wavelengths are already present in the pulse and do not need to arise from quantum noise. Although this four-wave mixing theory does predict broad spectral wings, it predicts a peaked spectrum corresponding to Raman resonances in the material. The experimentally observed spectra are often modulated, but the peaks do not always occur at the predicted frequencies. In addition, this theory fails to account for self-focusing in the medium, and it fails to address the ring structure observed surrounding the central white light continuum. Although it predicts a very broadened spectrum for special cases where the resonant structure of the material is conducive to strong Raman scattering, the theory does not appear to be as universal as experiments indicate continuum generation is.

Several attempts have been made to model continuum generation by more rigorously solving the nonlinear wave equation for pulse propagation. The wave equation, accounting for self-phase modulation, four-wave mixing, and self-steepening and neglecting dispersion, predicts an asymmetric spectral broadening. The predicted broad-

ening, however, is less than the observed broadening [143]. Another work, in which the same basic equation is solved using a different method, is able to predict broader pulses [144]. In both cases, however, dispersion is assumed to be zero. This assumption is valid when comparing to continua generated in gases, but it is invalid in experiments involving most liquids and solids. That dispersion plays an important role in propagation has already been demonstrated in Chapter 4 of this thesis where it is shown that dispersion leads to temporal pulse broadening and arrests the collapse of a self-focusing pulse. In addition, self-phase modulation implies increased broadening with a higher nonlinear index of refraction in contrast to experimental evidence.

It has been observed that self-trapped filaments are nearly always present during continuum generation. These self-trapped filaments can only form if there is a process occurring in the medium that stops the collapse of the pulse due to self-focusing. The approach can then be taken that the processes involved in halting the collapse and allowing the formation of self-trapped filaments are most likely also responsible, at least in part, for continuum generation [114]. It was proposed that plasma formation, and the associated appearance of free electrons, was sufficient to stop the collapse and simultaneously enhance SPM such that a broad spectrum results [145]. Although this predicts a broad blue-shifted spectrum, the associated loss of energy is much higher than that observed [137]. Another twist on the influence of ionization was proposed [129] that describes the self-trapped filament as a leaky anti-guiding structure with a Kerr type cladding and a slightly ionized core. The nonlinear index is high at the edge of the trapped pulse but falls off toward the center due to the influence of free electrons. This antiguide cannot support stable propagation modes because of the lack of total internal reflection and thus loses some energy through refraction. The theory proposes that quasi-stable modes exist and that refraction losses are responsible for the off-axis ring structure surrounding the white-light continuum in the far-field. Spectral broadening of the guided light is attributed to SPM.

The most promising theory to date describes continuum generation in condensed media and is again based on the generation of free electrons [135, 146]. In this theory, Brodeur and Chin assert that it is not plasma formation that generates the free electrons, but a multiphoton excitation (MPE) of electrons from the valence band to the conduction band. This MPE is a bandgap dependent process, and experiments in several liquids and solids have shown a dependence of the self-focal diameter on the bandgap of the material [135, 146]. The basic premise of this theory is that as the pulse undergoes self-focusing, different temporal slices of the pulse reach a maximum intensity where MPE occurs. MPE generates essentially free electrons, which serve to decrease the index of refraction and arrest the focusing. The sudden change in index of refraction results in a sudden drop in the phase. A change in phase with respect to time gives the instantaneous frequency. In this way, MPE generates a broad blue-shifted spectral wing. This theory is based on a moving focus model of pulse self-focusing [130, 147, 114], which is also applied to the continuum problem by Strickland and Corkum [41]. According to the moving focus model, the pulse is divided into discrete temporal slices that undergo self-focusing independently. Because each slice has a different power, various slices focus to different positions along the propagation axis. These slices in effect form temporally narrow transient sub-pulses. According to Strickland and Corkum, these sub-pulses generate continua via an on-axis phase retardation. The observed continuum spectrum is the summation of the broadened spectra produced by each of these transient sub-pulses. The spatial and spectral modulation characteristic of the observed continuum can be explained as far-field interference resulting from the multiple broad-bandwidth sources. The more modern theory relies on MPE instead of an on-axis phase shift and thereby inherently includes a dependence on the band gap of the medium.

5.1 On the Verge of Continuum Experiments

In an effort to better understand the continuum generation process, and in light of the excellent agreement between the (3+1)-D theory and our FROG measurements above the critical power for self-focusing presented in Chapter 4, our group pushed FROG measurements into the region just above the continuum formation threshold [119]. During these measurements, blue light was clearly visible by eye. To ensure that the phase matching bandwidth of the second harmonic generating crystal in the FROG device was adequate, the $100\ \mu\mathrm{m}$ BBO crystal was replaced by a $50\ \mu\mathrm{m}$ BBO crystal. As in the pulse splitting measurements, the laser beam was spatially filtered and focused to a FWHM spot size of $70\ \mu\mathrm{m}$ at the entrance face of a $3.0\ \mathrm{cm}$ long fused silica sample. SHG FROG measurements of the on-axis far-field were performed before and after propagation through the sample. The input pulses were nearly transform-limited with an intensity duration of ~ 90 fs FWHM.

Figures 5.2 (a) and (b) show the measured on-axis intensity after propagation for input peak powers of $6.8 \text{ and } 7.4\ \mathrm{MW}$, respectively. From the pulse splitting experiments performed in Chapter 4 we might expect the pulse to split into many more sub-pulses with these higher input powers. As the peak input power is increased, however, the sub-pulses begin to coalesce into a single broad pulse [119]. Calculations using Eq. 4.14 without the nonparaxiality term are shown in Figs. 5.2 (c) and (d). The input powers used in the calculation match those of the experiment to within 15%. In both the experiment and the calculations, as input power is increased, the central peak broadens and merges with the leading and trailing peaks.

Calculations at lower powers have shown that the splitting of the pulse into two sub-pulses arises first in the far-field and progresses to the near-field with increasing input power. Multiply-split pulses are observed in the far-field when the near-field is fully split into two sub-pulses. At higher input powers, however, multiply split pulses

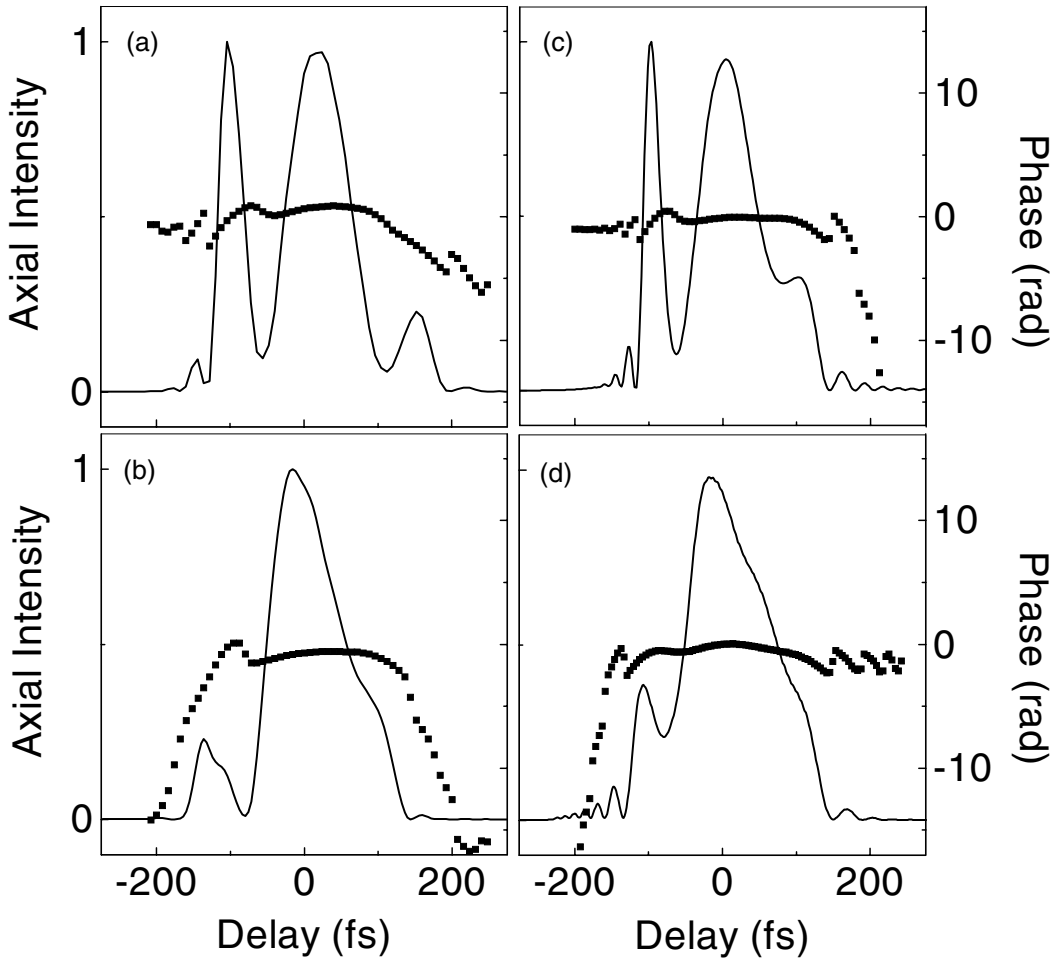

Figure 5.2: Measured axial intensities and phases for input powers of (a) 6.8 MW and (b) 7.4 MW. The corresponding calculated intensities and phases are shown in (c) and (d). (From Ref. [119])

do not appear in the near-field. Although the near-field is modulated, distinct multiple splitting arises only from the build-up of phase in the far-field as described previously and does not arise from the same physical processes responsible for the initial pulse splitting.

Measured and calculated spectra corresponding to the temporal intensity profiles displayed in Figs. 5.2 (b) and (d) are shown in Figs. 5.3 (a) and (b), respectively. The spectra are plotted on a log scale to emphasize the long tail extending to both sides of the central peak. By contrast, a bandwidth-limited, 100 fs Gaussian pulse centered at 800 nm would have wings with an intensity three orders of magnitude lower than those shown here just 50 nm on either side of the peak. These tails are thus evidence of weak continuum generation. The short wavelength tail of the calculated spectrum falls off faster that that of the measured spectrum. As indicated by the theory of Chin and Brodeur [135, 146], inclusion of multiphoton excitation in the theory may account for this difference.

5.2 Full Continuum Experiments

To improve and test the theory, good experimental data with which to compare is essential. Careful studies of continuum generation are difficult because of the broad bandwidths involved. With spectra spanning several hundred nanometers, an accurate intensity autocorrelation is difficult, if not impossible, because of the phase-matching bandwidth required. Since FROG is an autocorrelation-based device, increasing the input power above that used for Fig. 5.2 (b) quickly results in spectrally broad pulses for which the validity of SHG FROG comes into question. In addition, continuum pulses diverge quickly after exiting the medium and result in very low on-axis intensities. These intensities can be sufficiently low that a SHG FROG signal is difficult to obtain. Near-field SHG FROG measurements could be performed by imaging the output face of the sample onto the entrance aperture of the FROG apparatus. Such a measurement

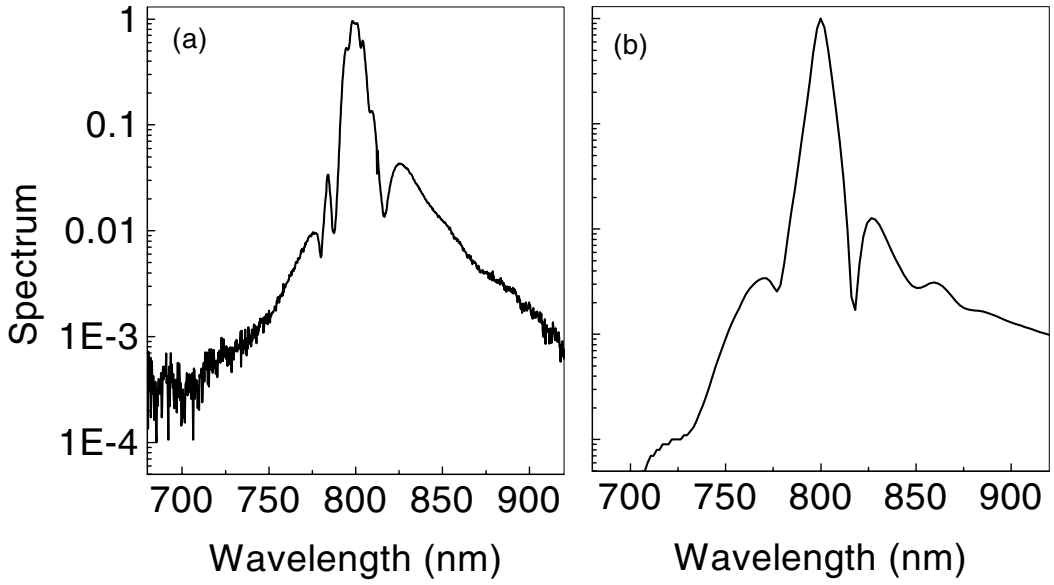

Figure 5.3: (a) The measured axial spectrum for an input power of 7.4 MW, and (b) the corresponding calculated spectrum. (From Ref. [119])

would suffer the same phase-matching bandwidth limitations, however, and near-field SHG FROG measurements have not been tested in simpler propagation regimes. For these reasons, temporal measurements of the field after propagation are not practical. Therefore, careful measurements of the spectrum and other empirical parameters are used for comparisons with theory at this time.

All data presented to this point have concentrated on the on-axis field before and after propagation. In an attempt to gain insight into the continuum generation process, we add a spatial dimension to the spectral measurements. Qualitative spatial-spectral, far-field measurements have been available for years in the form of verbal and pictoral descriptions of a white light beam surrounded by rings of color. The only previous quantitative measurement, by Strickland *et al.* [41], recorded the spatial spectrum of the far-field using a spectrometer and CCD. This chapter reports the first careful measurements of the near-field spatial spectrum of continuum pulses (Section 5.2.4). Detailed investigations of power loss and continuum behavior as a function of input power and timelapse are also reported in Sections 5.2.2 and 5.2.3.

For these measurements, spatially filtered pulses are focused at the input of the fused silica to a spot size of $33\ \mu m$ FWHM or a $26\ \mu\mathrm{m}$ radius at $1/e^2$ of intensity with a 10 cm focal length lens. The fused silica sample length is reduced to 0.318 cm. These changes are made to better facilitate comparisons with theory. Self-focusing plays an important role in continuum generation, reducing pulse radii during their passage through the sample by an order of magnitude to approximately a few microns. These dramatic changes in beam size require different stages of the propagation to be calculated on different size grids. To minimize the associated difficulties, we focus to a smaller initial spot size to reduce the amount of spatial beam compression that occurs during propagation. A shorter sample can thus be used since the propagation-limited beam size is reached sooner.

5.2.1 Qualitative Observations

The generated continuum exits the sample and propagates 10 cm to a white card where it is observed by eye. Observations are also made after the beam travels 35 cm to a white card. These observations differ from those at 10 cm only in that the beam is much larger and therefore weaker by eye. Subtle changes in the continuum behavior are more easily observed on the card placed 10 cm after the sample, so those observations are reported here.

Continuum spectra are generated with input peak powers ranging from 2.7 to 12.6 MW. Self-trapped filaments are not visible by eye in the sample; the sample is short enough, however, that they may be difficult to observe under these conditions. At the lowest powers, the beam on the card looks like a small red spot. As input power is increased, the red spot grows larger until white light begins to appear in the center, surrounded very closely by rings of blue and green. I should point out that in these experiments the continuum never goes through a stage where the central red spot is surrounded by a blue ring as was seen in the earlier experiments. This is most likely a result of the smaller focusing geometry used here. It is probable that in selecting input powers to sample, we took too large a step and missed the transition from a red spot to red surrounded by blue before the central white light spot appears. At an input power of 4.5 MW the green and blue rings are larger, and the white center takes on a yellow-orange hue. Following this, green frequencies begin adding into the central beam and then it appears white again. At an input power of 5.8 MW, a red outer ring appears separated from the white/blue/green structure by a large black ring. As the input power is increased further, the red and blue rings grow fatter. At an input power of 7.4 MW, a thin yellow ring forms around the outer edge of the red ring. This yellow ring is tenuous, and seems to appear and disappear many times per second. The white center again turns a yellow-orange color at a peak input power of 9.9 MW. And at 10.8

MW rings of black separate each ring of color surrounding the again white center. At this point, we see a strong white light central beam surrounded by a ring structure that consists, going outward from the center, of a thin black ring, a thicker blue ring, a second thin black ring, a thin green ring, a thick black ring, and a thick red ring with a thin yellow lining at the outermost edge. Increasing the power to 12.6 MW results in a similar far-field structure with the addition of a second outer red ring. Again, all color rings are separated by areas of darkness. The appearance of this ring structure is reminiscent of some kind of interference, but the mechanism that is actually channeling light off axis is unknown. Also, the appearance of two distinct outer red rings begs the question of whether one ring may be the result of the continuum generation process while the other is actually fundamental light being funneled off axis, or if both are created via the same mechanism.

This data is presented as if one always observes a distinct set of concentric rings in the far-field. In reality, though, one occasionally observes a pattern that resembles a series of overlapping concentric ring sets, each with a different spatial center. By slightly moving the sample, however, the far-field ring structure can be returned to the desired concentric ring pattern. It is also interesting to note that the power throughput is different in these two cases. Power measured after the sample is on the order of 10% higher when a single ring structure is observed. These patterns have been reported once before and were attributed to fluctuations due to plasma buildup [131]. I believe, however, that these differing patterns can be explained by considering the formation of self-trapped filaments. If a single ring structure results from continuum generation along a single trapped filament, then these more complicated patterns probably arise from the formation of multiple filaments. Continuum is generated along each filament and the resulting concentric ring patterns overlap in the far-field. For all of the data presented in this chapter, care was taken to ensure that only a single ring structure was present during the measurement.

It is interesting to note that although self-focusing and continuum generation are power dependent effects, the power figures presented in this chapter seem to indicate that continuum is occurring at the same powers at which we previously reported pulse splitting. One possible explanation for this is that the experimental set-up for these experiments is different from the pulse splitting experiments in that a shorter sample and a smaller focal spot are used. The pulse enters the sample with a much higher initial intensity than in the pulse splitting experiments. In those experiments, the pulse is spectrally broadened and GVD acts to spread the pulse in time, initiating pulse splitting. By the time the pulse reaches the same peak intensity used in the continuum experiments, significant spectral broadening has already occurred. Therefore, we should expect the propagation dynamics to be somewhat different in the two cases.

5.2.2 Power Throughput as a Function of Intensity

The power measurements presented here and in the next section were performed using a large area photodiode detector based power meter. The continuum light generated during propagation diverges rapidly after exiting the sample. Therefore, the power meter was placed as close as possible to the output face of the sample to collect all of the emitted light, including both the central white light and the colored rings.

Figure 5.4 shows the percentage of power lost during propagation as a function of input power. This percentage was determined by measuring the power with and without the sample present in the beam path. The two lowest power points in Fig. 5.4 correspond to situations where no central white light beam is observed. As the white light continuum appears, the losses jump to $\sim 15\%$. As power is increased, the overall trend is for the losses to increase as well up to an input power of 8.0 MW. There are three points, however, that do not follow this trend. At input powers of 4.5 and 10 MW, denoted by circles in Fig. 5.4, the losses are much lower than expected. Interestingly, it is at these powers that a yellow-orange color is observed in the central white-light

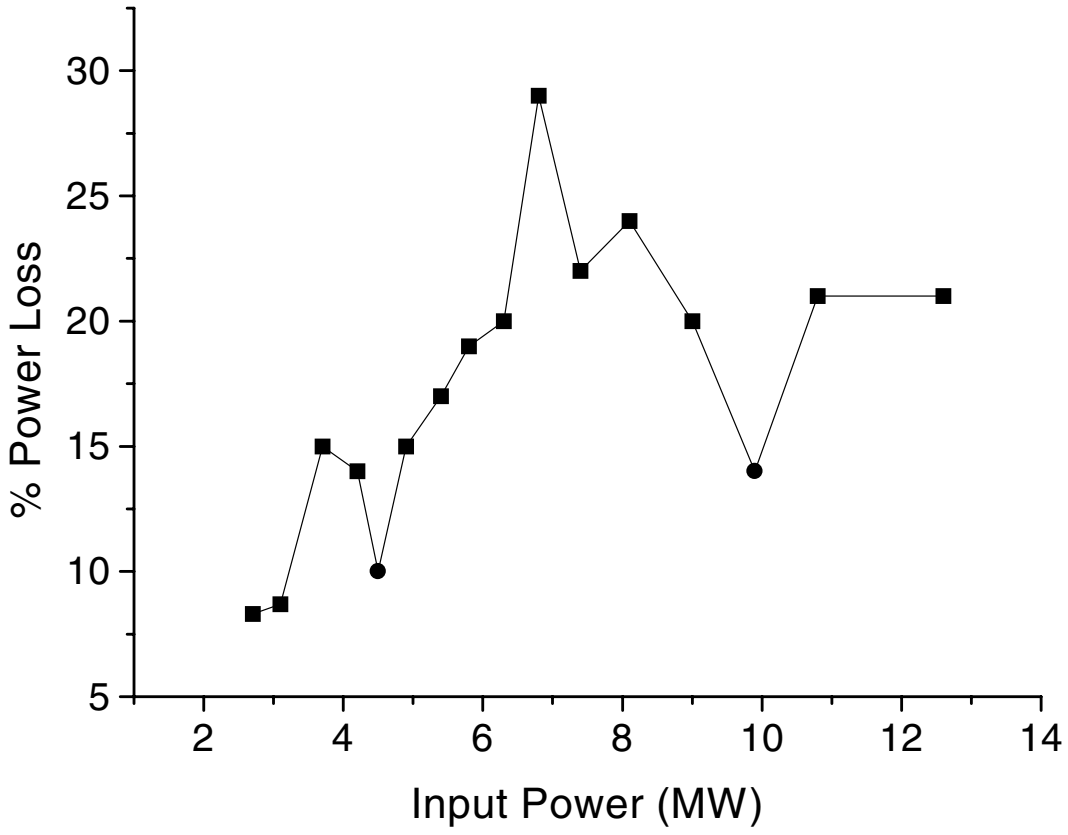

Figure 5.4: The percentage of power lost during propagation as a function of input power. The circles represent points at which the central far-field beam is yellow-orange instead of white.

region of the beam. The very high loss observed at 6.8 MW does not seem to correlate to any of the observed continuum behaviors.

Overall, it is evident that the processes involved in continuum generation involve a loss of overall power during propagation. This lends credence to the idea that multi-photon excitation or an absorption process may be involved. In fact, calculations based on the (3+1)-D theory presented earlier and including four-photon absorption predict accumulated losses of 12-14% for an input power of 12 MW [148].

5.2.3 Power Throughput as a Function of Time

Power measurements are also performed as a function of time. For these measurements, a post holder is attached to the optical table behind the sample, and a collar is placed on the post of the power meter head to ensure that the power meter could be removed and replaced to the same position. First the power without the sample present is measured. Next the beam is blocked, the sample is added into the beam path, and the power readings are recorded as soon as the beam is unblocked. The power meter is then removed from the beam path while the beam continues to propagate through the sample. The power meter is replaced and power measurements are made at intervals of several seconds to several minutes for approximately one half hour. The detector is sensitive to changes in temperature, therefore the power meter is removed between measurements to avoid unnecessary heating. After each set of measurements, the power is again measured without the sample present to check that the laser power has not drifted during the measurement.

When the laser first traverses the sample, the power loss discussed in the previous section is evident. At low input powers, after the beam is incident on the sample for several minutes, the output power begins to rise. After sufficient time, the power at the output is very nearly the same as the input power. At higher input powers, the output begins to rise after a shorter time. For an input peak power of 13 MW the output power

matches the input power after only 15 seconds. During the time the output power is rising, the far-field continuum structure also changes. Initially, a typical ring structure including the thin yellow lining around the outermost red ring is observed as described in Section 5.2.1. As the output power increases with time, the outer yellow lining disappears from around the red ring and simultaneously, the central white light region takes on a yellow hue. The initial power loss followed by a return of the output power to the value of the input is likely a result of a saturable absorption in the material. That the output power rises sooner with higher input powers is consistent with a saturable absorption.

After longer periods of time, the output power again begins to drop. Again, the amount of time that passes before this event occurs decreases with increasing input power. With an input power of 3.7 MW, just above the power where a strong central white light spot is observed, the output power drops by roughly 40% after 10 minutes. After the power drops, the far-field has lost its white light characteristics and appears as a red spot that is roughly the same diameter as the white light spot that preceded it. When the sample is moved slightly such that the beam traverses a different spatial path through it, the original white light continuum beam returns. These observations suggest that even at the lowest powers for continuum generation damage is occurring in the fused silica. Damage by short IR pulses in fused silica has been reported previously and is associated with a rapid buildup of electrons in the conduction band [149]. This damage thus provides further evidence that free electrons may be implicated in the continuum generation process. A different study on the formation of color centers in glasses asserts that continuum generation is actually responsible for the damage to the glass [150]. The study finds that color centers are formed by one- or two-photon absorption of the short wavelength continuum light generated by the propagation. This same study, however, finds no evidence of the formation of color centers in fused silica, although they may have formed and not been observed.

5.2.4 Near-Field Spatial Spectrum

Measurements of the spatial spectrum are performed by imaging the exit face of the sample onto the entrance slits of a 0.25 meter imaging spectrometer with an $f = 10$ cm lens and a magnification of 16. A radial slice of the beam is selected by the entrance slit, dispersed, and imaged onto a 16 bit CCD camera. A mask in front of the slit allows the central, high intensity portion of the beam to be blocked when measuring the radial extremes so that more than four orders of magnitude of intensity variation can be acquired. A long pass filter is employed when measuring the high frequency side of the spectrum to ensure that only the first order diffracted light from the grating is collected. Neutral density filters are placed in the beam path when necessary to prevent camera saturation. The entire spectrum cannot be captured in a single measurement because the grating is more dispersive than the CCD element is large. Therefore, a series of 10 to 14 spatial-spectral measurements corresponding to different wavelength regimes are necessary to obtain the full spatial spectrum at each input power. A corresponding background spectrum is subtracted from each individually measured spectrum to account for the differing exposure times and filtering used in each measurement. Each spatial spectrum is normalized such that its spectral edge matches the edge of the one obtained for the wavelength range adjoining it and the full spatial spectrum is pieced together. When measuring spectra over such a broad range of wavelengths, it is also important to consider the efficiencies of both the spectrometer grating and the CCD. The grating efficiency is known from 300 to 1000 nm. While the camera efficiency is only calibrated from 625 nm to 975 nm, the general shape of the efficiency curve is known over a larger range. Since continuum spectra usually fall off quickly on the long wavelength side, the limitations for the red components are not severe. The short wavelength spectrum, however, often extends well below 625 nm. Fortunately, the grating efficiency of the 300 groove/mm grating used here is increasing in the region of 300 to

roughly 600 nm where it peaks. Over this same range, the camera efficiency is falling off such that combined efficiency is relatively flat over this range. For this data a flat efficiency with a value of the known efficiency at 625 nm is assumed over the range 400 nm to 625 nm.

Figure 5.5 shows the near-field spatial spectrum for an input peak power of 12 MW. Only one measurement of the radial position at each wavelength range is shown in this plot. During the measurement, the continuum character changed such that the data from the low intensity wing was no longer related to the higher intensity spatial data shown here. This is probably a result of the sample being damaged with time as discussed in the previous section. Rings of color would be represented in this plot as a particular wavelength showing up primarily at two distances, equidistant from the central peak. Since rings are observed to form with lower frequencies at the outermost edge, these rings should appear as a v-shaped peak or set of peaks that opens toward the distance axis in Fig. 5.5. It is evident from this data that the ring structure exists only in the far-field. Spatial modulation of the near-field occurs near the on-axis portion of the beam. Although the far-field continuum spectrum appears to have strong radial symmetry, the near-field spatial modulation does not reflect this symmetry. An interesting feature is the peak around $580\ \mathrm{nm}$. This peak is roughly six orders of magnitude less intense than the peak near $800\ \mathrm{nm}$. This peak is better illustrated by plotting the on-axis spectrum as shown in Fig. 5.6. This spectrum also exhibits a strong spectral asymmetry in the generation of continuum. The short wavelength side of the spectrum extends much further than the long wavelength side.

Lineouts of a spatial spectrum obtained with a lower input peak power of 3.6 MW are shown in Figs. 5.7 and 5.8. Figure 5.9 shows the on-axis spectrum in this case. As in the higher power case, the on-axis spectrum extends further to short wavelengths than do the spectra at other radii. In this low power case, however, the peak at 580 nm is nonexistent.

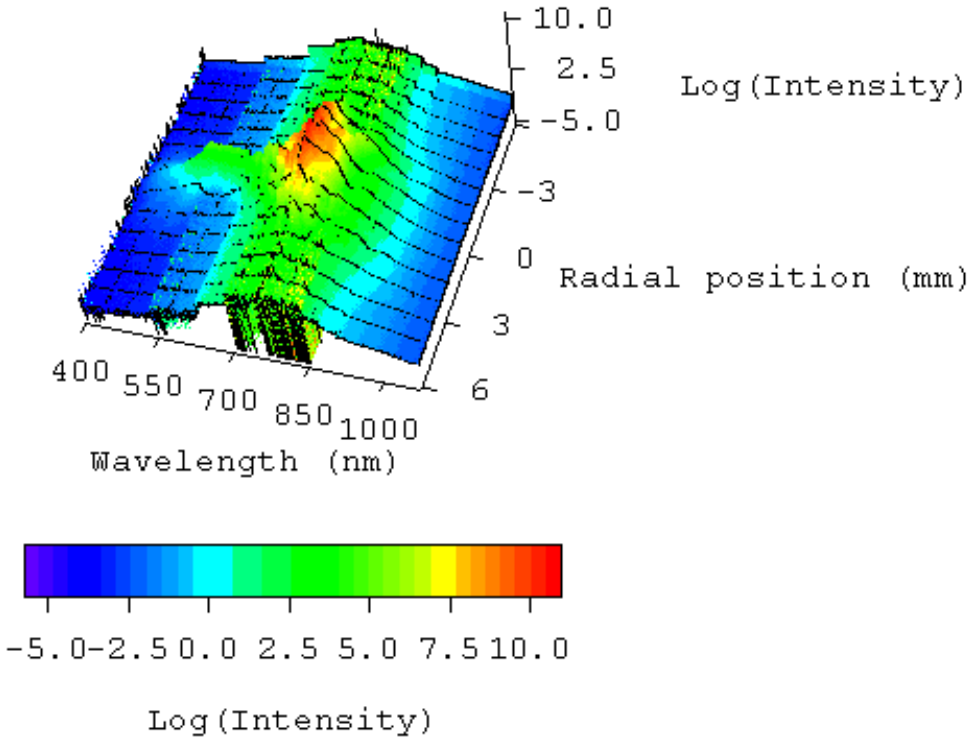

Figure 5.5: Spatial spectrum for an input power of 12 MW. Radial distance is plotted in mm and wavelength is plotted in nm.

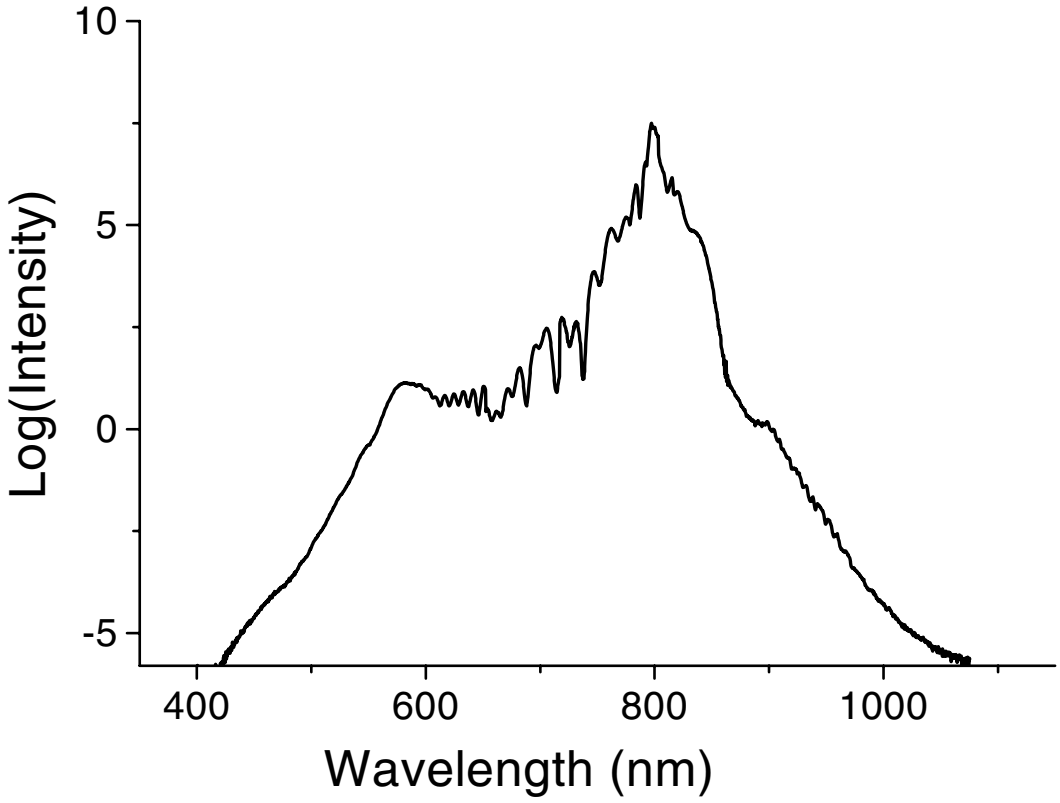

Figure 5.6: On axis spectrum corresponding to Fig. 5.5.

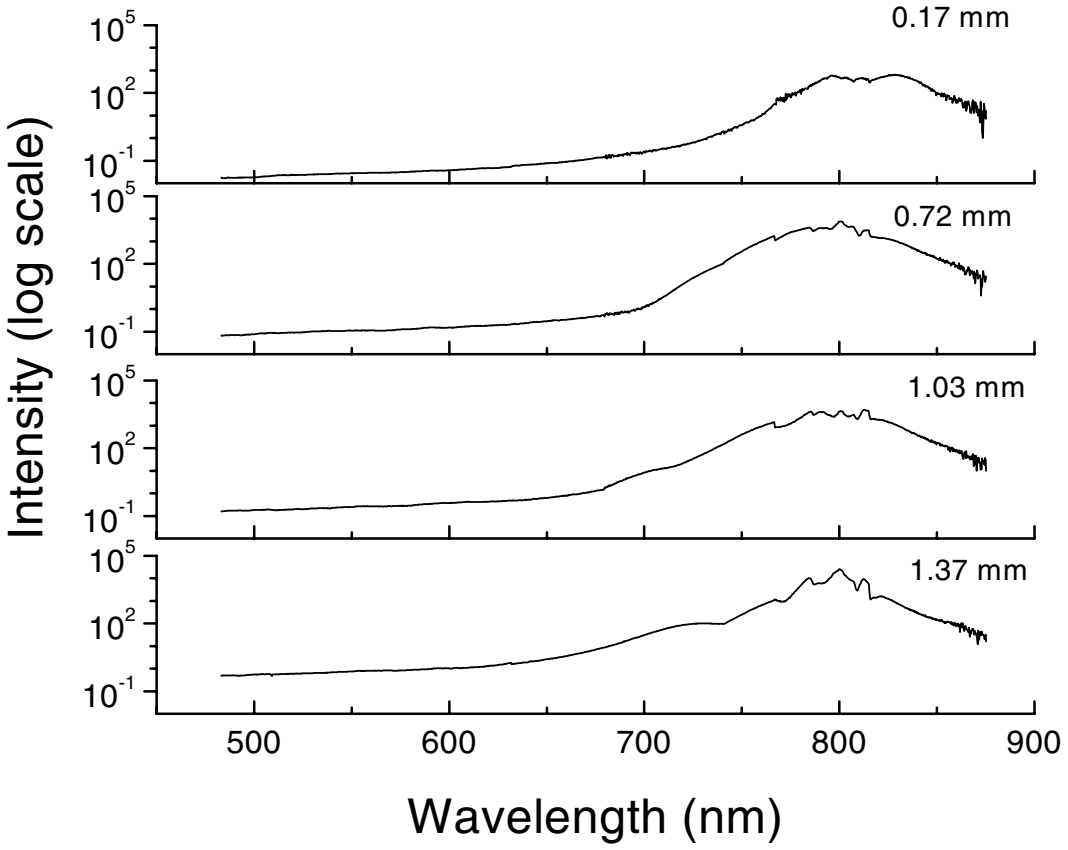

Figure 5.7: Lineouts of spectral intensity from a spatial-spectral measurement of continuum generated with an input power of 3.6 MW. The plot at 1.37 mm is the on-axis spectrum.

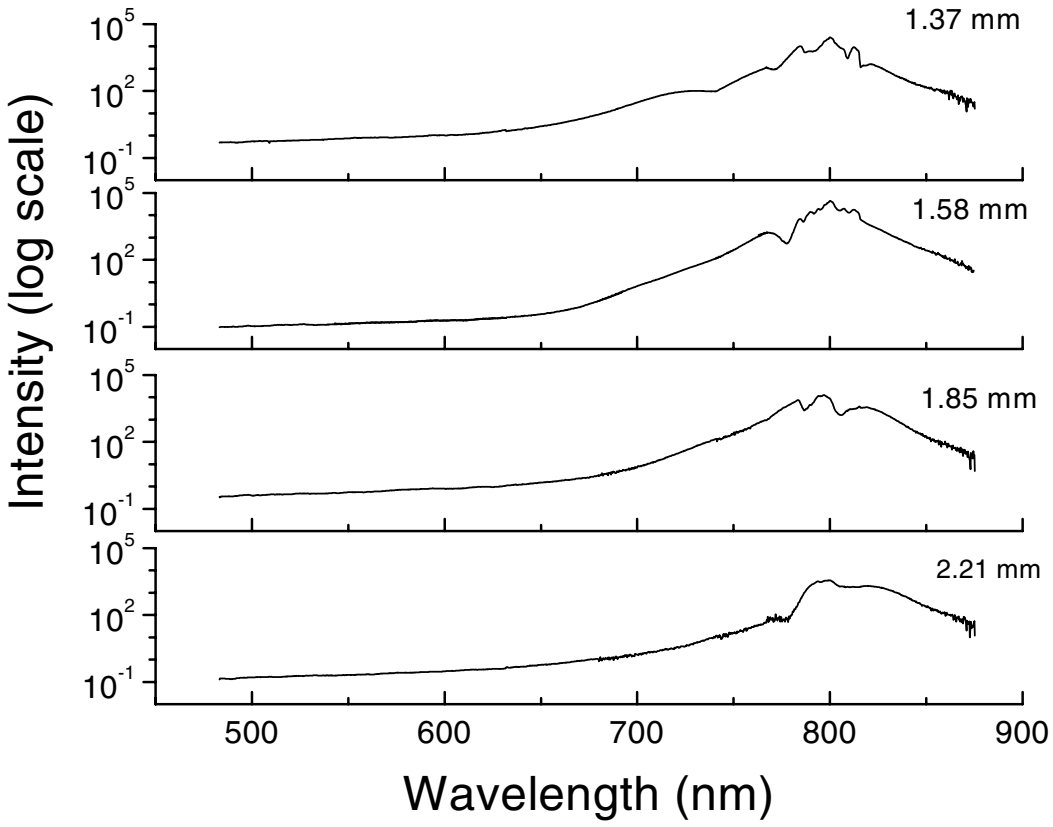

Figure 5.8: Lineouts of spectral intensity from a spatial-spectral measurement of continuum generated with an input power of 3.6 MW. The plot at 1.37 mm is the on-axis spectrum.

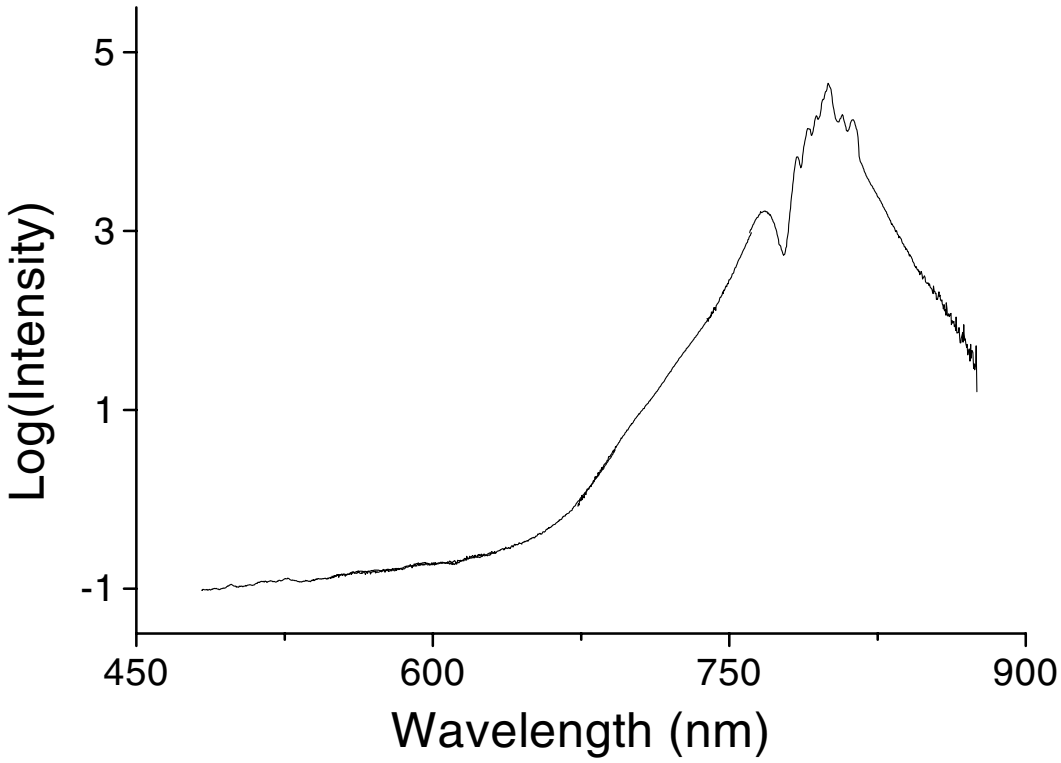

Figure 5.9: On-axis spectrum for an input power of 3.6 MW

5.2.5 Discussion

Preliminary on-axis calculations based on the (3+1)-D equation used to model pulse splitting with the inclusion of four-photon absorption are capable of reproducing some general features of the continuum [148]. For instance, the theory predicts asymmetric spectral broadening just as observed experimentally and predicts an extensively broadened spectrum with spectral wings extending from 400 nm to 1.4 microns. This theory also predicts a peak around 580 nm in the high input power case. The calculated peak, however, is only three orders of magnitude less than the peak intensity, while the measured peak is nearly six orders of magnitude less intense than the peak. As discussed previously, the inclusion of four photon absorption also predicts a loss of power during propagation that is comparable to the power loss we observe.

The theory of Chin and Brodeur also generally reproduces experimental observations. It predicts an asymmetric, very broad spectrum and accounts for the far-field ring structure as interference from continua generated from multiple broad-bandwidth sources. The theory is also based on multiphoton excitation which the power data presented here supports. Comparisons with experiment reveal, however, that although it predicts sufficient broadening, it also predicts a blue wing that is an order of magnitude more intense than that observed by experiment. In addition, the theory relies on a moving focus model of self-focusing that does not present a realistic representation of the self-trapped filaments. In fact, an experiment was performed in 1969 that demonstrates that filaments are indeed trapped and not a result of a moving focus [151]. In this experiment, self-trapped filaments were sent through an aperture such that if filaments actually existed, they would pass through unaffected. But if they were actually a result of a moving focus, they would be destroyed by diffraction. The filaments persisted after propagation through the aperture. The reverse experiment was also performed. The self-focused pulse was propagated through a glass film such that a filament would be de-

stroyed by diffraction, but the larger focusing beams would pass through and continue to focus. In this case, filaments were selectively destroyed. For this reason, a moving focus model is probably not the best representation to be used. Also, the moving focus model predicts the formation of short temporal sub-structures during propagation. One might argue that perhaps short temporal sub-structures are formed as a result of pulse splitting. The (3+1)-D NLSE used to model our pulse splitting experiments, however, never yields distinct multiple splittings in the near-field. Therefore, it is unlikely that the continuum is actually generated by short-duration sub-pulses. In addition, this theory relies on one-dimensional calculations even though self-focusing is involved. Since the transverse dimensions of the beam are being changed dramatically by the propagation, a three-dimensional calculation is clearly more appropriate.

The question remains: what are the necessary components of a reasonable theory for continuum generation? Because continuum generation occurs only above the critical power for self-focusing, the theory should account for changes to the spatial dimension of the beam during propagation. Based on the power measurements presented here, clearly a loss mechanism such as multiphoton absorption or excitation is important. The data here also emphasize that a damage mechanism should be considered. The work of Chin and Brodeur clearly indicates that multiphoton excitation has a probable role in the propagation. Their work also points out the dependence on bandgap that can be accounted for by MPE. Counter to the work of Chin and Brodeur, a successful theory should include, or at least not explicitly exclude, the formation of self-trapped filaments. The formation of self-trapped filaments also offers an explanation of the ring structure associated with continuum in similar fashion to the moving focus model. If continuum is generated all along the filament, the light generated at different points in the medium will interfere to give a ring structure. The ring structure may also be explained by including a saturable process in the theory. Ring formation as a result of saturation has been predicted by Marburger [114]. Theory should com-

pare not only to the on-axis spectrum, but to the entire spatial spectrum. Descriptions of the far-field spatial spectrum are available both in the literature and in this chapter. This chapter also provides the first measurement of the near-field spatial spectrum. In addition, a successful theory should include the dispersion of the material. Continuum spectra produced in gases have shown a modulation that was initially associated with all continuum spectra. Continuum spectra in glass that do not exhibit this modulation have typically been explained as resulting from multiple shot experiments where the spectral modulation would be averaged out. I believe, however, that continuum spectra in glass do not show a strong modulation because the various spectral components are dispersed by GVD.

Although the processes involved in continuum generation cannot fully be explained at this time, some of the main issues involved have been elucidated. The observations presented here should provide a useful comparison for developing theories. Understanding continuum generation remains an interesting and important unsolved problem.

Chapter 6

One-Dimensional Propagation in Liquids

It is well known that the additional degrees of freedom of constituent molecules in a liquid compared to molecules in a solid lead to more complicated interactions between the liquid and an electromagnetic field. Propagation of an intense beam through a liquid can result not only in the instantaneous optical Kerr effect, but in molecular reorientation, molecular redistribution, and Raman excitations of rotation and libration as well [124, 152]. Molecular reorientation is a rotation of a molecule to reduce the energy of the system in response to a field induced dipole moment of that molecule. Molecular reorientation typically occurs on a timescale of 10^{-11} s [124]. Molecular redistribution is also a response of the material to a field induced dipole moment and involves the local rearrangement of molecules in the field to minimize the energy of induced dipole-induced dipole interactions between molecules. This rearrangement has a response time in the sub-picosecond range [124]. The response times for rotation and libration are typically on the order of 100 fs. Electrostriction, which is an increase in the density of a material due to the presence of an applied field, typically has a response time of approximately 100 ns in liquids [124]. Most all of these processes involve a response time that is longer than the duration of our 80-100 fs pulses. Rotation and libration respond on a timescale that is very close to the duration of our pulses. Because of these long response times, none of these processes should lead to an observable effect in our experiments. We expect, therefore, to observe the same processes involved

in propagation of short pulses in liquids as were observed in propagation through fused silica in one dimension, namely the electronic Kerr effect and group velocity dispersion.

Interestingly, however, Nibbering *et al.* have reported a non-instantaneous nonlinear response in methanol with a response time of 27 fs [94]. Their experiment involves propagation of $804\ \mathrm{nm}$, $24\ \mathrm{mJ}$, $150\ \mathrm{fs}$ pulses through a known reference material and an unknown sample. The spectrum before and after each propagation is measured. Spectral changes upon propagation through the reference material yield the initial pulse intensity. The initial pulse intensity is then used with the second spectral measurement to determine the nonlinear index of refraction of the unknown sample. Nibbering asserts that this measurement is evidence that the optical Kerr effect in methanol is dominated by a nuclear rather than a purely electronic term. Their work assumes that the non-instantaneous response can be modeled by a single-sided exponential:

$$n(t) = \int_{-\infty}^{t} \frac{n_2 I(t')}{\tau} \exp\left(-\frac{t-t'}{\tau}\right) dt'. \tag{6.1}$$

This chapter investigates the propagation of $\sim 80 - 120\ \mathrm{fs}$ pulses in two liquids: methanol and water. Methanol is studied with the purpose of repeating Nibbering's measurement using a different technique and thereby confirming or disproving the reported non-instantaneous nonlinearity. Water is investigated for two reasons. Propagation issues involved in sending short pulses through water, particularly the nonlinear index of refraction of liquid water, is of considerable interest in the biological sciences. Short pulse lasers are finding application in research involving the human body, especially with regard to surgical techniques [153, 154, 155]. In addition, water is studied because it is a hydrogen-bonded, polar liquid composed of relatively small molecules and, as such, is suitable for testing for systematic errors in the measurement. To wit, if both liquids show the same non-instantaneous response, the integrity of the measurement technique can be questioned. If the experiments in water reveal a purely instantaneous response, however, while the experiments in methanol do not, then it is

likely that the non-instantaneous nonlinearity is real and not merely an artifact of the measurement technique.

6.1 Methanol Studies

6.1.1 Stationary Cell Measurements

Experiment

Pulses from the compressor stage of the laser system described in Chapter 3 propagate unfocused to the sample. The unfocused beam propagates approximately as a plane wave in the sample, with a diameter of 5 mm (FWHM). The energy per pulse of 227 μJ corresponds to a peak power of 2.6 GW. Because of the high energy of the pulses, the beam is not spatially filtered. Plane-wave propagation within the sample is verified explicitly by measuring the beam size before and after propagation through the sample. To within the experimental error due to the pixel size of the CCD camera, the beam size is unchanged. The spectroscopic grade methanol sample is placed in a 1 cm path length Starna spectrophotometer cuvette. Propagation through only the two 1-mm-thick cell walls of the empty cuvette is found to have negligible effect on the pulse at this intensity.

An interesting problem arises in attempting to perform FROG measurements with this experimental set up. When methanol is added to the cuvette, the beam acquires a dynamic spatial modulation after propagation. If one observes the liquid sample with a flashlight in a dark room, one can see a convective-type current in the liquid and small dust-sized particles moving in a circular pattern. Repeated cleaning of the cuvette makes no difference in this behavior. If the sample is allowed to sit undisturbed for ~ 24 hours, however, the liquid becomes calm, and the beam passes through with no observable spatial modulation. All data presented in this chapter were acquired after

a minimum 24 hour wait period.

Data

Figure 6.1 shows the measured intensity and phase of a pulse prior to and after propagation through the methanol sample. The input field is shown in (a) and the field after propagation is shown in (b). In both graphs, the solid line represents the intensity, and the points represent the phase. The upward curvature of the phase in (a) is evidence of an initially slightly downchirped input. After propagation through the methanol, the pulse is noticeably upchirped as a result of the positive group velocity dispersion and the positive nonlinear index of refraction n_2. In addition, the peak of the phase curvature has been shifted slightly toward the trailing edge of the pulse.

Model and Results

Since conditions have been chosen such that the pulse propagates through the sample as a plane wave, the propagation can be modeled using a (1+1)-dimensional nonlinear Schrödinger equation:

$$\frac{\partial \mathcal{E}}{\partial z} + i\frac{k''}{2}\frac{\partial^2 \mathcal{E}}{\partial t^2} - i\frac{2\pi n_2}{\lambda}|\mathcal{E}|^2\mathcal{E} = 0. \tag{6.2}$$

The second term of this equation accounts for group velocity dispersion, and the third term gives the instantaneous nonlinearity. The measured input field shown in Fig. 6.1(a) is used as an initial condition of this model, with k'' = 290 fs^2/cm [156] and $n_2 = 4 \times 10^{-16}$ cm^2/W. The propagated field is then calculated using a split-step technique [107, 129] and is shown in Fig. 6.2(a) along with the measured field for comparison. The calculated intensity and phase are given by the dashed line and the crosses, respectively. The simulation was performed using a range of different n_2 values around those found in the literature [94, 157], and no significant difference in the fit was observed. As illustrated by this example, the simple model, including reasonable values for the material parameters and an instantaneous response time for the nonlinearity,

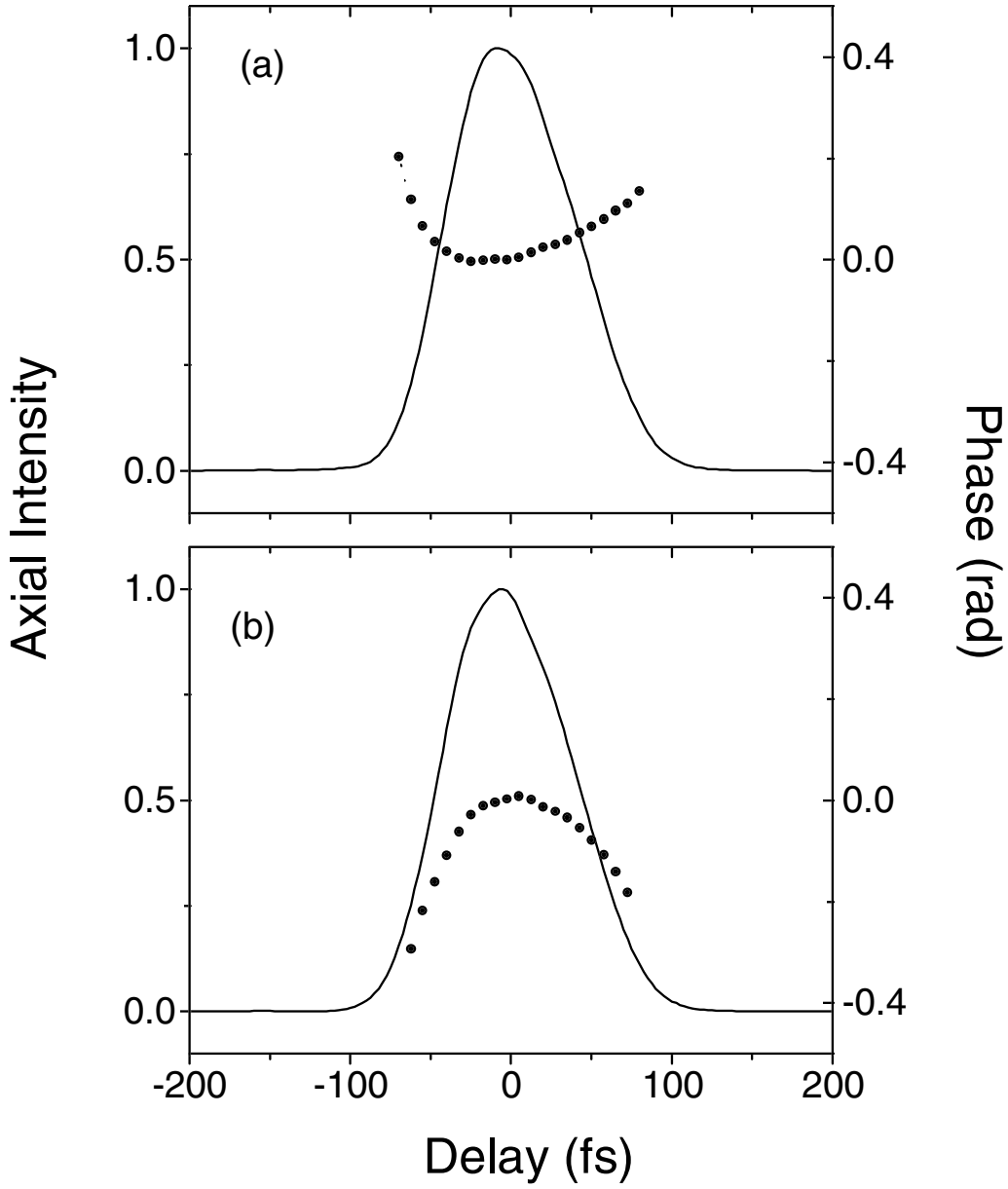

Figure 6.1: Intensity (solid lines) and phase (points) of a pulse both (a) prior to and (b) after propagation through a 1-cm sample of methanol.

fails to match the experimentally measured phase, especially the shift in the phase to later times.

This shortcoming in the model can be corrected by phenomenologically including a non-instantaneous response of the nonlinearity such that the term

$$n_2|\mathcal{E}|^2$$

in Eq. (2) is replaced by [114]

$$\int_{-\infty}^{t} \frac{n_2|\mathcal{E}(t')|^2}{\tau} \exp(-\frac{t-t'}{\tau})dt' \tag{6.3}$$

where τ is the exponential response time of the nonlinearity. Equation 6.3 is the same representation of the non-instantaneous nonlinearity used by Nibbering *et al* [94].

Figure 6.2(b) shows the results of the model including the non-instantaneous response term of Eq. 6.3 with τ = 10 fs. The measured input field of Fig. 6.1(a) was again used as an initial condition of the model. Inclusion of the non-instantaneous response correctly predicts the observed shifting of the peak of the phase toward the trailing edge of the pulse. The calculated phase best matches the experimentally determined phase when values of $n_2 = 4 \times 10^{-16}$ cm^2/W and $\tau = 10$ fs are used.

An interesting feature of the data in Fig. 6.2 is the extremely small value of the exponential response time τ. As mentioned previously, response times for electrostriction, molecular reorientation, molecular redistribution, and molecular librations are all too slow to explain the observed non-instantaneous nonlinearity. As seen in the one-dimensional experiments with fused silica presented in Chapter 4, vibrational Raman does not come into play unless much higher intensities (and therefore larger pulse bandwidths due to self-phase modulation) are used. Thermal effects occur on very long timescales relative to the length of our pulses. Because a single FROG measurement requires approximately five minutes to acquire and the repetition rate of the laser is 1 kHz, it is possible that thermal effects could appear in these stationary cell measurements. Nibbering's work does not mention the sample conditions. To determine

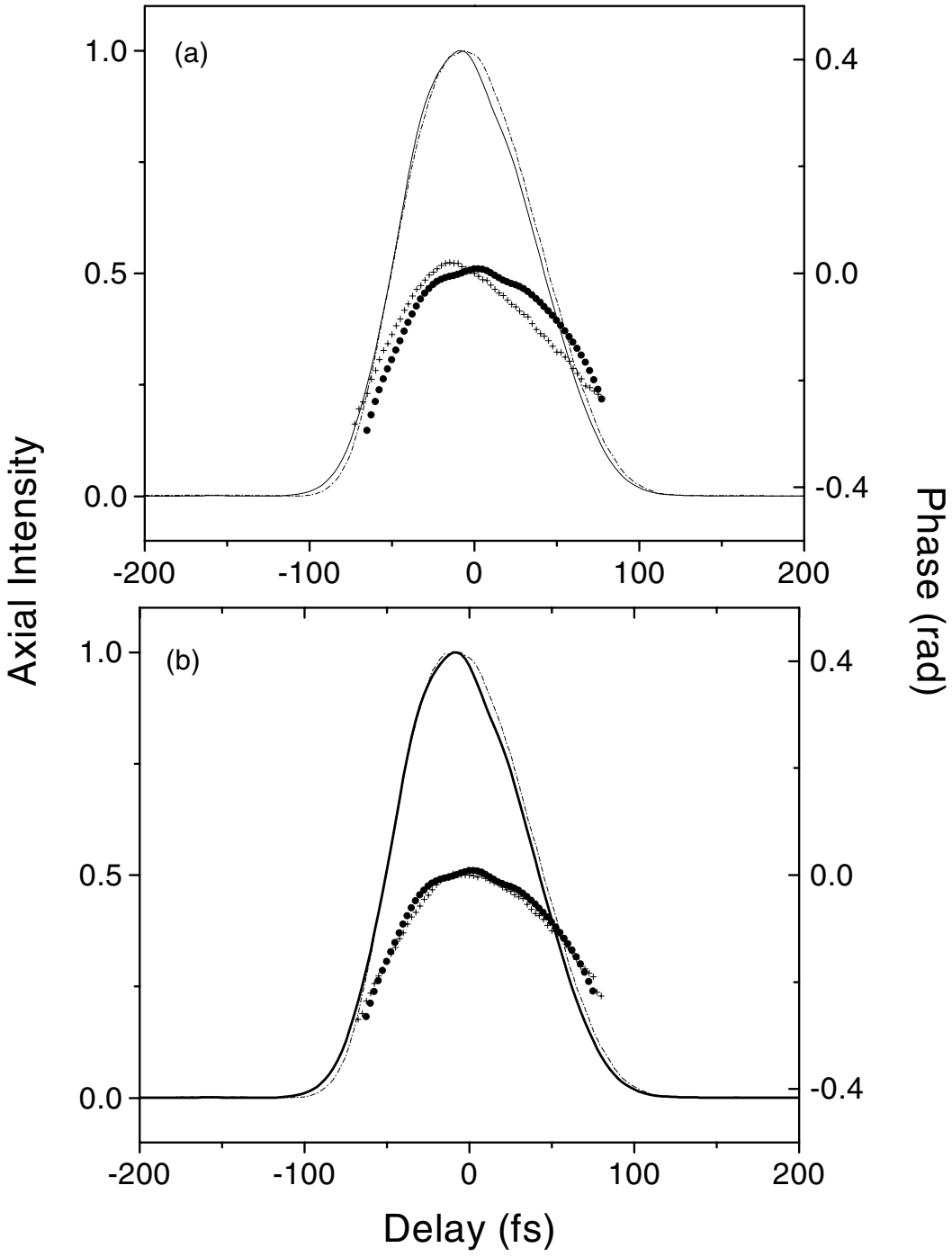

Figure 6.2: Calculated field after propagation (a) assuming an instantaneous nonlinearity and (b) with inclusion of a non-instantaneous nonlinearity. The calculated intensity is plotted as a dashed line and the calculated phase is plotted as crosses. The calculated fields are shown along with the measured field (solid line and points) for comparison.

whether the observed response is indeed a result of the nonlinear index of refraction changing during the measurement, we also performed measurements using a flowing methanol apparatus.

6.1.2 Flowing Methanol Measurements

Experiment

For these experiments, a dye cell and pump from a dye laser were used to flow the sample. A new dye cell was used to ensure that there was no contamination from an optically active dye. The path length through the sample was 1.69 cm, and the thickness of the cell walls was 2 mm. In addition, a vacuum spatial filter was inserted into the beam path before the sample cell to improve the spatial quality of the beam. Peak input powers ranged between 4.5 and 5.5 GW. Again, all experiments were performed in the plane wave regime. It is also important to note that all of the data in the remainder of this chapter were acquired under sub-optimal laboratory conditions. The building temperature fluctuated over a range of seven degrees Celsius from day to night, greatly affecting laser performance and stability. As a result, all FROG traces were acquired in duplicate and only data from those traces that were repeatable are presented here. Careful observation of the beam with PG FROG was also used to monitor changes in laser behavior. In this way, if the laser changed between the measurement of two repeatable reference traces and two repeatable sample traces, the data were also discarded.

Data

Figure 6.3 shows the intensity and phase of the input field and the field after propagation through 1.69 cm of methanol. The input pulse has an intensity FWHM of 120 fs and has a nearly flat phase with a small component of upchirp. After propagation, the pulse is broadened in time and is significantly upchirped as is evidenced by the

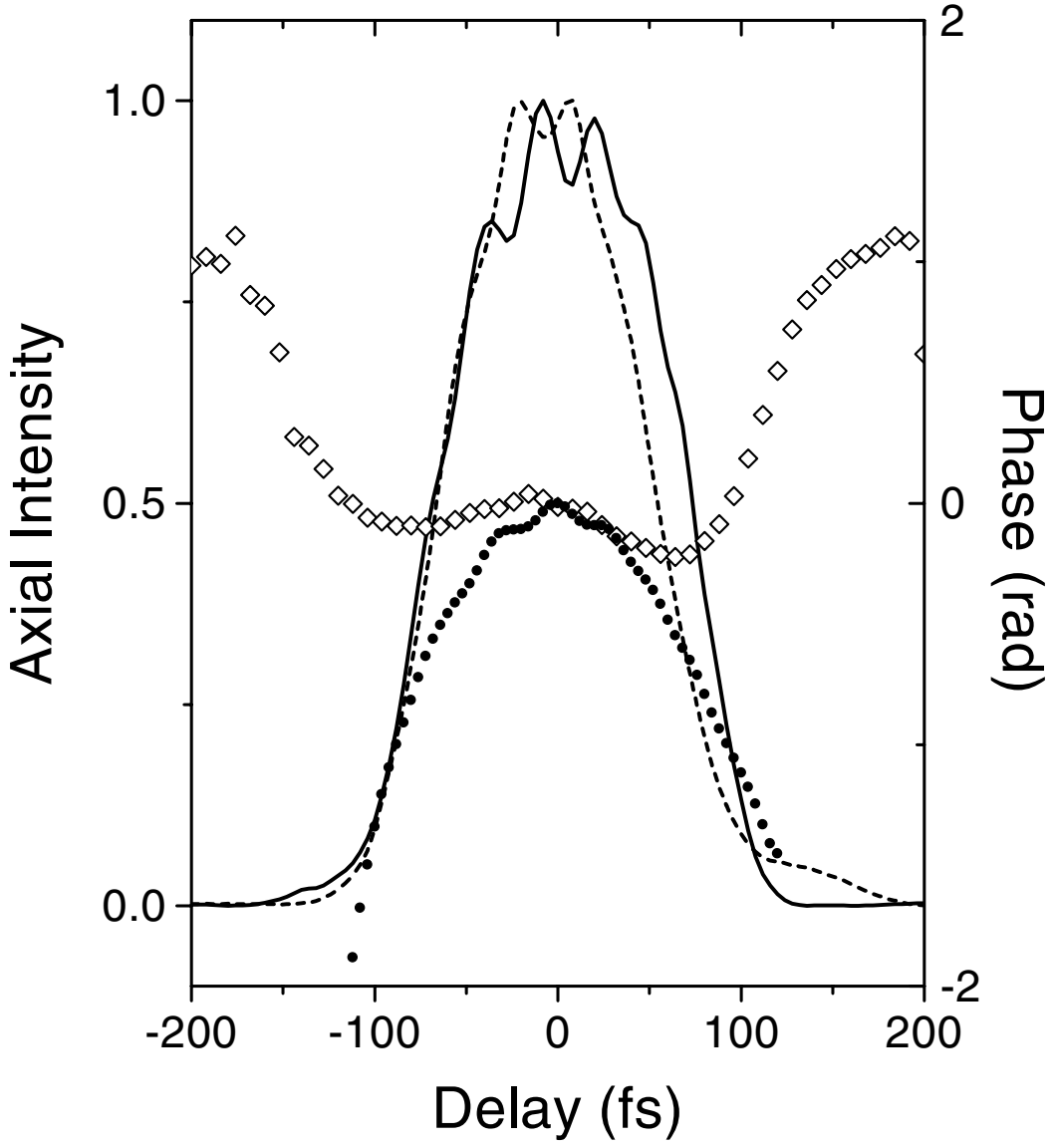

Figure 6.3: Measured intensity and phase of the pulse before (dashed line and diamonds) and after (solid line and points) traversing 1.69 cm of methanol.

downward curvature of the phase. These features are a result of the interplay between SPM with positive n_2 and positive dispersion. A shift in the phase toward the trailing edge of the pulse is difficult to discern by eye.

The corresponding spectra before and after propagation through the methanol sample are shown in Fig. 6.4. After propagation through the methanol, a red-shift of energy in the spectrum is observed. This spectral red-shifting is indicative of a non-instantaneous nonlinearity.

Propagation with a very upchirped input pulse was also investigated. For this data, the input power was increased such that the peak intensity was roughly the same as for the shorter, flat-phase pulse. This experiment thus tests for any dependence of the non-instantaneous nonlinearity on the chirp or length of the pulse. The temporal duration of the very chirped input pulse differs from that of the nearly flat-phase input pulse by 12 fs. The phase of the very chirped input pulse changes by approximately six radians from the center of the pulse to the point where the intensity has dropped to $1/e^2$ of the peak intensity. The most obvious effect of the propagation is a significant broadening of the pulse. Thirty-five femtoseconds more pulse broadening is observed with this upchirped input than with the nearly flat-phase input of Fig 6.3. This extra broadening is the result of an upchirped input pulse providing a head start to the propagation-induced upchirp that results from SPM with positive n_2 and positive GVD.

Model and Results

The flowing methanol data are modeled using the same equations as the stationary cell data. The cell walls in this case are approximately twice as thick (2 mm) as the walls of the stationary cell. Including propagation through the cell walls in the calculation has an observable effect on the calculated spectra. Therefore, all calculations are performed assuming propagation first through 2 mm of fused silica with values of

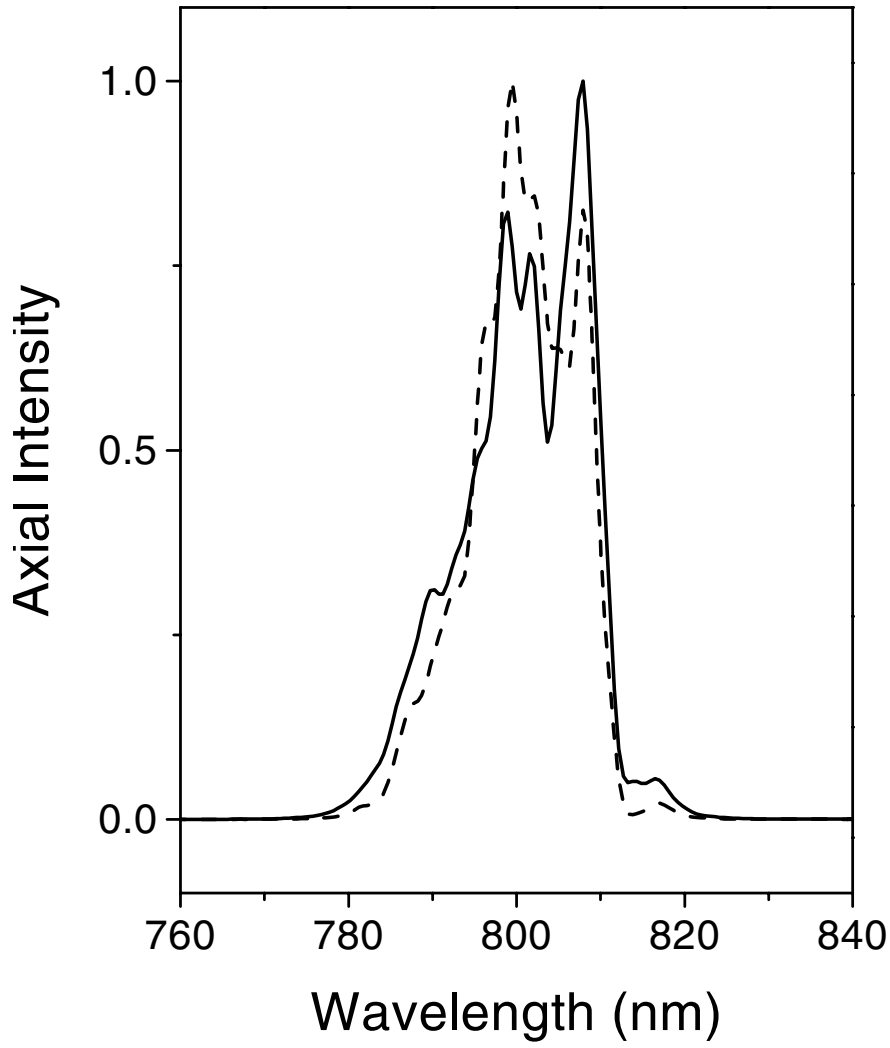

Figure 6.4: Measured spectra before (dashed line) and after (solid line) propagation through 1.69 cm of methanol.

$n_2 = 2.5 \times 10^{-16}$ cm^2/W and $k'' = 360$ fs^2/cm and assuming an instantaneous response. The field is then propagated numerically through the methanol sample using $k'' = 290\ \mathrm{fs}^2/\mathrm{cm}$, assuming a non-instantaneous nonlinearity as given by Eq. 6.3 and varying the values of n_2 and τ. Finally, the field is propagated through the second 2 mm wall of fused silica.

Calculations using the measured input field from Fig. 6.3 are in best agreement with the temporal broadening of the measured field after propagation when a value of $n_2 = 4 \times 10^{-16}$ cm^2/W is used. Figure 6.5 shows the measured intensity and phase along with calculated results using this value of n_2 and three different values of τ. If the nonlinearity is assumed to be purely instantaneous ($\tau = 0$), the calculated phase does not match well on the leading or trailing edges of the pulse. On the other hand, when τ is assumed to be 27 fs (the value determined by Nibbering *et al.*), the calculated phase is shifted too far toward the trailing edge of the pulse. The best match between the model and experiment is found when a value of τ = 10 fs is used. To further illustrate this point, the differences between the measured and calculated phases for these three values of τ are plotted in Fig. 6.6. The phase difference in the case of τ = 10 fs always falls between the phase differences in the other two cases, and is on average closer to zero. The small scale modulation in the measured phase is not reproduced by the calculations and results in the modulations seen in all three of the phase difference curves. Performing calculations on a much finer grid might reproduce these modulations. Currently, the largest number of points in the field array that the model can handle is 512.

A comparison between the measured spectrum after propagation (shown in Fig. 6.4) and the calculated spectrum corresponding to the case of τ = 10 fs (Fig. 6.5) is shown in Fig. 6.7. The measured and calculated spectra are in good agreement. The calculation reproduces the observed shifting of energy to the red spectral components.

Calculations involving the very upchirped input pulse also show good agreement

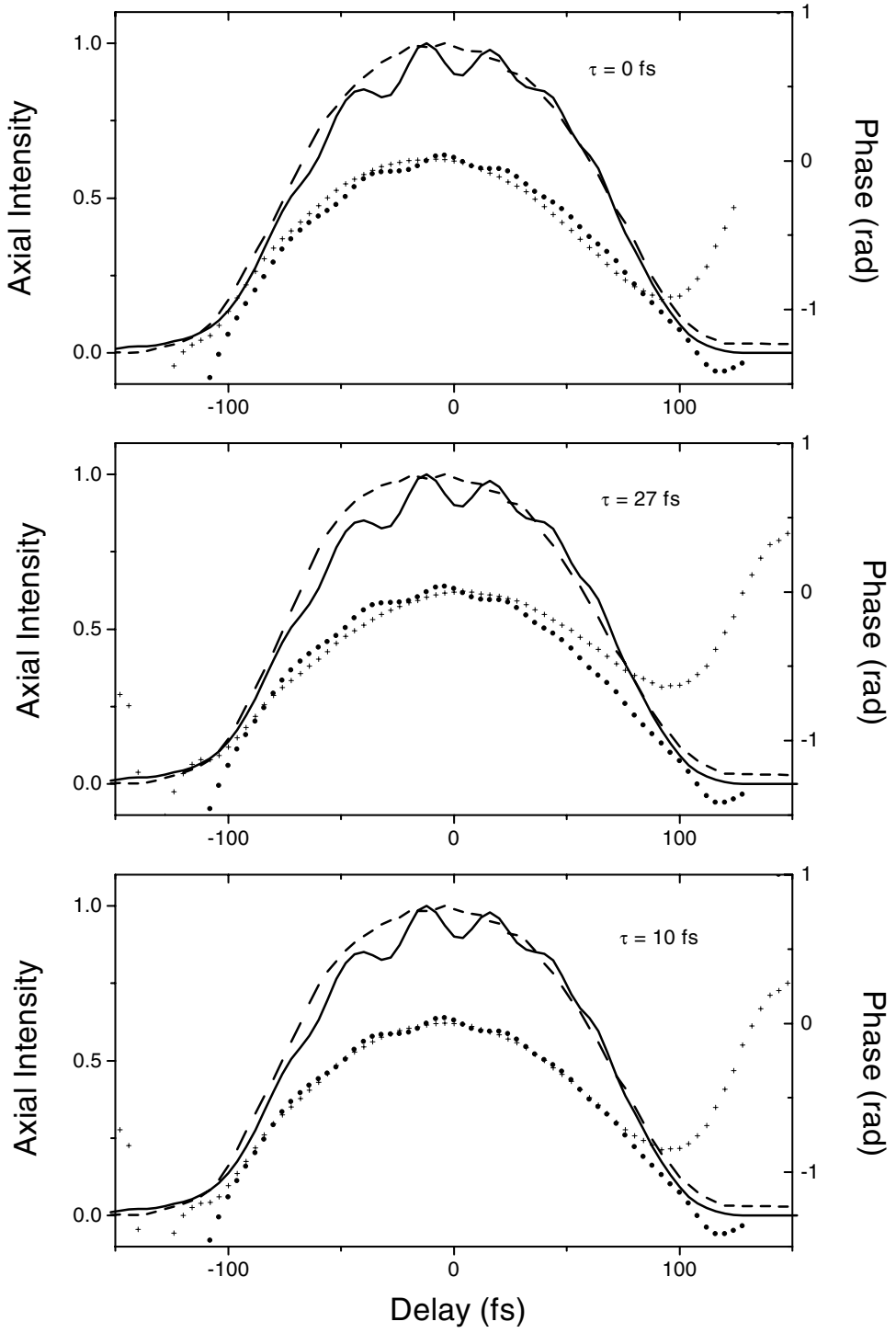

Figure 6.5: Measured intensity (solid line) and phase (points) along with calculated intensity (dashed line) and phase (crosses) using the input field from Fig. 6.3 with n_2 = 4×10^{-16} cm^2/W for three different values of τ.

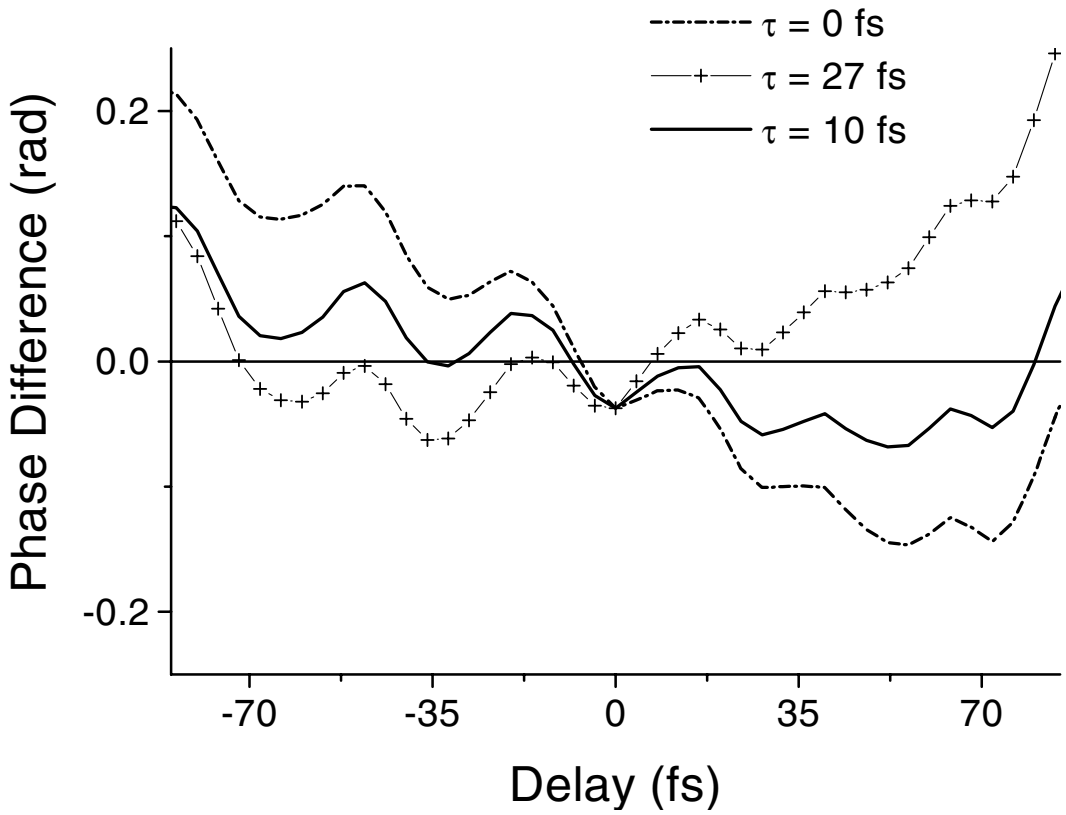

Figure 6.6: The difference between measured and calculated phase for the three calculations presented in Fig. 6.5: $\tau = 0$ fs (dots and dashes), $\tau = 10$ fs (solid line) and $\tau = 27$ fs (line with crosses).

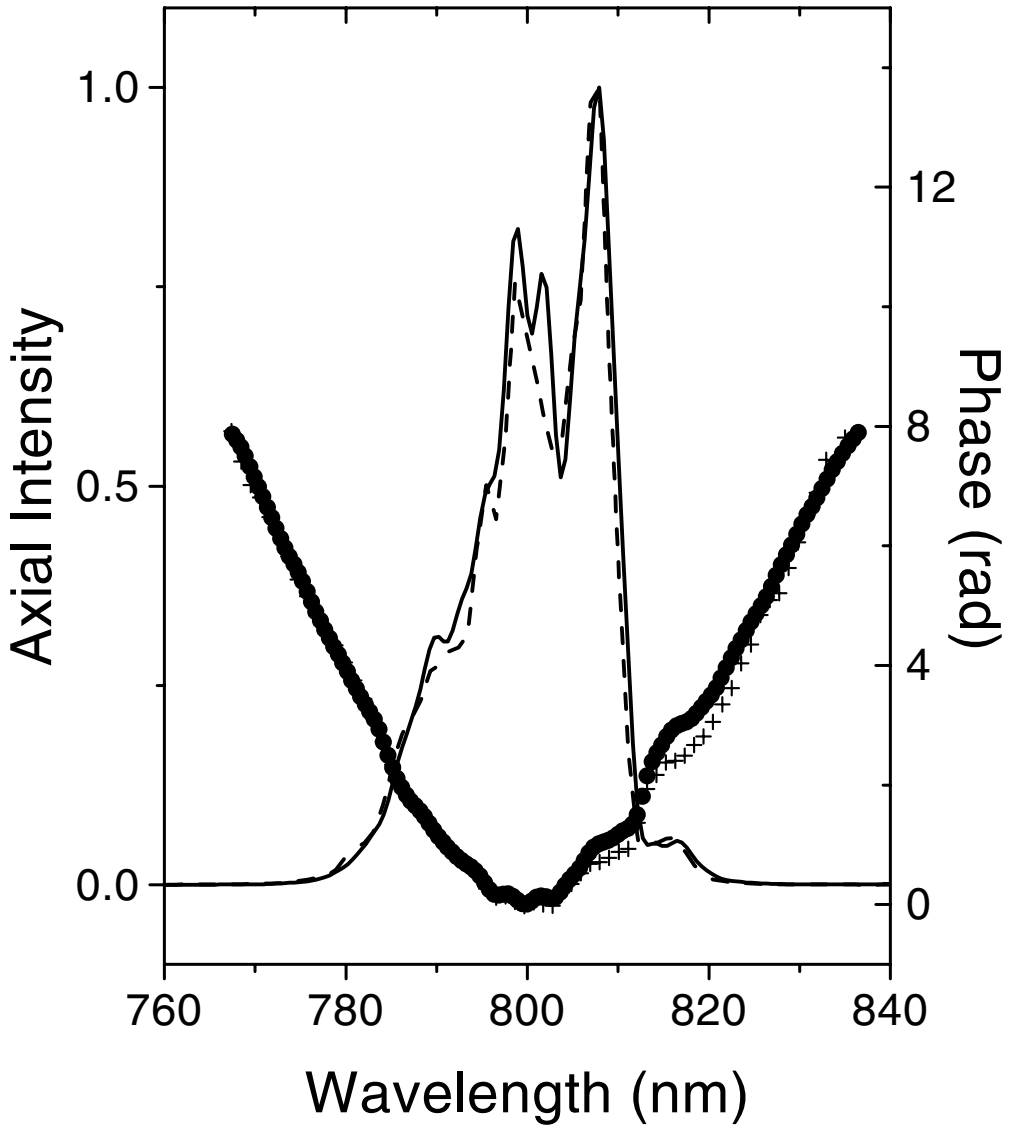

Figure 6.7: Measured spectral intensity and phase (solid line and points) along with calculated spectral intensity and phase (dashed line and crosses) for the case of n_2 = 4×10^{-16} cm^2/W and $\tau = 10$ fs.

with experiment when values of $n_2 = 4 \times 10^{-16}$ cm^2/W and $\tau = 10$ fs are used in the model. The phase in this case is so strongly curved, however, that the effects of differing values of τ are difficult to distinguish. Therefore, any dependence of the non-instantaneous nonlinearity on the chirp of the pulse is difficult to extract. Moreover, it is best to use a flat-phase input pulse in experiments to determine the value n_2 and τ.

6.1.3 Discussion

The data presented in the previous two sections clearly indicate the presence of a non-instantaneous nonlinearity in methanol. Experiments with a flowing methanol configuration rule out the possibility that heating effects are contributing to the measured nonlinearity. In all cases, we observe values of n_2 and τ that are smaller than those reported by Nibbering *et al.* [94]. To demonstrate that our numbers are clearly different from those measured by Nibbering, a plot of our data with a calculation using Nibbering's numbers is shown in Fig. 6.8. The calculated field is very different from the measured field in this case.

There are several questions that should be addressed. The first is the difference in the measured values reported in these two investigations. The model used to calculate the nonlinear response is the same in both cases. The two main differences in the approaches are the experimental method used and the length of the input pulses. Nibbering's work involves propagating 150 fs pulses through the sample. Since these pulses are longer, it is possible that they measure contributions to the nonlinear index from libration and rotation (response time of 100 fs) that the shorter pulses used in our experiment do not detect. It is also possible that there is a systematic error in one or both of the measurement techniques that results in the differing magnitudes of the propagation parameters. Another possibile difference lies in the method of measuring the input intensity. A small change in the input intensity results in a noticeable change in the magnitude of the nonlinear index of refraction. Therefore an incorrectly cali-

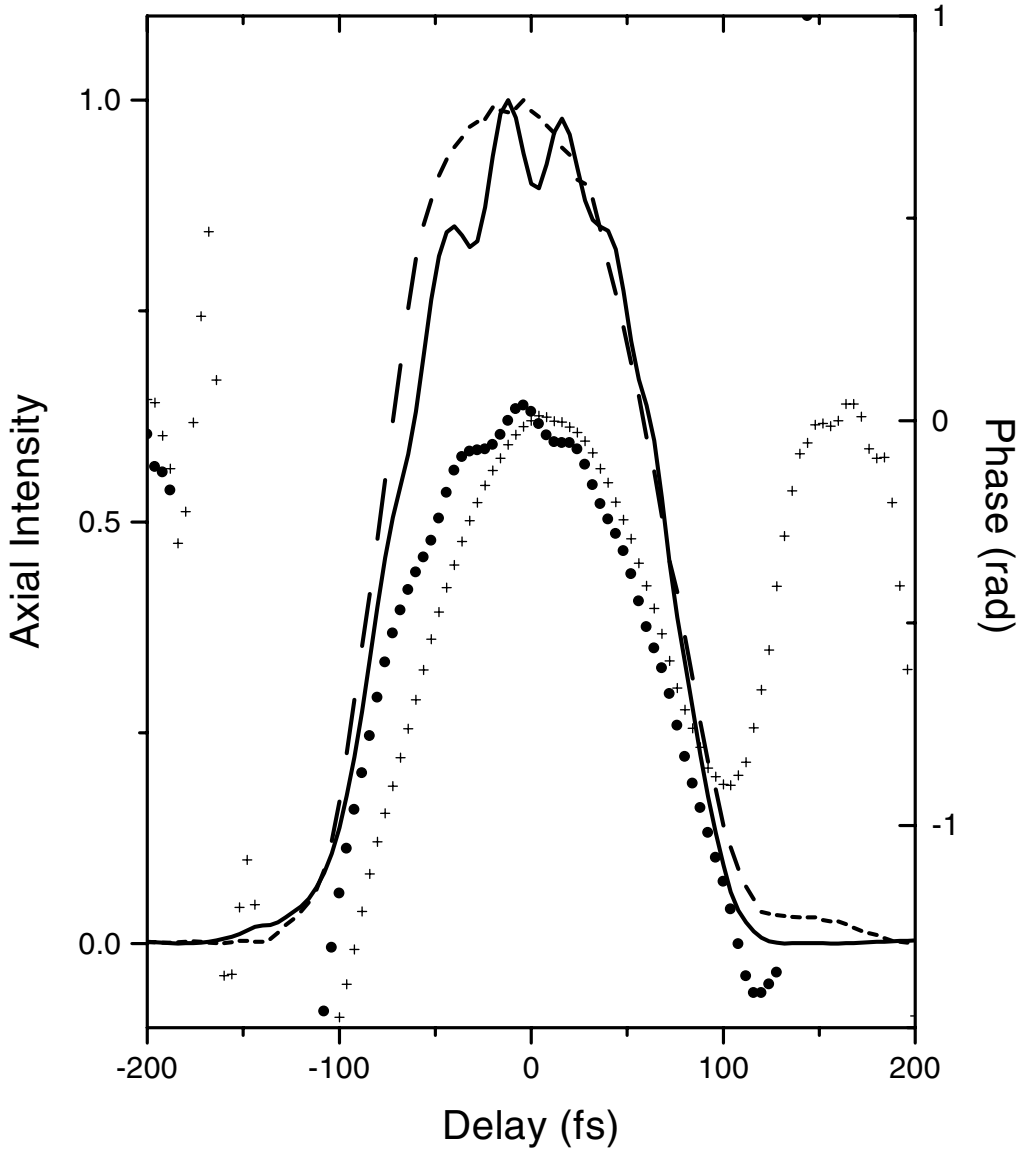

Figure 6.8: Measured intensity and phase (solid line and points) with calculated intensity and phase (dashed line and crosses) using Nibbering's reported values: n_2 = 6.7×10^{-16} cm^2/W and $\tau = 27$ fs.

brated power meter, or an inaccurate assessment of input pulse duration, could lead to the differences in the measured values of n_2.

A second question that remains is the nature of the non-instantaneous nonlinearity. Most effects involving nuclear or molecular motion respond on timescales much longer than 10 fs. If this effect is real, one may ask whether it is possible that the cause is not actually something that occurs with a 10 fs response time, but simply results in a phase profile that has similar characteristics. The model is one used to describe any diffusive retardation in the medium and is not necessarily representative of the true nature of the process or processes involved. The presence of one- or two-photon absorptions affecting the nonlinear index is ruled out by the UV-Vis absorption spectrum of methanol which is flat between 850 nm and 205 nm. In addition, two-photon absorption is typically accompanied by a flattening of the peak of the intensity profile after propagation [158], a feature that is not observed in our data. Also, measurements of power throughput reveal losses due only to reflection.

A third question surrounding the observed effect is whether it could be an artifact of the measurement techniques used. To partially respond to this question, we perform experiments in water using the same techniques. Water is chosen because like methanol, it is a small, polar liquid that is hydrogen bonded and has a flat UV-Vis absorption spectrum down to 190 nm.

6.2 Water Studies

Water measurements are performed using the flowing liquid apparatus described in Section 6.1.2. Peak input powers are always near 5 GW, and the pulses propagate as plane waves through the sample. The stability criteria are again used to select which data sets to analyze. Calculations are performed taking into account propagation through the cell walls. Fisher HPLC-grade water is used as the sample.

This work		Previous work		
n_2 (10^{-16} cm^2/W)	# data sets	n_2 (10^{-16} cm^2/W)	wavelength	Ref.
1.8	2	2.8	694 nm	[159]
3.0	1	4.2	532 nm	[160]
4.5	3	5.4	532 nm	[159]
		5.7	804 nm	[94]

Table 6.1: Measured and literature values of n_2 for water.

6.2.1 Data and Results

Figure 6.9 shows the measured intensity and phase before and after propagation through 1.69 cm of water. The input pulse has an initial upchirp that leads to enhanced broadening of the pulse. After propagation, the pulse is more upchirped and shows no shifting of the phase toward the trailing edge of the pulse.

Calculations are performed using the measured input field and a value of k'' = 247 $\mathrm{fs}^2/\mathrm{cm}$ [156]. For all acquired data, the best fit is obtained when only an instantaneous nonlinearity is included. A comparison of the calculated and measured fields after propagation for the data shown in Fig. 6.9 is plotted in Fig. 6.10. The calculated intensity and phase matches the measurement quite well. For this calculation, $n_2 = 1.8 \times 10^{-16}$ cm^2/W. The fact that no non-instantaneous nonlinearity is present in water indicates that the nonlinearity observed for methanol is not likely an artifact of the measurement technique.

The value of n_2 was determined for several data sets by using n_2 as a fit parameter in calculating the measured field. Three different values were obtained, with an average value of 3.4 ± 0.4 cm^2/W accounting for random error only. In all cases the agreement between the measured and calculated fields were comparable to that shown in Fig. 6.10. Table 6.1 shows our measured values along with some values from the literature. Beside each measured value is the number of data sets that gave that result. Our measured values are somewhat lower than the only other published value near 800 nm [94]. The

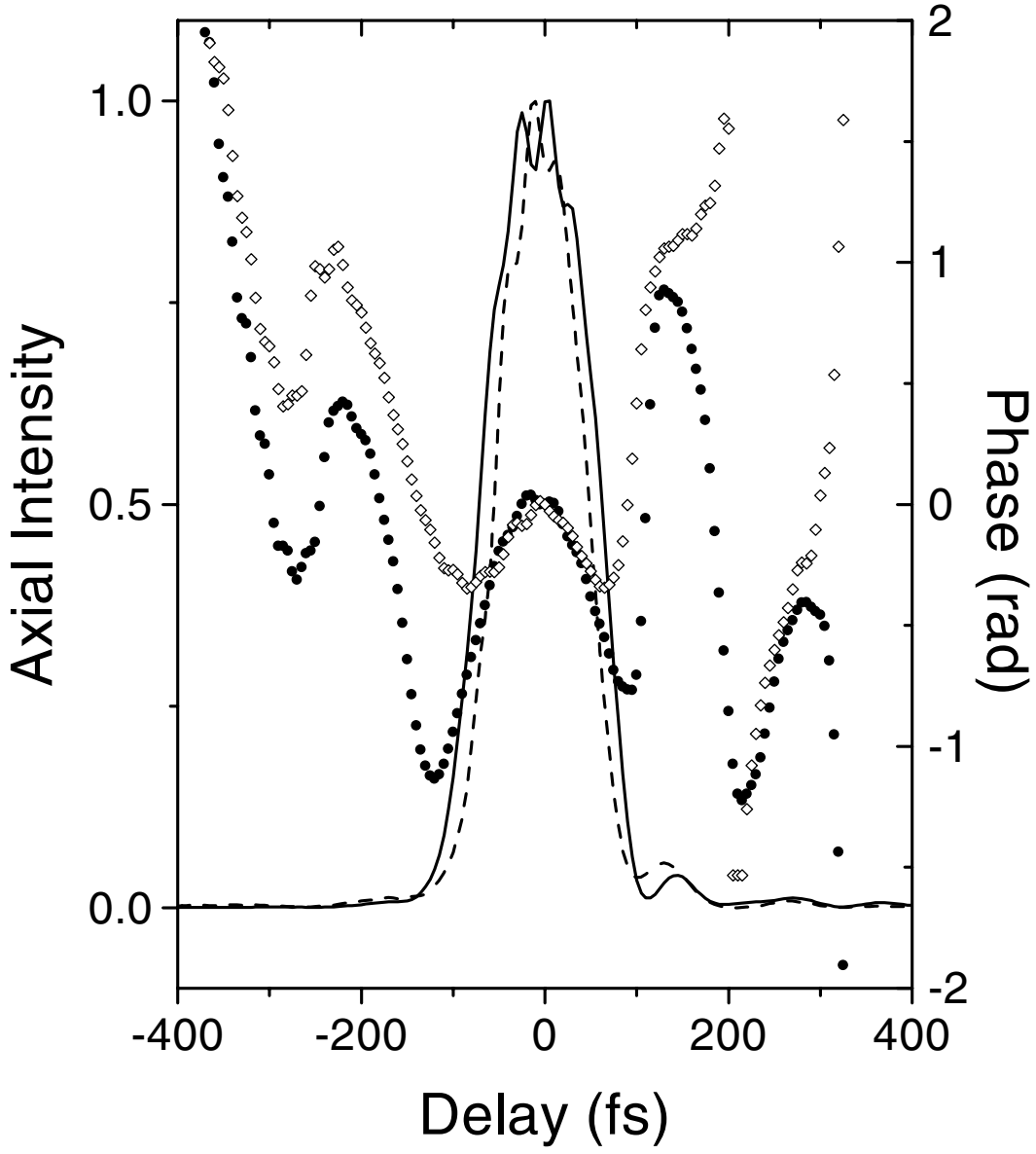

Figure 6.9: Measured intensity and phase prior to (dashed line and diamonds) and after (solid line and points) propagation through 1.69 cm of water.

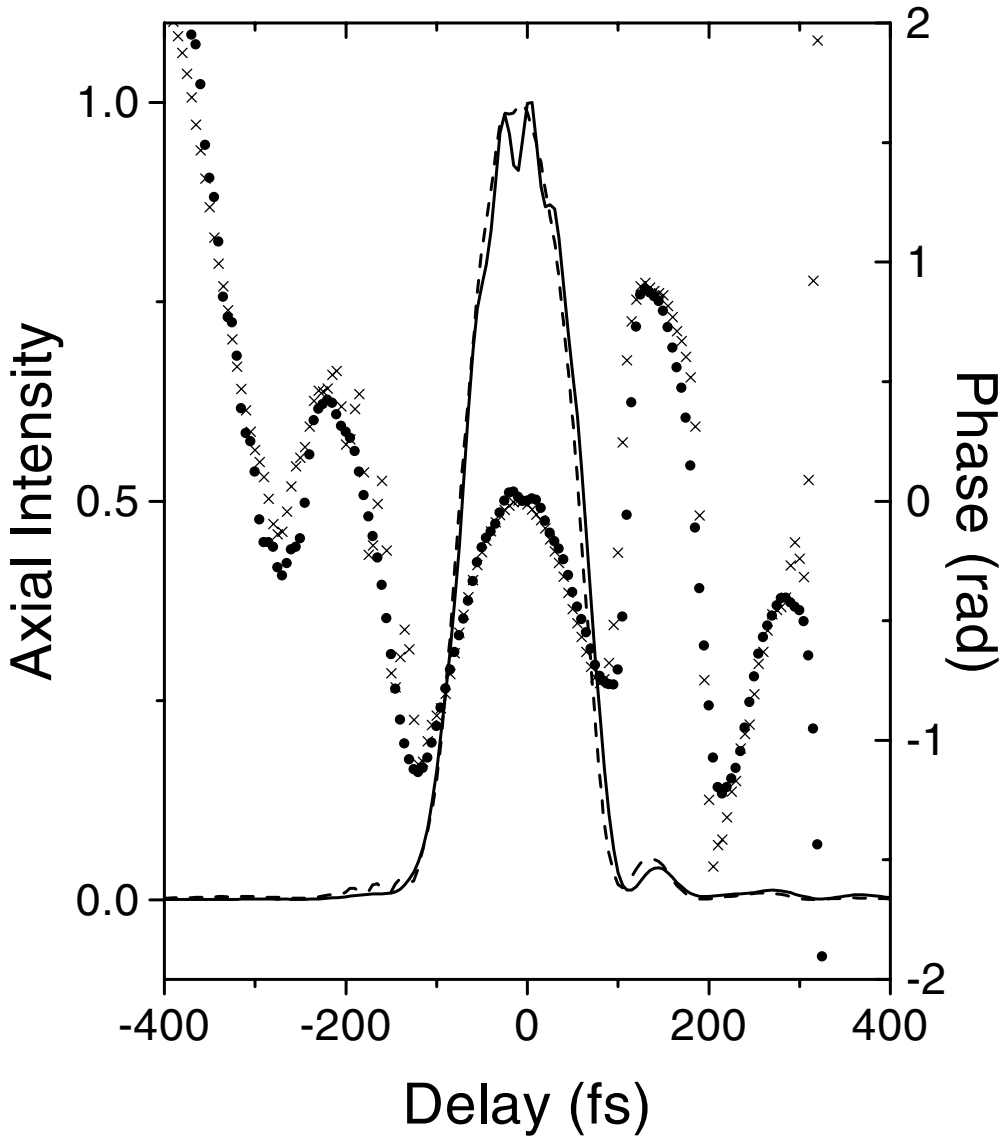

Figure 6.10: Measured (solid line and points) and calculated (dashed line and crosses) intensity and phase after propagation through 1.69 cm of water. The calculation assumes a purely instantaneous nonlinearity.

spread in the values of n_2 given by different data sets is larger than we would ideally like it to be. There are several possible explanations for this. One problem may involve accurate measurement of the intensity. Measurement of the peak intensity is based on accurate knowledge of the area of the input pulse (see Chapter 3). If the area of the input pulse changes between measurement of the input pulse and measurement of the pulse after propagation through the sample, the intensity, and hence n_2, will be incorrect. With the unstable room conditions present during these measurements, it is conceivable that small scale or very slow changes could have occurred without causing the data to fail the stability requirements. Also, during these water measurements a problem arose with the temperature servo on the baseplate of the regenerative amplifier. The temperature of the baseplate fluctuated over several degrees Celsius during the course of an hour. Fluctuations in the temperature of the amplifier baseplate affect laser performance and could contribute to the observed inconsistencies in the data. One could also argue that the observed differences are an inherent limit of the measurement technique. Previous FROG data presented in this thesis gives much more repeatable results, however. It is more likely a problem of accurate measurement of the intensity of an unstable laser.

6.3 Summary

The experiments in this chapter corroborate the existence of a non-instantaneous nonlinearity with a very short response time in methanol. The value of this response time is found to be 10 fs, roughly three times shorter than the previous measurement reported [94]. Experiments conducted with a flowing methanol apparatus eliminate the possibility that the observed nonlinearity is actually a heating effect. The shorter pulses used in these experiments also cast doubt on the mechanism being driven by librational motion. Experiments in water, which show a purely instantaneous nonlinearity, confirm that the measured non-instantaneous nonlinearity in methanol is probably real.

Measurements of power throughput, observations of the temporal intensity of the pulse after propagation, and observations of the UV-Vis absorption spectrum of methanol all indicate that there is no evidence for absorption occuring during propagation. The actual mechanism responsible for the observed non-instantaneous nonlinearity remains undetermined.

Attempts to measure the nonlinear index of refraction of water using this technique gave results with low precision. The results, however, are in agreement with other values published in the literature. And, under more stable conditions, this would likely be a reasonable method of measuring the nonlnear index of refraction.

Chapter 7

Summary

Understanding the propagation of short pulses in a variety of media is of great importance to a number of applications spanning many fields of interest. By applying a full-field measurement technique to the study of short pulse propagation in several interesting materials and regimes, this work lends insight into the complicated combination of linear and nonlinear processes involved. This work also demonstrates the second-harmonic generation (SHG) form of frequency-resolved optical gating (FROG) as a powerful technique for resolving complicated propagation issues in the field of ultrafast science.

Experiments involving plane-wave propagation in fused silica reveal surprisingly large changes in temporal pulse width over relatively short propagation distances. These experiments show a broadening that is nearly 20 times larger than that predicted by group velocity dispersion (GVD) alone. These experiments, along with calculations based on a one-dimensional nonlinear Schrödinger equation (NLSE), illustrate that the effects of GVD and self-phase modulation (SPM) are interrelated and should not be treated separately as is commonly seen in the literature. This thesis presents the first full-field measurements detailing this interplay between GVD and SPM. The very good agreement between the experiment and the model validates FROG as a valuable technique for investigating short pulse propagation.

Propagation is also studied in a regime where conditions are such that the pulse

undergoes self-focusing. Self-focusing leads to much higher intensities and associated higher-order nonlinear effects that result in temporal pulse splitting. At lower input powers, a pulse splits into two sub-pulses, each shorter in duration than the parent pulse. With increasing input powers, multiple sub-pulses are observed. The overall phase across the entire split field indicates upchirp, with the leading pulse shifted to the red of the trailing pulse in frequency. The phase of the input pulse is also found to affect the propagation. An upchirped input gives a head-start to the propagation induced upchirp and results in split pulses that are broader in both the spectral and temporal domains. A downchirped input pulse, on the other hand, tends to offset the propagation induced upchirp and results in split pulses that are significantly narrower in both the temporal and spectral domains.

In this three-dimensional propagation regime, transverse changes to the beam can no longer be neglected, and the model must take into account propagation-induced spatial changes to the beam. A simple three-dimensional model based on the NLSE, however, is not sufficient to describe the observed pulse splitting. The observed splitting exhibits asymmetry in both intensity and phase that the simple model cannot reproduce. Observation of these asymmetries led to the development of a model including the effects of a Raman nonlinearity, linear and nonlinear shock, and third-order dispersion. The Raman nonlinearity preferentially amplifies red-shifted frequencies within the pulse and, with GVD, enhances the leading pulse of the split pair. Both linear and nonlinear shock enhance the trailing pulse during the pulse-splitting process. The very short-temporal duration trailing pulse then diffracts faster than the leading pulse and thus appears less intense at the exit face of the sample. The effects of the Raman nonlinearity are not sufficient to completely offset the effects of shock in the material, however it does temper them. Third-order dispersion also contributes to a larger leading pulse by increasing the dispersion of the blue components. It is, however, a smaller magnitude effect and plays a lesser role in determining the symmetry of the split pulses

than either Raman or shock. The paraxial assumption is still valid with this level of self-focusing.

This modified NLSE predicts asymmetric pulse splitting, however, it does not predict the multiply-split pulses observed in the experiment. In order to explain the multiple splittings, we have found that we must take into account propagation to the far-field. In fact, we have found that multiple splittings like those observed in experiment only occur in the far-field. These multiple pulses do not arise from subsequent splitting of the original split field, but rather result from a build-up of phase in the far-field. In general, pulse splitting occurs first in the far-field and then proceeds to the near-field. When fully split pulses are resolved in the near-field, the far-field is multiply-split. The modified NLSE including propagation to the far-field is in excellent agreement with the experiment at 800 nm for all of the peak input powers investigated.

We have also investigated propagation at higher powers where a continuum spectrum is generated. Continuum spectra have been used in parametric amplification, short pulse generation, and time-resolved spectroscopy and show potential for use in many evolving applications. Our studies near the power threshold for continuum generation indicate that the split temporal field begins to coalesce with the production of more spectral components. Above the threshold for continuum generation, full-field FROG measurements are no longer practical. In this regime, we present observations of continuum behavior as a function of both input power and elapsed time. The overall loss of power during the continuum generation process is an indication that multi-photon absorption occurs in the sample. The dependence of the continuum and power losses on the elapsed time indicates the presence of a saturable process and probable material damage. This thesis also presents the first near-field spatial-spectral measurements of the continuum spectrum. Comparisons with the model used in the pulse splitting experiments, modified to include four-photon absorption, reveal spectral asymmetries and initial power losses similar to those observed in the experiment. This theory, however,

is still not adequate to describe all aspects of the experimental data. These results uncover several of the basic processes involved in the generation of spectral continua and should provide a useful comparison for further theoretical development.

Propagation in liquid samples is also investigated in a one-dimensional propagation regime with the goal of providing a measurement of the nonlinear index of refraction. These measurements are of interest because an accurate determination of the nonlinear index is of particular importance in forecasting propagation effects. Measurements were performed in both methanol, a common organic solvent, and water which is of interest to medical and biological sciences. We find that full-field measurement techniques are ideally suited to these kinds of measurements, assuming one takes into account group velocity dispersion and limits the propagation to the plane-wave regime. Studies in methanol reveal contributions to the nonlinear index of refraction by a non-instantaneous nonlinearity with a surprisingly short response time of 10 fs. The exact mechanism responsible for this non-instantaneous nonlinearity is unknown. Electrostriction, molecular reorientation, molecular redistribution, rotation and libration should all occur on timescales longer than 10 fs and are therefore not responsible for the observed nonlinear response. The nonlinear index of refraction of water, on the other hand, results purely from the instantaneous electronic response. The nonlinear index of refraction of water is found to be in good agreement with previous literature values. Measurements in water thus validate both the observed non-instantaneous nonlinearity in methanol and the measurement technique.

The studies in this thesis elucidate important aspects of linear and nonlinear propagation under a variety of conditions. The science presented here is not only interesting from a fundamental standpoint, but it should also find applicability in a wide variety of fields. This work emphasizes the advantages of using a full-field measurement technique for investigating short pulse propagation and demonstrates the suitability of the SHG form of FROG for this purpose. These studies also exemplify the mutually ben-

eficial relationship that is possible between experiment and theory. These studies lend insight into several interesting and complicated short pulse propagation related issues and should have a bearing on other endeavors involving short, high-intensity pulses.

Of course, the experiments presented here suggest many opportunities for future investigations, some of which include measurements of the full spatial field of a propagating pulse, three-dimensional propagation in liquids, and studies of pulse splitting in materials that do not produce continuum. As discussed in Chapter 4, the pulse splitting experiments involve the spatial aspects of the field during propagation. It would thus be interesting to measure not only the on-axis field as we have done, but also to include a measure of spatial intensity and phase during propagation as well. A means of accomplishing this measurement is the technique of spectral interferometry.

Spectral interferometry consists of interfering an unknown pulse with a known reference pulse and recording the entire interferogram with a CCD [161, 40, 162]. A few requirements in spectral interferometry are as follows; there must exist a coherent phase relationship between the two pulses, the spectrum of the reference pulse must be greater than that of the pulse to be measured, and the reference pulse must be fully characterized. The reference pulse can be characterized using FROG. A single laser beam can be split to give both of the pulses thus ensuring a coherent phase relationship. The second pulse becomes "unknown" by traversing the sample of interest. In short pulse propagation, however, one must be careful either to limit the effects of self phase modulation in the sample or to spectrally broaden the reference pulse via SPM prior to its interaction with the unknown pulse to ensure that the second requirement is satisfied. The full field, including one spatial dimension, of the unknown pulse can be retrieved from the spectral interferogram.

We have performed spectral interferometry in a linear propagation regime and have accurately recovered the value of dispersion of BK-7 glass along the entire spatial dimension of the beam. We have also performed one preliminary experiment involving

nonlinear propagation and were able to observe the expected spatially dependent nonlinear index of refraction. If one could accurately determine the full field of a continuum reference pulse, spectral interferometry could be an invaluable tool for gathering much-needed information about the spatial phase of a pulse during continuum generation.

It would also be interesting to study three-dimensional propagation in liquids. We know empirically and from the literature that a continuum is generated in water. But, do the extra degrees of freedom afforded a liquid affect the continuum generation process? And if so, in what way? And, what effect does local boiling have on the observed continuum?

Investigating the literature tells us that the band gap of the material plays a role in determining the spectral broadening observed in continuum generation. There exist materials with a band gap that is too small for continuum to be generated [135]. It would be interesting to investigate pulse splitting in these materials at input peak powers above that where multiple splitting is first observed. In the absence of spectral superbroadening, it is improbable that the same pulse coalescence would be observed. Another experiment would also be interesting to perform. In materials with the smallest possible band gap above the threshold for continuum generation, where continuum would occur at lower input powers, a situation might arise where pulse-splitting never occurs. By investigating these extreme cases, one could potentially learn more about the processes involved.

In any case, propagation of short pulses should continue to present many fascinating and challenging problems to scientists for years to come.

Bibliography

[1] L. E. Hargrove, R. L. Fork, and M. A. Pollack, "Locking of He-Ne laser modes induced by synchronous intracavity modulation," Appl. Phys. Lett. **5,** 4–5 (1964).

[2] R. L. Fork, C. H. Brito Cruz, P. C. Becker, and C. V. Shank, "Compression of optical pulses to six femtoseconds by using cubic phase compensation," Opt. Lett. **12,** 483–485 (1987).

[3] J. Zhou, J. Peatross, M. M. Murnane, H. C. Kapteyn, and I. P. Christov, "Enhanced high-harmonic generation using 25 fs laser pulses," Phys. Rev. Lett. **76,** 752–755 (1996).

[4] J.-C. Diels, J. J. Fontaine, I. C. McMichael, and F. Simoni, "Control and measurement of ultrashort pulse shapes (in amplitude and phase) with femtosecond accuracy," Appl. Opt. **24,** 1270–1282 (1985).

[5] P. W. Milonni and J. H. Eberly, Lasers (John Wiley and Sons, Inc., New York, 1988).

[6] A. Yariv, Optical Electronics (Saunders College Publishing, Philadelphia, 1991).

[7] R. W. Boyd, Nonlinear Optics (Academic Press, San Diego, 1992).

[8] J. R. de Oliveira, M. A. de Moura, J. M. Hickmann, and A. S. L. Gomes, "Self-steepening of optical pulses in dispersive media," J. Opt. Soc. Am. B **9,** 2025–2027 (1992).

[9] D. J. Bradley and G. H. C. New, "Ultrashort pulse measurements," Proc. IEEE **62,** 313–345 (1974).

[10] E. B. Treacy, "Measurement and interpretation of dynamic spectrograms of picosecond light pulses," J. Appl. Phys. **42,** 3848–3858 (1971).

[11] J. Jansky and G. Corradi, "Full intensity profile analysis of ultrashort laser pulses using four-wave mixing or third harmonic generation," Optics Commun. **60,** 251–256 (1986).

[12] N. G. Paulter, Jr. and A. K. Majumdar, "A new triple correlator design for the measurement of ultrashort laser pulses," Optics Commun. **81,** 95–100 (1991).

[13] H.-S. Albrecht, P. Heist, J. Kleinschmidt, D. Van Lap, and T. Schröder, "Single-shot measurement of femtosecond pulses using the optical Kerr effect," Meas. Sci. Technol. **4,** 492–495 (1993).

[14] A. S. L. Gomes, V. L. da Silva, and J. R. Taylor, "Direct measurement of non-linear frequency chirp of Raman radiation in single mode optical fibers using a spectral window method," J. Opt. Soc. Am. B **5,** 373–379 (1988).

[15] R. Trebino, C. C. Hayden, A. M. Johnson, W. M. Simpson, and A. M. Levine, "Chirp and self-phase modulation in induced-grating autocorrelation measurements of ultrashort pulses," Opt. Lett. **15,** 1079–1081 (1990).

[16] G. Szabó, A. Müller, and Z. Bor, "A single shot method to determine duration and chirp of ultrashort pulses with a streak camera," Optics Commun. **82,** 56–62 (1991).

[17] T. F. Albrecht, K. Seibert, and H. Kurz, "Chirp measurement of large-bandwidth femtosecond optical pulses using two-photon absorption," Optics Commun. **84,** 223–227 (1991).

[18] S. P. Le Blanc and R. Sauerbrey, "Ultrashort pulse characterization using plasma-induced cross-phase modulation," Optics Commun. **111,** 297–302 (1994).

[19] K. Naganuma, K. Mogi, and H. Yamada, "General method for ultrashort light pulse chirp measurement," IEEE J. Quantum Electron. **25,** 1225–1233 (1989).

[20] K. Naganuma, K. Mogi, and H. Yamada, "Time direction determination of asymmetric ultrashort optical pulses from second-harmonic generation autocorrelation signals," Appl. Phys. Lett. **54,** 1201–1202 (1989).

[21] J. E. Rothenberg and D. Grischkowsky, "Measurement of optical phase with subpicosecond resolution by time domain interferometry," Opt. Lett. **12,** 99–101 (1987).

[22] C. Yan and J.-C. Diels, "Amplitude and phase recording of ultrashort pulses," J. Opt Soc. Am. B **8,** 1259–1263 (1991).

[23] E. B. Treacy, "Direct demonstration of picosecond-pulse frequency sweep," Appl. Phys. Lett. **17,** 14–16 (1970).

[24] E. P. Ippen and C. V. Shank, "Dynamic spectroscopy and subpicosecond pulse compression," Appl. Phys. Lett **27,** 488–490 (1975).

[25] E. B. Treacy, "Optical pulse compression with diffraction gratings," IEEE J. Quantum Electron. **QE-5,** 454–458 (1969).

[26] W. H. Knox, R. L. Fork, M. C. Downer, R. H. Stolen, C. V. Shank, and J. A. Valdmanis, "Optical pulse compression to 8 fs at a 5-kHz repetition rate," Appl. Phys. Lett **46,** 1120–1121 (1985).

[27] J. A. Chilla and O. E. Martinez, "Direct determination of the amplitude and the phase of femtosecond light pulses," Opt. Lett. **16,** 39–41 (1991).

[28] J. A. Chilla and O. E. Martinez, "Frequency domain phase measurement of ultrashort light pulses. Effect of noise," Optics Commun. **89,** 434–440 (1992).

[29] J.-P. Foing, J.-P. Likforman, M. Joffre, and A. Migus, "Femtosecond pulse phase measurement by spectrally resolved up-conversion: Application to continuum compression," IEEE J. Quantum Electron. **28,** 2285–2290 (1992).

[30] J. Paye, "The chronocyclic representation of ultrashort light pulses," IEEE J. Quantum Electron. **28,** 2262–2273 (1992).

[31] D. J. Kane and R. Trebino, "Characterization of arbitrary femtosecond pulses using frequency-resolved optical gating," IEEE J. Quantum Electron. **29,** 571–579 (1993).

[32] K. C. Chu, J. P. Heritage, R. S. Grant, K. X. Liu, A. Dienes, W. E. White, and A. Sullivan, "Direct measurement of the spectral phase of femtosecond pulses," Opt. Lett. **20,** 904–906 (1995).

[33] A. M. Weiner, J. P. Heritage, and E. M. Kirschner, "High-resolution femtosecond pulse shaping," J. Opt. Soc. Am. B **5,** 1563–1572 (1988).

[34] A. Sullivan, W. E. White, K. C. Chu, J. P. Heritage, K. W. Delong, and R. Trebino, "Quantitative investigation of optical phase-measuring techniques for ultrashort pulse lasers," J. Opt. Soc. Am. B **13,** 1965–1978 (1996).

[35] K. C. Chu, J. P. Heritage, R. S. Grant, and W. E. White, "Temporal interferometric measurement of femtosecond spectral phase," Opt. Lett. **21,** 1842–1844 (1996).

[36] J.-K. Rhee, T. S. Sosnowski, A.-C. Tien, and T. B. Norris, "Real-time dispersion analyzer of femtosecond laser pulses with use of a spectrally and temporally resolved upconversion technique," J. Opt. Soc. Am. B **13,** 1780–1785 (1996).

[37] V. Wong and I. A. Walmsley, "Ultrashort-pulse characterization from dynamic spectrograms by iterative phase retrieval," J. Opt. Soc. Am. B **14,** 944–948 (1997).

[38] M. A. Bolshtyansky, N. V. Tabiryan, and B. Y. Zel'dovich, "BRIEFING: beam reconstruction by iteration of an electromagnetic field with an induced nonlinearity gauge," Opt. Lett. **22,** 22–24 (1997).

[39] T. Feurer, S. Niedermeier, and R. Sauerbrey, "Measuring the temporal intensity of ultrashort laser pulses by triple correlation," Appl. Phys. B **66,** 163–168 (1998).

[40] F. Reynaud, F. Salin, and A. Barthelemy, "Measurement of phase shifts introduced by nonlinear optical phenomena on subpicosecond pulses," Opt. Lett. **14,** 275–277 (1989).

[41] D. Strickland and P. B. Corkum, "Resistance of short pulses to self-focusing," J. Opt. Soc. Am. B **11,** 492–497 (1994).

[42] J. K. Ranka, R. W. Schirmer, and A. L. Gaeta, "Observation of pulse splitting in nonlinear dispersive media," Phys. Rev. Lett. **77,** 3783–3786 (1996).

[43] R. L. Fork, C. V. Shank, C. Hirlimann, R. Yen, and W. J. Tomlinson, "Femtosecond white-light continuum pulses," Opt. Lett. **8,** 1–3 (1983).

[44] M. Sheik-Bahae, A. A. Said, T.-H. Wei, D. J. Hagan, and E. W. Van Stryland, "Sensitive measurement of optical nonlinearities using a single beam," IEEE J. Quantum Electron. **26,** 760–769 (1990).

[45] T. D. Krauss and F. W. Wise, "Femtosecond measurement of nonlinear absorption and refraction in solids," Appl. Phys. Lett. **65,** 1739–1741 (1994).

[46] Newport Catalog (Newport Corp., Irvine, 1994).

[47] V. V. Yakovlev, B. Kohler, and K. R. Wilson, "Broadly tunable 30-fs pulses produced by optical parametric amplification," Opt. Lett. **19,** 2000–2002 (1994).

[48] R. Trebino and D. J. Kane, "Using phase retrieval to measure the intensity and phase of ultrashort pulses: frequency-resolved optical gating," J. Opt. Soc. Am. A **10,** 1101–1111 (1993).

[49] D. J. Kane and R. Trebino, "Single-shot measurement of the intensity and phase of an arbitrary ultrashort pulse by using frequency-resolved optical gating," Opt. Lett. **18,** 823–825 (1993).

[50] K. W. DeLong, C. L. Ladera, R. Trebino, B. Kohler, and K. R. Wilson, "Ultrashort-pulse measurement using noninstantaneous nonlinearities: Raman effects in frequency-resolved optical gating," Opt. Lett. **20,** 486–488 (1995).

[51] J. Paye, M. Ramaswamy, J. G. Fujimoto, and E. P. Ippen, "Measurement of the amplitude and phase of ultrashort light pulses from spectrally resolved autocorrelation," Opt. Lett. **18,** 1946–1948 (1993).

[52] K. W. DeLong, R. Trebino, J. Hunter, and W. E. White, "Frequency-resolved optical gating with the use of second-harmonic generation," J. Opt. Soc. Am. B **11,** 2206–2215 (1994).

[53] T. Tsang, M. A. Krumbügel, K. W. Delong, D. N. Fittinghoff, and R. Trebino, "Frequency-resolved optical-gating measurements of ultrashort pulses using surface third-harmonic generation," Opt. Lett. **21,** 1381–1383 (1996).

[54] J. N. Sweetser, D. N. Fittinghoff, and R. Trebino, "Transient-grating frequency-resolved optical gating," Opt. Lett. **22,** 519–521 (1997).

[55] R. Trebino, K. W. DeLong, D. N. Fittinghoff, J. N. Sweetser, Marco A. Krumbügel, B. A. Richman, and D. J. Kane, "Measuring ultrashort laser pulses in the time-frequency domain using frequency-resolved optical gating," Rev. Sci. Inst. **68,** 3277–3295 (1997).

[56] K. W. DeLong and R. Trebino, "Improved ultrashort pulse-retrieval algorithm for frequency-resolved optical gating," J. Opt. Soc. Am. A **11,** 2429–2437 (1994).

[57] K. W. DeLong, D. N. Fittinghoff, R. Trebino, B. Kohler, and K. Wilson, "Pulse retrieval in frequency-resolved optical gating based on the method of generalized projections," Opt. Lett. **19,** 2152–2154 (1994).

[58] J. W. Nicholson, F. G. Omenetto, D. J. Funk, and A. J. Taylor, "Evolving FROGS: phase retrieval from frequency-resolved optical gating measurements by use of genetic algorithms," Opt. Lett. **24,** 490–492 (1999).

[59] D. N. Fittinghoff, K. W. DeLong, R. Trebino, and C. L. Ladera, "Noise sensitivity in frequency-resolved optical-gating measurements of ultrashort pulses," J. Opt. Soc. Am. B **12,** 1955–1967 (1995).

[60] K. W. DeLong, D. N. Fittinghoff, and R. Trebino, "Practical issues in ultrashort-laser-pulse measurement using frequency-resolved optical gating," IEEE J. Quantum Electron. **32,** 1253–1264 (1996).

[61] K. W. DeLong, R. Trebino, and D. J. Kane, "Comparison of ultrashort-pulse frequency-resolved-optical-gating traces for three common beam geometries," J. Opt. Soc. Am. B **11,** 1595–1608 (1994).

[62] D. J. Kane, A. J. Taylor, R. Trebino, and K. W. DeLong, "Single-shot measurement of the intensity and phase of a femtosecond UV laser pulse with frequency-resolved optical gating," Opt. Lett. **19,** 1061–1063 (1994).

[63] T. S. Clement, A. J. Taylor, and D. J. Kane, "Single-shot measurement of the amplitude and phase of ultrashort laser pulses in the violet," Opt. Lett. **20,** 70–72 (1995).

[64] D. N. Fittinghoff, J. L. Bowie, J. N. Sweetser, R. T. Jennings, M. A. Krumbügel, K. W. DeLong, R. Trebino, and I. A. Walmsley, "Measurement of the intensity and phase of ultraweak, ultrashort laser pulses," Opt. Lett. **21,** 884–886 (1996).

[65] D. J. Kane, "Real-time measurement of ultrashort laser pulses using principal component generalized projections," IEEE J. Select. Topics Quantum Electron. **4,** 278–284 (1998).

[66] D. J. Kane, "Recent progress toward real-time measurement of ultrashort laser pulses," IEEE J. Quantum Electron. **35,** 421–431 (1999).

[67] M. Munroe, D. H. Christensen, and R. Trebino, "Error bars in intensity and phase measurements of ultrashort laser pulses," In Technical Digest. Summary of papers presented at the Conference on Lasers and Electro-Optics, **6,** 462–463 (1998).

[68] K. W. DeLong, R. Trebino, and W. E. White, "Simultaneous recovery of two ultrashort laser pulses from a single spectrogram," J. Opt. Soc. Am. B **12,** 2463–2466 (1995).

[69] D. J. Kane, G. Rodriguez, A. J. Taylor, and T. S. Clement, "Simultaneous measurement of two ultrashort laser pulses from a single spectrogram in a single shot," J. Opt. Soc. Am. B **14,** 935–943 (1997).

[70] C. W. Siders, A. J. Taylor, and M. C. Downer, "Multipulse interferometric frequency-resolved optical gating: real-time phase-sensitive imaging of ultrafast dynamics," Opt. Lett. **22,** 624–626 (1997).

[71] C. W. Siders, J. L. W. Siders, and A. J. Taylor, "Femtosecond coherent spectroscopy at 800 nm: measuring high-field ionization rates in gases with MI FROG," In Technical Digest. Summary of papers presented at the International Quantum Electronics Conference, **7,** 43–44 (1998).

[72] C. W. Siders, J. L. W. Siders, F. G. Omenetto, and A. J. Taylor, "Multiple interferometric frequency-resolved optical gating," IEEE J. Quantum Electron. **35,** 432–440 (1999).

[73] M. D. Thomson, J. M. Dudley, L. P. Barry, and J. D. Harvey, "Waveguide-enhanced frequency-resolved optical gating at $1.5\ \mu\mathrm{m}$ using the Kerr nonlinearity in optical fibre," In ACOFT '98 Proceedings. 23rd Australian Conference on Optical Fibre Technology, pp. 57–60 (1998).

[74] M. D. Thomson, J. M. Dudley, L. P. Barry, and J. D. Harvey, "Complete pulse characterization at $1.5\ \mu\mathrm{m}$ by cross-phase modulation in optical fibers," Opt. Lett. **23,** 1582–1584 (1998).

[75] L. Jusinski, A. Kwok, M. A. Krumbügel, J. N. Sweetser, and R. Trebino, "Frequency-resolved optical gating using cascaded second-order nonlinearities," In Technical Digest. Summary of papers presented at the Conference on Lasers and Electro-Optics, **6,** 464–465 (1998).

[76] A. Kwok, L. Jusinski, M. A. Krunbügel, J. N. Sweetser, D. N. Fittinghoff, and R. Trebino, "Frequency-resolved optical gating using cascaded second-order nonlinearities," IEEE J. Select. Topics Quantum Electron. **4,** 271–277 (1998).

[77] G. Taft, A. Rundquist, M. M. Murnane, H. C. Kapteyn, K. W. DeLong, R. Trebino, and I. P. Christov, "Ultrashort optical waveform measurements using frequency-resolved optical gating," Opt. Lett. **20,** 743–745 (1995).

[78] G. Taft, A. Rundquist, M. M. Murnane, I. P. Christov, H. C. Kapteyn, K. W. DeLong, D. N. Fittinghoff, M. A. Krumbügel, J. N. Sweetser, and R. Trebino, "Measurement of 10-fs laser pulses," IEEE J. Select. Topics Quant. Electron. **2,** 575–584 (1996).

[79] A. Baltuska, M. S. Pshenichnikov, and D. A. Wiersma, "Amplitude and phase characterization of 4.5-fs pulses by frequency-resolved optical gating," Opt. Lett. **23,** 1474–1476 (1998).

[80] A. Baltuska, M. S. Pshenichnikov, and D. A. Wiersma, "SHG FROG characterization of < 5-fs pulses," In Technical Digest. Summary of papers presented at the Conference on Lasers and Electro-Optics, **6,** 461–462 (1998).

[81] J. M. Dudley, L. P. Barry, J. D. Harvey, M. D. Thomson, B. C. Thomsen, P. G. Bollond, and R. Leonhardt, "Complete characterization of ultrashort pulse sources at 1550 nm," IEEE J. Quantum Electron. **35,** 441–450 (1999).

[82] A. J. Taylor, G. Rodriguez, and T. S. Clement, "Determination of n_2 by direct measurement of the optical phase," Opt. Lett. **21,** 1812–1814 (1996).

[83] P. J. Delfyett, S. Hong, S. Gee, I. Nitta, J. C. Connolly, and G. A. Alphonse, "Joint time-frequency measurements of modelocked semiconductor diode lasers and dynamics using frequency-resolved optical gating," IEEE J. Quantum Electron. **35,** 487–500 (1999).

[84] W. Theobald, R. Hassner, S. Niedermeier, K. Michelmann, T. Feurer, H. Schillinger, R. Sauerbrey, and G. Schafer, "Relativistic accelerations in femtosecond laser produced plasmas," In Technical Digest. Summary of papers presented at the International Quantum Electronics Conference, **7,** 75 (1998).

[85] S. P. Nikitin, Y. Li, T. M. Antonsen, and H. M. Milchberg, "Ionization-induced pulse shortening and retardation of high intensity femtosecond laser pulses," Optics Commun. **157,** 139–144 (1998).

[86] K. Furusawa, H. Yabe, and M. Obara, "Automatic ultrafast pulse compresor in chirped pulse amplification by FROG using fuzzy control technique," In Conference Proceedings. LEOS '98, **1,** 138–139 (1998).

[87] T. Brixner, M. Strehle, and G. Gerber, "Feedback-controlled optimization of amplified femtosecond laser pulses," Appl. Phys. B. **B68,** 281–284 (1999).

[88] V. D. Kleiman, S. M. Arrivo, J. S. Melinger, and E. J. Heilweil, "Controlling condensed-phase vibrational excitation with tailored infrared pulses," Chem. Phys. **233,** 207–216 (1998).

[89] H. K. Eaton, T. S. Clement, A. A. Zozulya, and S. A. Diddams, "Investigating nonlinear femtosecond pulse propagation with frequency-resolved optical gating," IEEE J. Quantum Electron. **35,** 451–457 (1999).

[90] A. A. Zozulya, S. A. Diddams, and T. S. Clement, "Investigations of nonlinear femtosecond pulse propagation with the inclusion of Raman, shock, and third-order phase effects," Phys. Rev. A **58,** 3303–3310 (1998).

[91] S. A. Diddams, H. K. Eaton, A. A. Zozulya, and T. S. Clement, "Amplitude and phase measurements of femtosecond pulse splitting in nonlinear dispersive media," Opt. Lett. **23,** 379–381 (1998).

[92] A. M. Weiner, "Effect of group velocity mismatch on the measurement of ultrashort optical pulses via second harmonic generation," IEEE J. Quantum Electron. **QE-19,** 1276–1283 (1983).

[93] Y. Ishida, K. Naganuma, and T. Yajima, "Self-phase modulation in hybridly mode-locked cw dye lasers," IEEE J. Quantum Electron. **QE-21,** 69–77 (1985).

[94] E. T. J. Nibbering, M. A. Franco, B. S. Prade, G. Grillon, C. L. Blanc, and A. Mysyrowicz, "Measurement of the nonlinear refractive index of transparent materials by spectral analysis after nonlinear propagation," Optics Commun. **119,** 479–484 (1995).

[95] E. T. J. Nibbering, G. Grillon, M. A. Franco, B. S. Prade, and A. Mysyrowicz, "Determination of the inertial contribution to the nonlinear refractive index of air, N_2, and O_2 by use of unfocused high-intensity femtosecond laser pulses," J. Opt. Soc. Am. B **14,** 650–660 (1997).

[96] J. M. Dudley, L. P. Barry, P. G. Bollond, J. D. Harvey, R. Leonhardt, and P. D. Drummond, "Direct measurement of pulse distortion near the zero-dispersion wavelength in an optical fiber by frequency-resolved optical gating," Opt. Lett. **22,** 457–459 (1997).

[97] A. Siegman, Lasers (University Science Books, Mill Valley, CA, 1986).

[98] S. A. Diddams, H. K. Eaton, A. A. Zozulya, and T. S. Clement, "Characterizing the nonlinear propagation of femtosecond pulses in bulk media," IEEE J. Select. Topics Quant. Electr. **4,** 306–316 (1998).

[99] R. Hellwarth, J. Cherlow, and T.-T. Yang, "Origin and frequency dependence of nonlinear optical susceptiblities in glass," Phys. Rev. B **11,** 964–967 (1975).

[100] R. H. Stolen, J. P. Gordon, W. J. Tomlinson, and H. A. Haus, "Raman response function of silica core fibers," J. Opt. Soc. Am. B **6,** 1159–1166 (1989).

[101] R. H. Stolen and W. J. Tomlinson, "Effect of the Raman part of the nonlinear refractive index on propagation of ultrashort optical pulses in fibers," J. Opt. Soc. Am. B **9,** 565–573 (1992).

[102] C. Radzewicz, J. S. Krasinski, Y. B. Band, and M. Trippenbach, "Femtosecond light wavepackets,", Presented at LASE '99, Photonics West, San José, CA, 1999.

[103] N. A. Zharova, A. G. Litvak, T. A. Petrova, A. M. Sergeev, and A. D. Yunakoviskii, "Multiple fractionation of wave structures in a nonlinear medium," JETP Lett. **44,** 13–17 (1986).

[104] P. Chernev and V. Petrov, "Self-focusing of light pulses in the presence of normal group-velocity dispersion," Opt. Lett. **17,** 172–174 (1992).

[105] J. E. Rothenberg, "Pulse splitting during self-focusing in normally dispersive media," Opt. Lett. **17,** 583–585 (1992).

[106] J. T. Manassah and B. Gross, "Self-focusing of (3+1)-D femtosecond pulses in nonlinear Kerr media," Laser Physics **6,** 563–578 (1996).

[107] G. P. Agrawal, Nonlinear Fiber Optics (Academic Press, San Diego, 1995).

[108] D. Strickland and P. B. Corkum, "Short pulse self-focusing," In Short-Pulse High-Intensity Lasers and Applications, H. A. Baldis, ed.,**1413,** 54–58 (1991).

[109] J. K. Ranka and A. L. Gaeta, "Breakdown of the slowly-varying envelope approximation in the self-focusing of ultrashort pulses," Opt. Lett. **23,** 534–536 (1998).

[110] J. H. Marburger, "Self-focusing as a pulse sharpening mechanism," IEEE J. Quantum Electron. **QE-3,** 415 (1967).

[111] Y. Silberberg, "Collapse of optical pulses," Opt. Lett. **15,** 1282–1284 (1990).

[112] R. McLeod, K. Wagner, and S. Blair, "(3+1)-dimensional optical soliton dragging logic," Phys. Rev. A **52,** 3254–3278 (1995).

[113] D. E. Edmundson and R. H. Enns, "Robust bistable light bullets," Opt. Lett. **17,** 586–588 (1992).

[114] J. H. Marburger, "Self-Focusing: Theory," Prog. Quant. Electr. **4,** 35–110 (1975).

[115] G. G. Luther, J. V. Moloney, A. C. Newell, and E. M. Wright, "Self-focusing threshold in normally dispersive media," Opt. Lett.. **19,** 862–864 (1994).

[116] G. L. McAllister, J. H. Marburger, and L. G. DeShazer, "Observation of optical pulse shaping by the self-focusing effects," Phys. Rev. Lett. **21,** 1648–1649 (1968).

[117] J. K. Ranka and A. L. Gaeta, "Nonlinear dynamics of the self-focusing of ultrashort pulses,", presented at Ultrafast Optics 1997, Monterrey, CA, paper MB-3.

[118] M. Trippenbach and Y. B. Band, "Dynamics of short-pulse splitting in dispersive nolinear media," Phys. Rev. A **56,** 4242–4253 (1997).

[119] A. A. Zozulya, S. A. Diddams, A. G. Van Engen, and T. S. Clement, "Propagation dynamics of intense femtosecond pulses: Multiple splittings, coalescence, and continuum generation," Phys. Rev. Lett. **82,** 1430–1433 (1999).

[120] I. Ledoux, J. Zyss, A. Migus, J. Etchepare, G. Grillon, and A. Antonelli, "Generation of high peak power subpicosecond pulses in the 1.0-1.6 μm range by parametric amplification in an organic crystal," Appl. Phys. Lett. **48,** 1564–1566 (1986).

[121] S. R. Greenfield and M. R. Wasielewski, "Optical parametric amplification of femtosecond pulses tunable from the blue to the infrared with microjoule energies," Appl. Opt. **34,** 2688–2691 (1995).

[122] T. S. Sosnowski, P. B. Stephens, and T. B. Norris, "Production of 30-fs pulses tunable throughout the visible spectral region by a new technique in optical parametric amplification," Opt. Lett. **21,** 140–142 (1996).

[123] T. M. Jedju and L. Rothberg, "Tunable femtosecond radiation in the mid-infrared for time-resolved absorption in semiconductors," Appl. Opt. **27,** 615–618 (1988).

[124] The Supercontinuum Laser Source, R. R. Alfano, ed., (Springer-Verlag, New York, 1989).

[125] M. Nisoli, S. De Silvestri, and O. Svelto, "Generation of high energy 10 fs pulses by a new pulse compression technique," Appl. Phys. Lett. **68,** 2793–2795 (1996).

[126] R. R. Alfano and S. L. Shapiro, "Emission in the region 4000 to 7000 Åvia four-photon coupling in glass," Phys. Rev. Lett. **24,** 584–587 (1970).

[127] M. Hercher, "Laser-induced damage in transparent media," J. Opt. Soc. Am. **54,** 563 (1964).

[128] R. Y. Chiao, E. Garmire, and C. H. Townes, "Self-trapping of optical beams," Phys. Rev. Lett. **13,** 479–482 (1964).

[129] E. T. J. Nibbering, P. F. Curley, G. Grillon, B. S. Prade, M. A. Franco, F. Salin, and A. Mysyrowicz, "Conical emission from self-guided femtosecond pulses in air," Opt. Lett. **21,** 62–64 (1996).

[130] M. M. Loy and Y. R. Shen, "Study of self-focusing and small-scale filaments of light in nonlinear media," IEEE J. Quantum Electron. **QE-9,** 409–422 (1973).

[131] W. L. Smith, P. Liu, and N. Bloembergen, "Superbroadening in H_2O and D_2O by self-focused picosecond pulses from a YAlG:Nd laser," Phys. Rev. A **15,** 2396–2403 (1977).

[132] P. B. Corkum and C. Rolland, "Femtosecond continua produced in gases," IEEE J. Quantum Electron. **25,** 2634–2639 (1989).

[133] R. R. Alfano and S. L. Shapiro, "Observation of self-phase modulation and small-scale filaments in crystals and glasses," Phys. Rev. Lett. **24,** 592–594 (1970).

[134] T. R. Gosnell, A. J. Taylor, and D. P. Greene, "Supercontinuum generation at 248 nm using high-pressure gases," Opt. Lett. **15,** 591–593 (1990).

[135] A. Brodeur and S. L. Chin, "Band-gap dependence of the ultrafast white-light continuum," Phys. Rev. Lett. **80,** 4406–4409 (1998).

[136] P. B. Corkum, P. P. Ho, R. R. Alfano, and J. T. Manassah, "Generation of infrared supercontinuum covering 3-14 μm in dielectrics and semiconductors," Opt. Lett. **10,** 584–586 (1985).

[137] P. B. Corkum, C. Rolland, and T. Srinivasan-Rao, "Supercontinuum generation in gases," Phys. Rev. Lett. **57,** 2268–2271 (1986).

[138] H. Nishioka, W. Odajima, K.-I. Ueda, and H. Takuma, "Ultrabroadband flat continuum generation in multichannel propagation of terrawatt Ti:sapphire laser pulses," Opt. Lett. **20,** 2505–2507 (1995).

[139] A. Penzkofer, A. Laubereau, and W. Kaiser, "Stimulated short-wave radiation due to single-frequency resonances of $\chi^{(3)}$," Phys. Rev. Lett. **31,** 863–866 (1973).

[140] A. Penzkofer, "Parametrically generated spectra and optical breakdown in H_2O and NaCl," Optics Commun. **11,** 265–269 (1974).

[141] A. Penzkofer, A. Seilmeier, and W. Kaiser, "Parametric four-photon generation of picosecond light at high conversion efficiency," Optics Commun. **14,** 363–367 (1975).

[142] M. Wittmann and A. Penzkofer, "Spectral superbroadening of femtosecond laser pulses," Optics Commun. **126,** 308–317 (1996).

[143] G. Yang and Y. R. Shen, "Spectral broadening of ultrashort pulses in a nonlinear medium," Opt. Lett. **9,** 510–512 (1984).

[144] J. T. Manassah, M. A. Mustafa, R. R. Alfano, and P. P. Ho, "Spectral extent and pulse shape of the supercontinuum for ultrashort laser pulse," IEEE J. Quantum Electron. **QE-22,** 197–204 (1970).

[145] N. Bloembergen, "The influence of electron plasma formation on superbroadening in light filaments," Optics Commun. **8,** 285–288 (1973).

[146] A. Brodeur and S. L. Chin, "Ultrafast white-light continuum generation and self-focusing in transparant condensed media," J. Opt. Soc. Am. B **16,** 637–650 (1999).

[147] Y. R. Shen, "Self-focusing: Experimental," Prog. Quant. Electr. **4,** 1–34 (1975).

[148] A. A. Zozulya, 1999, department of Physics, Worcester Polytechnic Institute, private communication.

[149] A.-C. Tien, S. Backus, H. Kapteyn, M. Murnane, and G. Mourou, "Short-pulse laser damage in transparant materials as a function of pulse duration," Phys. Rev. Lett. **82,** 3883–3886 (1999).

[150] O. M. Efimov, K. Gabel, S. V. Garnov, L. B. Glebov, S. Grantham, M. Richardson, and M. J. Soileau, "Color-center generation in silicate glasses exposed to infrared femtosecond pulses," J. Opt. Soc. Am. B **15,** 193–199 (1998).

[151] M. M. Denariez-Roberge and J.-P. E. Taran, "Experimental confirmation of self-trapping from the dependence of self-modulation on propagation distance," Appl. Phys. Lett. **14,** 205–207 (1969).

[152] I. L. Fabellinski, in Molecular Scattering of Light (Plenum, New York, 1967), Chap. VIII.

[153] R. F. Bonner, "Laser capture microdissection (LCM) and the future of molecular pathology," In Conference Proceedings. LEOS 98, **2,** 226–228 (1998).

[154] J. S. Nelson, "Recent advances in laser treatment of human skin," In Conference Proceedings. LEOS 98, **2,** 335–336 (1998).

[155] L. B. Da Silva, B.-M. Kim, M. D. Feit, and A. M. Rubenchik, "Use of ultrashort pulse lasers in medicine," In Conference Proceedings. LEOS 98, **2,** 443–444 (1998).

[156] A. G. Van Engen, JILA, University of Colorado, private communication, 1998.

[157] P. P. Ho and R. R. Alfano, "Optical Kerr effect in liquids," Phys. Rev. A **20,** 2170–2187 (1979).

[158] P. T. Guerreiro, S. G. Lee, A. S. Rodrigues, Y. Z. Hu, E. M. Wright, S. I. Najafi, J. Mackenzie, and N. Peyghambarian, "Femtosecond pulse propagation near a two-photon transistion in a semiconductor quantum-dot waveguide," Opt. Lett. **21,** 659–661 (1996).

[159] in CRC Handbook of Laser Science and Technology, M. J. Webster, ed., (CRC Press, Boca Raton, FL, 1986), Vol. III, p. 270.

[160] B. A. Rockwell, W. P. Roach, M. E. Rogers, W. M. Mayo, C. A. Toth, C. P. Cain, and G. D. Noojin, "Nonlinear refraction in vitreous humor," Opt. Lett. **18,** 1792–1794 (1993).

[161] J. Piasecki, B. Colombeau, M. Vampouille, C. Froehly, and J. A. Arnaud, "Nouvelle méthode de mesure de la réponse impulsionnelle des fibres optiques," Appl. Opt. **19,** 3749–3755 (1980).

[162] L. Lepetit, G. Chériaux, and M. Joffre, "Linear techniques of phase measurement by femtosecond spectral interferometry for applications in spectroscopy," J. Opt. Soc. Am. B **12,** 2467–2474 (1995).